FUNDAMENTAL STUDY OF THE MECHANICAL FAILURE OF SILICON BASED ELECTRODES FOR LI-ION BATTERIES USING A NOVEL MULTI-PHYSICS COMPUTATIONAL MODELING FRAMEWORK

by

Sameer Satish Damle

B.S. in Chemical Engineering, Institute of Chemical Technology, Mumbai, 2010

Submitted to the Graduate Faculty of

Swanson School of Engineering in partial fulfillment

of the requirements for the degree of

Doctor of Philosophy

University of Pittsburgh

2016

UNIVERSITY OF PITTSBURGH

SWANSON SCHOOL OF ENGINEERING

This dissertation was presented

by

Sameer Satish Damle

It was defended on

March 1, 2016

and approved by

Sachin Velankar, Ph.D., Associate Professor

Departmental of Chemical Engineering, University of Pittsburgh

Amit Acharya, Ph.D., Professor

Civil and Environmental Engineering, Carnegie Mellon University

Dissertation Director: Spandan Maiti, Ph.D., Assistant Professor

Departmental of Bioengineering, University of Pittsburgh

Dissertation Co-director: Prashant N Kumta, Ph.D., Edward R. Weidllein Chair Professor

Departmental of Bioengineering, University of Pittsburgh

FUNDAMENTAL STUDY OF THE MECHANICAL FAILURE OF SILICON BASED ELECTRODES FOR LI-ION BATTERIES USING A NOVEL MULTI-PHYSICS COMPUTATIONAL MODELING FRAMEWORK

Sameer Satish Damle, PhD

University of Pittsburgh, 2016

Li-ion batteries are the currently accepted flagship energy storage system with several cathode systems identified over the years. However, graphite has always remained the commercial anode material of choice. Silicon has been identified as the next-generation anode for Li-ion systems with a high theoretical capacity (4200 $mAhg^{-1}$) compared to graphite (372 $mAhg^{-1}$) and has been the focus of much research over the past decade. Silicon unfortunately, undergoes large volumetric expansion (312%) upon Li diffusion generating considerable diffusion-induced stresses. Presence of high stress leads to mechanical failure of Si resulting in capacity fade due to loss of electrical contact with the current collector impeding commercialization. The mechanical response of the electrode depends on the electrode properties comprising the active (Si) and passive components (current collector, mechanical supports). The objective of this thesis is to gain a mechanistic understanding of the interactions between the electrode components and their effect on the overall mechanical integrity of the Si based anode assembly, which can aid in the design of failure resistant, next-generation, high capacity anodes.

To achieve this objective, a custom nonlinear finite element modeling software that can model coupled diffusion induced large elasto-plastic deformation of Si, surface electrochemical reaction kinetics and eventual mechanical failure response of the electrode system was utilized. This modeling framework is first used to understand the effect of passive components (current

collector and Si-Cu interface properties) on the mechanical stability of an *a*-Si thin film anode system. To unlock the mechanisms behind the gradual interfacial delamination of the Si film from the underlying Cu current collector in an *a*-Si thin film anode system, a detailed parametric study is performed to analyze effect of the mechanical properties of the current collector and the Si-Cu interface on the delamination at Si-Cu interface. The knowledge gained from these studies is further bolstered by examining the mechanical stability of *a*-Si patterned thin film anodes upon insertion of a thin elastic buffer layer between a square Si thin film pattern and the current collector. Finally, the modeling framework is utilized to understand the effect of active material geometry in Si-carbon nanotube (CNT) heterostructured anodes.

TABLE OF CONTENTS

LIST OF TABLES

LIST OF FIGURES

NOMENCLATURE

A	Surface area of Si in contact with electrolyte (m^2)
c	Concentration of Li in the reference configuration ($mol\,m^{-3}$)
c_{max}	Maximum Li intercalation concentration in anode material ($mol\,m^{-3}$)
c_e	Concentration of electrolyte ($mol\,m^{-3}$)
c_s	Concentration of Li ions on the surface of the active material ($mol\,m^{-3}$)
C	Capacity of the electrode material ($mAh\,g^{-1}$)
$C\text{-}rate$	Charge rate
$\mathbf{C}$	Right Cauchy Green tensor
D	Diffusivity of Li atom in the anode material ($m^2\,s^{-1}$)
DI	Delamination index
E	Young's modulus (Pa)
f	Yield function
F	Faraday's constant ($Ahmol^{-1}$)
$\mathbf{F}$	Deformation gradient
$\mathbf{F}_e$	Elastic component of the deformation gradient
$\mathbf{F}_p$	Plastic component of the deformation gradient
$\mathbf{F}_\theta$	Expansion component of the deformation gradient
H	Hardening Modulus (Pa)
i	Current (A)
i_0	Exchange current density (Am^{-2})
$\mathbf{I}$	Identity tensor
G_c	Fracture toughness of the material/interface (Jm^{-2})
J_{Li}	Li atom flux ($mol\ m^{-2}\,s^{-1}$)

J_θ	Jacobian associated with expansion component of the deformation gradient
k	Kinetic rate constant $(\text{m s}^{-1})(\text{mol m}^{3})^{-0.5}$
$\boldsymbol{l}$	Spatial velocity gradient
$\mathbf{L}$	Spatial velocity gradient pulled back to intermediate configuration
$\mathbf{L}_p$	Plastic deformation gradient
$Li_{fraction}$	Fraction of lithium concentration in Li_xSi alloy
m	Mass of the active material (Si) in the electrode configuration (g)
M	Mobility of solvent
$\mathbf{M}_e$	Mandel stress tensor
n	Duration of the lithium alloying/de-alloying half cycle (sec)
p	Hydrostatic pressure (Pa)
$\mathbf{P}$	First Piola-Kirchhoff stress tensor
R	Universal gas constant ($\text{J mol}^{-1}\text{ K}^{-1}$)
R_c	Contact resistance (Ohms)
s	Entropy density
$\mathbf{S}$	Second Piola-Kirchhoff stress tensor
T	Temperature
t	Time (sec)
t_e	Effective traction
$\boldsymbol{t}_c$	Traction at the cohesive surface
$\boldsymbol{u}$	Displacement field
U_{OCP}	Open circuit potential (Volts)
$\boldsymbol{x}$	Position vector of material point in current configuration
$\mathbf{X}$	Position vector of material point in reference configuration
α_a, α_c	Anodic and cathodic transfer coefficient
$\boldsymbol{\delta}$	Displacement jump vector
δ_e, δ_c	Effective and characteristic opening displacement jump

ν	Poisson's ratio
$\dot{\lambda}$	Plastic rate parameter
ε_p	Plastic strain
μ	Chemical potential
η	Partial volume of Li in Si ($m^3 mol^{-1}$)
η_s	Overpotential (Volts)
ω	Rate of change of elastic modulus of *a*-Si with Li fraction in the Li_xSi alloy (Pa $Li_{fraction}^{-1}$)
σ_y	Yield strength of the material
σ_c	Maximum cohesive normal traction
Ψ	Free energy functional

1.0 INTRODUCTION

In the past four decades, there has been a threefold increase in the world's energy demand[1]. To reduce the U.S. dependence on fossil fuels as a source of energy, continuous efforts are being made to harvest energy from renewable sources. However, for a continuous and uninterrupted supply of energy from renewable sources, there is a critical need for strategies and technologies to effectively store the generated energy. Since the commercialization of the first commercial Li-ion battery by Sony in 1991, Li-ion batteries (LIBs) have emerged as the flagship energy storage system[2]. The current Li-ion batteries boast a higher volumetric and gravimetric energy density than other battery technologies such as Pb-acid, Ni-MH, Ni-Cd, etc[3]. The currently developed LIBs is ubiquitously used in personal devices ranging from laptops and camcorders to smartphones. However, deployment of LIBs in advanced platform technologies such as hybrid and plug-in hybrid vehicles (PHEVs), all electric vehicles (EVs), and aerospace applications will require still higher energy densities than what is currently achievable. Thus, there is continued research on-going to further improve the LIB technology to increase its already prevalent wide scale deployment in these advanced areas[4].

Schematics of a typical LIB are shown in Figure 1 **(a).** The standard LIB cell consists of two electrodes separated by an electrolyte and a separator. Each electrode assembly includes multiple components, which can be classified into active and passive components. The active material participates in the electrochemical reaction while the passive components (such as current collector, conductive additive, binder, mechanical support, separator, etc.) help in the electron transfer and maintenance of the mechanical integrity of the entire assembly. The

operation of LIBs can be described as 'rocking chair' or 'shuttle-cock' mechanism[3] where the Li ions travel back and forth between the anode and cathode compartments through the electrolyte as the battery is charged and discharged (Figure 1 **(a)**). The basic chemical reactions occurring at the electrodes are summarized below,

$$xLi^+ + xe^- \underset{\text{discharge}}{\overset{\text{charge}}{\rightleftharpoons}} Li_xY \quad (\text{anode}) \tag{1.1}$$

$$Li_xMO_2 \underset{\text{discharge}}{\overset{\text{charge}}{\rightleftharpoons}} Li^+ + xe^- \quad (\text{cathode}) \tag{1.2}$$

Equation (1.1) indicates that the specific capacity of the anode is determined by the stoichiometric ratio of Li reacting with the anode material Y to give Li_XY. Currently used commercial Li ion batteries are comprised of graphite as anode material. Li intercalation in graphite results in LiC_6 giving a capacity of 372 mAh g^{-1}[5]. This Li intercalation process is accompanied by a 12% volume expansion of the graphite. To further improve the specific capacity, different materials have been investigated to replace the traditional graphite anode (Figure 1 **(b)**). Among the different materials available, silicon has gathered the most attention due to its high theoretical specific capacity. Contrary to graphite, wherein intercalation is the preferred mode of insertion and de-insertion of the migrating Li-ions, in silicon, the primary mode is alloying and formation of intermetallic or so-called zintl phases. Li alloying of Si results in the formation of $Li_{22}Si_5$ (or $Li_{4.4}Si$) giving a high theoretical capacity of ~4200 mAh g^{-1} [6]. In addition to its higher capacity, Si is also the second most abundant element on earth[7]. Thus, utilization of Si based anodes holds consdierable promise for producing the cost effective next-generation rechargeable batteries.

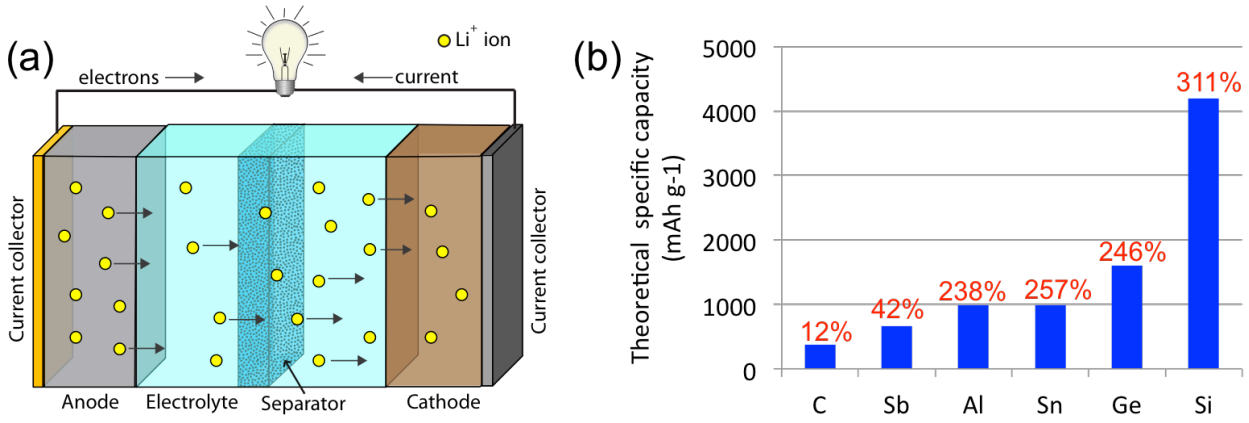

Figure 1. (a) Schematics of a Li-ion battery. (b) Theoretical specific capacity of different anode materials for Li-ion battery. The percentage volumetric expansion occurred on complete lithiation is also indicated.

However, Si undergoes colossal Li alloying induced volumetric expansion (311%) that can generate significant mechanical stresses within the anode assembly. These stresses are often large enough to cause mechanical failure of the anode assembly. Some typical failure scenarios reported in the literature are mechanical degradation of Si due to initiation of cracks leading to eventual fracture[8, 9] (Figure 2 **(a-c)**), void formation[10], surface roughening[11] and delamination[12] (Figure 2 **(d)**) from the current collector causing loss of electronic contact of the active material. Thus, mechanical degradation in Si based electrodes has proven to be a major obstacle in commercialization of the Si based anodes. Understanding the mechanisms responsible for mechanical degradation of the anode assembly is thus of paramount importance to develop Si based next-generation high performance LIB anodes. The focus of the current research work is to understand the failure mechanisms in Si-based anodes through an experimentally validated computational approach.

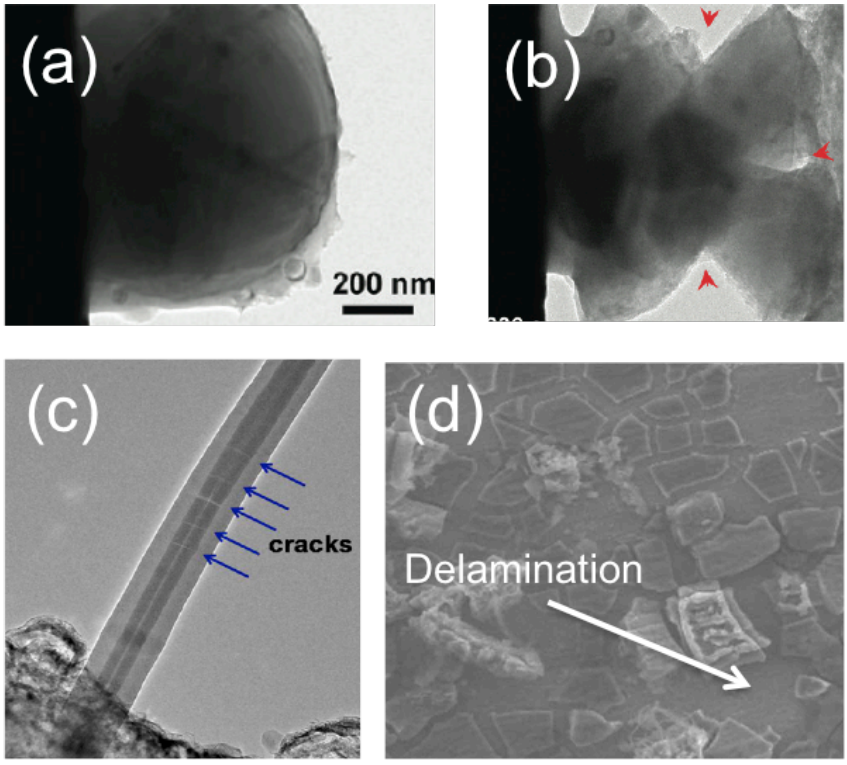

Figure 2. (a-b) A 940 nm diameter Si particle pre and post Li insertion[13]. (c) Radial cracks in a Si-CNT heterostructure anode[9]. (d) Vertical cracks and film delamination in a 250 nm thick Si thin film electrode[14].

2.0 BACKGROUND AND MOTIVATION

In silicon-based nanostructured anodes, the active material, Si can exist in different configurations such as nano-particle[15], nanotube[16], nanowire[17], thin film[18-20], etc. It is accompanied by other passive electrode components such as a metal current collector, separator, mechanical support with high electronic conductivity, binders, conductive additives, etc. Experimental studies have shown that the mechanical response of the anode depends on: (a) the mechanical properties of the passive component and its adhesion to the active component and (b) the dimensions and geometry of the active components. In the following sections, the current knowledge of the effect of passive and active components on the mechanical stability of the anode assembly is detailed with the primary focus on two anode systems; amorphous silicon (a-Si) thin film anode and silicon – carbon nanotube (Si-CNT) heterostructured anode.

2.1 AMORPHOUS SILICON *(A-SI)* THIN FILM ANODE

a-Si thin film electrodes have been extensively researched due to their ease of fabrication and near theoretical performance (~3600 $mAhg^{-1}$)[19, 20]. Experiments show that after the first electrochemical cycle, *a*-Si film exhibits through-thickness cracks resulting in separate islands attached to the current collector[12]. For proper functioning of the anode, transfer of electrons from the Cu current collector and the Si film is necessary. As the Si islands are still in contact with the

underlying current collector, the electrochemical capacity of the anode is still retained. However, after a few cycles, the capacity drops precipitously as the islands delaminate entirely from the metal current collector akin to a deck of cards resulting in complete loss of performance. Hence, the Si-Cu interface stability is a direct criterion to retain the anode capacity.

Modification of the passive component properties on the a-Si thin film anode capacity retention has been explored by experimentalists. Recent work by Datta et al.[21] have shown that the presence of an interfacial layer of amorphous carbon between the *a*-Si thin film and the substrate results in excellent capacity retention of the thin film anode. Similarly, Yu et al.[22] have demonstrated excellent capacity retention of 84.6% after 500 cycles using micro-fabricated ribbons of Si thin film ($100-400\,nm$ and $70-200\,\mu m$ wide) on poly(dimethylsiloxane) (PDMS) substrate. Furthermore, improving the adhesion of the film to the current collector[23] [24] has shown to delay the capacity fade. These observations indicate that the choice of substrate and engineering of the Si-Cu interface can have a direct impact on the Si-Cu interface stability.

2.2 SI-CNT HETEROSTRUCTURED ANODE

Although Si is characterized by a high theoretical capacity, it suffers from poor electronic conductivity and mechanical strength. To circumvent this problem, researchers have explored core-shell heterostructured anode configurations consisting of carbon nanotube (CNT) core and nanostructured Si shell exploiting the superior electronic conductivity and mechanical strength[25-27] of the CNTs. Many researchers have also recently reported synthesis of a Si-CNT core-shell heterostructure consisting of a thin continuous Si coating on the CNT. Even though the results show excellent first cycle capacity, mechanical degradation of the Si due to formation of

nanpores[10], axial cracks[8 11 9] has been observed after prolonged cycling leading to capacity fade. To reduce the mechanical degradation of the continuous coating of Si on CNTs and to prolong the capacity retention of Si-CNT heterostructures, Gohier et al. [28] decorated vertically aligned thin CNTs of 5 nm diameter with 10 nm sized Si droplets. Providing sufficient free space for the expansion of Si droplets resulted in a high reversible capacity of 3000 $mAhg^{-1}$at 1.3 C *C-rate* with 90% capacity retention after 37 cycles. Epur et al.[29] have also shown that having Si droplets geometry deposited on the CNTs gives a better capacity retention compared to continuous films of Si deposited on CNTs. Thus these results indicate that the geometrical features of the active material can alter the cycling performance of the anode significantly, and thus can be a promising route to design high efficiency anode configurations that lead to improved cycling performance.

2.3 COMPUTATIONAL MODELING OF ELECTRODES

Along with the above-mentioned experimental works, significant amount of research has been directed towards mathematical modeling of the Li-ion batteries to understand and predict their performance. Computational simulations allow for faster testing of the battery component design and revision at significantly low cost than physical experimentation. In 1993, Doyle et al. presented an electrochemical *Pseudo2D* model containing differential equation in a lithium battery, which are solved using volume-averaged methods to predict the cell voltage and current as functions of time. Many other similar models predicting the cycle life performance are based on this framework[30-39]. As mechanical degradation is known to be an important factor responsible for capacity fade in electrodes[40], attempts have been made to quantify the stresses

generated in the electrode during electrochemical cycling. Using the analogy between thermal diffusion induced stresses[41, 42] and the Li diffusion induced stresses (DIS), researchers have modeled the stresses evolved during galvanostatic and potentiostatic electrochemical cycling of different electrode geometries. These models reveal important information such as effect of charge rate, elastic softening of the material, surface energy, phase transformations, size of the active material, diffusivity, etc. on the DIS and have commented on the probability of failure of the electrode particle with a simple geometry such as spherical or ellipsoidal particles[43-50], nanowires[51-53], nanotubes[54], etc.

Even though the above-mentioned models provide important insight into the electro-chemo-mechanical behavior of anodes, they are limited to the simulation of simple anode geometries. Moreover, they lack the capability to predict failure of the complex anode assembly. The process of capacity fade in electrodes is gradual and occurs over multiple electrochemical cycles[4]. Diverse electro-chemo-mechanical changes occur in the electrode material such as elasto-plastic deformation[55, 56], evolution of cracks[11, 18], delamination from current collector[12] and elastic softening[57] as described in **Section 2.1** and **2.2**. Moreover, the electrode geometries are complex and often include interaction of the active material with the inactive material.

In recent years, significant progress has been made to improve the state of the art of electrode modeling. Researchers have attempted to simulate and predict crack propagation and mechanical damage in silicon nanowires[13, 58, 59], particles[60] and cylindrical graphitic particles[61], hollow core-shell nanostructures[62]. Shenoy et al.[57] have used first principles studies and attempted to understand the Li alloying induced elastic softening of silicon. In a series of work, Suo's group has also modeled the plastic deformation of silicon during electrochemical cycling[63-67]. However, despite this progress, there still does not exist an experimentally verified modeling

framework capable of simulating the complex anode structures for multiple electrochemical cycles and predict the mechanical degradation leading to capacity fade of the electrode.

2.4 MOTIVATION FOR THE CURRENT WORK

Despite the current knowledge of effect of active and passive components of the silicon anode on its mechanical stability, a mechanistic understanding of the failure of the anode assembly is currently lacking. Failure of anode assembly results from a complex mechanical interaction of the active and passive components during electrochemical cycling, which is still not properly understood as yet. This gap in knowledge prevents the generation of a strategy for fabrication of high capacity, stable, silicon based anodes. Thus there is a need for the development of advanced computational strategies comprising an experimentally guided multi-physics simulation platform that has the following attributes of: (i) Capable of simulating complex anode geometries and its resulting mechanical failure over multiple electrochemical cycles. (ii) Requirement to closely mimic the experimental conditions to understand the mechanical response of such complex electrode systems during electrochemical cycling. Development of such in silico experimental bench can be expected to cut down the development time of next-generation electrodes. The details of the goals and objectives for this dissertation thesis are detailed in next chapter.

3.0 RESEARCH GOALS, OBJECTIVES AND CONTRIBUTIONS

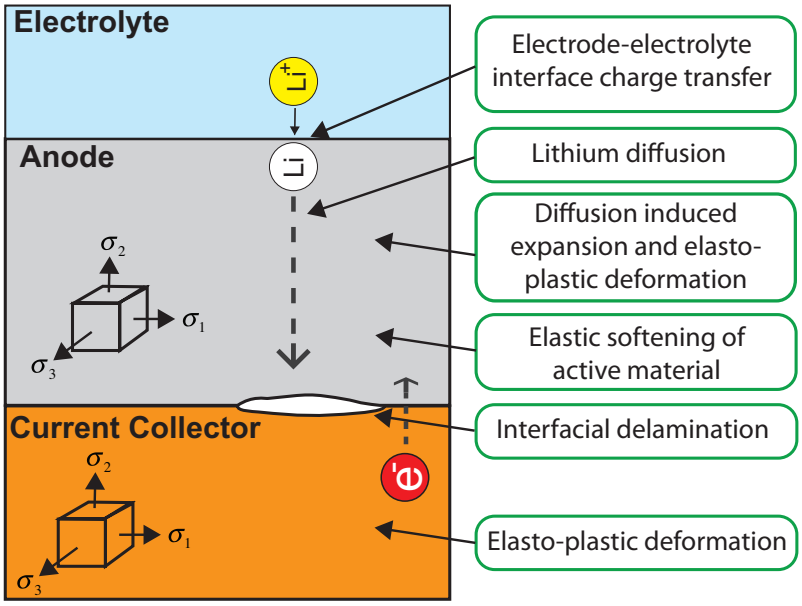

Figure 3. Schematics of mechanisms operative during electrode electrochemical cycling.

The objective of this dissertation thesis is to utilize a thermodynamically consistent theoretical framework that considers the coupled diffusion induced large deformation as well as failure response of the electrode materials system. The modeling framework is capable of simulating elastic and elasto-plastic behavior of the electrode components, as well as predicting its voltage-capacity response. A cohesive zone technique[68-70] has been utilized to simulate the fracture in the bulk of the active material as well as its delamination from the inactive component in the electrode (current collector, mechanical support, etc.). A schematic detailing the mechanisms considered in the modeling framework operative during electrode electrochemical cycling is

shown in Figure 3. The modeling framework is utilized to gain mechanistic understanding of the effect of active and passive components on the mechanical stability of the Si based anode structures.

The major goals of this dissertation are divided into three main categories

- **To verify and validate a thermodynamically consistent framework to model the electro-chemo-mechanical response electrode structure during electrochemical cycling.** The model should be capable of simulating the Li diffusion induced stresses and the coupled Li transport inside the active material, elastic as well as elasto-plastic deformation of the electrode components and the ensuing fracture/delamination of the electrode components.
- **To examine the effect of electrode passive components on the mechanical integrity of *a*-Si thin film anode systems using the modeling framework.**
  - Effect of current collector properties (elastic modulus and yield strength) on stability of Si-Cu interface will be investigated.
  - Effect of Li segregation induced embrittlement at the Si-Cu interface on the delamination of the a-Si thin film anode will be studied.
  - Effect of insertion of a thin elastic buffer layer between the a-Si thin film pattern and the Cu current collector on the stability of Si thin film patterned anode will be studied.
- **To understand the effect of the active material (nanostructured Si) geometry in Si-CNT heterostructured anode systems on its mechanical stability during electrochemical cycling.**

3.1 ORGANIZATION OF THE THESIS

In **Chapter 4.0** the details of the computational modeling framework are presented. The model is then employed to understand the effect of passive components (current collector and the Si-Cu interface) on the onset and propagation of the interfacial delamination of a 250 nm thick a-Si thin film anode (**Chapter 5.0 and 6.0**). In doing so, the goal is to provide and identify candidate current collector systems that will be conducive for effectively mitigating the deleterious effects of the catastrophic failure in Si. Furthermore, interfacial crack propagation in *a*-Si thin film electrode over multiple electrochemical cycles is simulated. Knowledge from these studies is further expanded by studying effect of a thin elastic buffer layer inserted between an a-Si thin film pattern and Cu current collector, on the mechanical stability of the anode configuration during electrochemical cycling (**Chapter 7.0**). In **Chapter 8.0**, the effect of Si geometry in the Si-CNT heterostructured anode is examined using the modeling framework to gain a fundamental insight into the various Si configuration dependent mechanical stability of Si-CNT heterostructures. The geometry of Si is systematically varied from a continuous coating to a particle in the shape of $1/8^{th}$ of a cylinder adhered to the CNT. Different active material geometries are compared for Li diffusion induced stresses and possible mechanical degradation during electrochemical cycling.

3.2 CONTRIBUTIONS

This dissertation thesis makes the following key contributions:

- The electrode-electrolyte interface reaction kinetics in Li-ion battery anode were modeled using the Butler-Volmer equation (**Section 4.1**). The open circuit potential of Si thin film anode was experimentally determined using Galvanostatic Intermittent Titration (GITT) (Figure 39). The capability of the modeling framework to predict Voltage-Capacity plot was demonstrated for Si thin film anode system (Figure 9, Figure 10).
- It was shown that plastic deformation of the underlying Cu current collector limits the delamination at the Si-Cu interface during electrochemical cycling of the Si thin film anode (Figure 16).
- Electrochemical cycling of Si thin film anode was simulated for 30 consecutive cycles to understand the evolution of interfacial delamination at Si-Cu interface during electrochemical cycling (Figure 18).
- For the first time, modified Mclean-Langmuir segregation kinetics was used to model the Li segregation induced embrittlement of the Si-Cu interface properties (Section 4.8). It was shown that the Li segregation induced interface embrittlement causes mechanical failure of Si thin film anode (Figure 20) validating the experimental observations.
- Effect of insertion of an elastic buffer layer between the patterned amorphous Si thin film and Cu current collector was examined using computational methods for the first time. It was shown that combination of certain buffer and interfacial mechanical properties can completely avoid interfacial delamination of the Si thin film pattern during its electrochemical cycling (**Figure 25**).

- The mechanical integrity of the Si-CNT heterostructured anode during electrochemical cycling was studied. The geometry of Si coating on CNT was varied systematically (Figure 28) and compared for possibility of void nucleation/grown in the active material (Figure 33, Figure 34 and Figure 35), thus providing design suggestions for CNT based heterostructured anodes.

4.0 COMPUTATIONAL FRAMEWORK

In this chapter, formulation of the computational modeling framework is presented. Equations detailing the electrode-electrolyte surface reaction kinetics, coupled diffusion – mechanical deformation and the mechanical failure (fracture/delamination) in the anode assembly are presented. For the definition of each variable, please see the nomenclature section.

4.1 REACTION KINETICS OF ELECTRODE-ELECTROLYTE INTERFACE

During the electrochemical cycling of the Li-ion battery, a reversible charge transfer reaction of $Li \rightleftharpoons Li^{+} + e^{-}$ occurs across the electrical double layer at the electrode-electrolyte interface (see Figure 4). When an active material is cycled over a time period of $2t$ under galvanostatic (constant current) conditions, the Li flux at the electrode-electrolyte interface is given as,

$$J_{Li} = \frac{i}{F} = \frac{Cm}{At} \tag{4.1}$$

where i is the current, F is the Faraday's constant, and C is the specific capacity of the active material with mass m and surface area A exposed to the electrolyte.

The reaction overpotential η_s is related to the rate of reaction (i.e. Li flux) according to the well-known Butler-Volmer equation as[71]

$$J_{Li} = \frac{i_0}{F}\left[\exp\left(\frac{\alpha_a F}{RT}\eta_s\right) - \exp\left(-\frac{\alpha_c F}{RT}\eta_s\right)\right] \tag{4.2}$$

Here, α_a and α_c are the anodic and cathodic transfer coefficients, respectively. R is the universal gas constant and T is the temperature. The exchange current density i_0 is expressed in terms of the concentration of electrolyte (c_e), electrode surface (c_s), and the maximum concentration

($c_{\max}$) of lithium according to

$$i_0 = k(c_e)^{\alpha_c}(c_{\max} - c_s)^{\alpha_a}(c_s)^{\alpha_c} \tag{4.3}$$

where k is the kinetic constant.

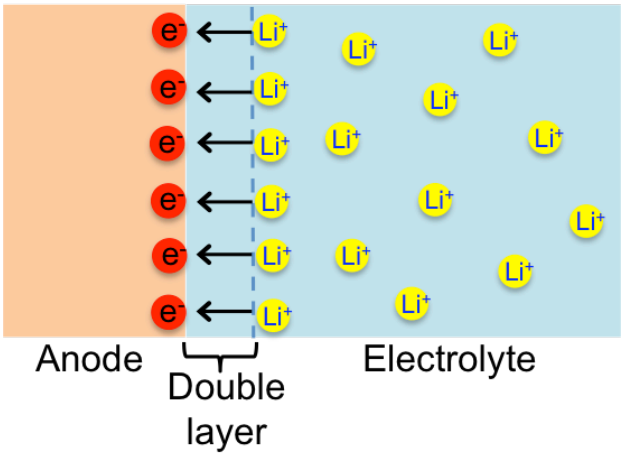

Figure 4. Schematics of the electrical double layer at the electrode-electrolyte interface.

In the formulation, solid-electrolyte interface (SEI) layer is assumed to form only in the first cycle. Further formation of SEI layer on the active material has been neglected. It is assumed that the SEI layer does not consume any Li ions and is ion-conductive. During the half-

cell testing, the electrodes are cycled against a Li reference electrode. Thus, the half-cell output voltage can be calculated as

$$V = U_{OCP} - \eta_s - R_c\, i\, A \tag{4.4}$$

where R_c is the contact resistance emanating from delamination of the active material from the current collector and U_{OCP} is the open circuit potential of the electrode at given Li concentration.

4.2 KINEMATICS OF ELECTRODE DEFORMATION

A body Ω_0 in its reference configuration having a material point with position vector $\mathbf{X}$ is considered as shown in Figure 5**.** The material point $\mathbf{X}$ is mapped to the point $\boldsymbol{x}$ in the spatial configuration Ω_t by the deformation map φ as $\boldsymbol{x} = \varphi(\mathbf{X}, \mathbf{t})$. The total deformation gradient $\mathbf{F} = \nabla_{\mathbf{X}}\varphi$ is multiplicatively decoupled into three parts as

$$\mathbf{F} = \mathbf{F}_e\mathbf{F}_p\mathbf{F}_\theta \tag{4.5}$$

where $\mathbf{F}_\theta$ is the deformation gradient solely due to insertion of lithium. The elastic distortion of the material is characterized by $\mathbf{F}_e$ while the inelastic deformation of the electrode is indicated by $\mathbf{F}_p$. The constitutive framework introduces two stress free intermediate states, $\bar{\Omega}_\theta$ and $\bar{\Omega}_{\theta p}$. For the sake of mathematical simplicity, a combined deformation gradient $\mathbf{F}_{\theta p} = \mathbf{F}_\theta\mathbf{F}_p$ is defined which maps a material point in Ω_0 to a point in stress free intermediate configuration $\bar{\Omega}_{\theta p}$. Therefore, the elastic deformation gradient can be written as $\mathbf{F}_e = \mathbf{F}\mathbf{F}_{\theta p}^{-1}$. The right Cauchy-Green tensor and its elastic counterpart can be given as

$$\mathbf{C} = \mathbf{F}^{\mathrm{T}}\mathbf{F},\ \mathbf{C}_e = \mathbf{F}_e^{\mathrm{T}}\mathbf{F}_e = \mathbf{F}_{\theta p}^{-\mathrm{T}}\mathbf{C}\mathbf{F}_{\theta p}^{-1} \tag{4.6}$$

The total jacobian, $J = \det(\mathbf{F})$, which also represents the volume change ratio of the material, can be multiplicatively decomposed similar to the deformation gradient as $J = J_e J_p J_\theta$. Here, $J_\theta = \det(\mathbf{F}_\theta) > 0$ is the electrode active material expansion due to Li insertion. Also, $J_e = \det(\mathbf{F}_e) > 0$ and $J_p = \det(\mathbf{F}_p) > 0$. Spatial velocity gradient can be introduced as

$$\boldsymbol{l} = \nabla_x \boldsymbol{v} = \dot{\mathbf{F}}\mathbf{F}^{-1} = \dot{\mathbf{F}}_e\mathbf{F}_e^{-1} + \mathbf{F}_e\dot{\mathbf{F}}_\theta\mathbf{F}_\theta^{-1}\mathbf{F}_e^{-1} + \mathbf{F}_e\mathbf{F}_\theta\dot{\mathbf{F}}_p\mathbf{F}_p^{-1}\mathbf{F}_\theta^{-1}\mathbf{F}_e^{-1} \tag{4.7}$$

with $\boldsymbol{v} = \dot{\boldsymbol{x}}$ denoting the spatial velocity. Pull back of the spatial velocity gradient $\boldsymbol{l}$ to the intermediate configuration yields

$$\mathbf{L} = \mathbf{F}_e^{-1}\boldsymbol{l}\mathbf{F}_e = \underbrace{\mathbf{F}_e^{-1}\dot{\mathbf{F}}_e}_{\mathbf{L}_e} + \underbrace{\dot{\mathbf{F}}_\theta\mathbf{F}_\theta^{-1}}_{\mathbf{L}_\theta} + \underbrace{\mathbf{F}_\theta\dot{\mathbf{F}}_p\mathbf{F}_p^{-1}\mathbf{F}_\theta^{-1}}_{\mathbf{L}_p'} \tag{4.8}$$

which can be additively decomposed into an elastic velocity gradient tensor $\mathbf{L}_e$, intercalation induced expansion velocity gradient $\mathbf{L}_\theta$, and a transformed plastic deformation gradient $\mathbf{L}_p'$.

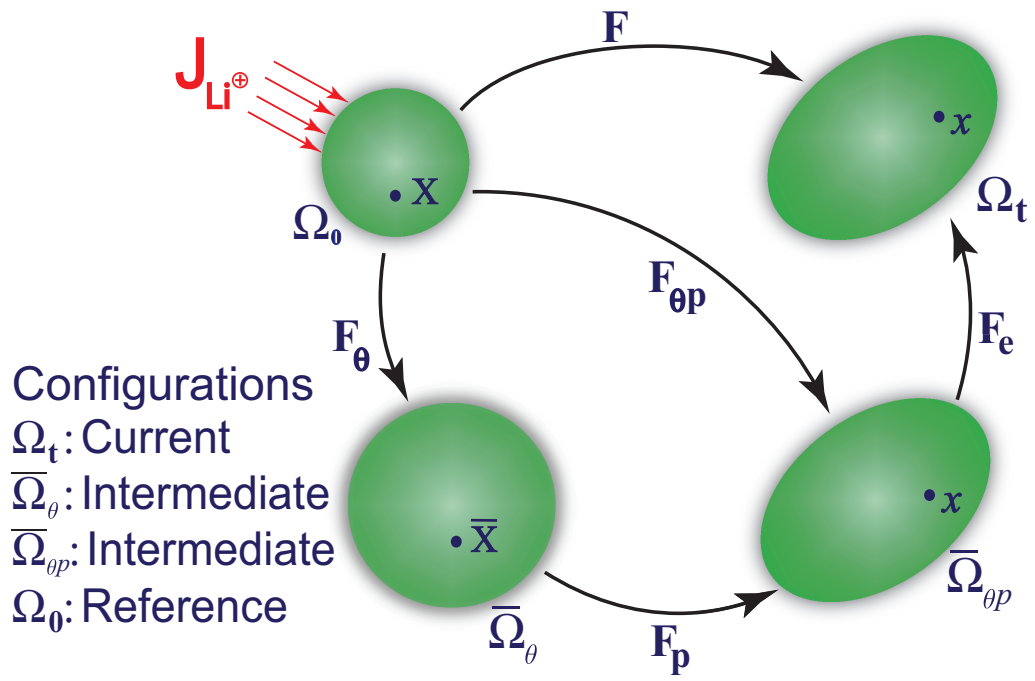

Figure 5. Graphical representation of multiplicative decomposition of Li intercalation (alloying) induced deformation gradient $\mathbf{F}$.

4.3 KINEMATICS OF LI INTERCALATION (LI ALLOYING)

Lithium insertion into the electrode results in its expansion, which depends on the nature of the crystal structure[72]. In case of amorphous materials (e.g. *a*-Si), lithium gets accommodated in arbitrary planes leading to homogenous expansion of Si[6]. Therefore, the deformation gradient resulting from Li insertion can be expressed as

$$\mathbf{F}_\theta = \left(1+\eta c\right)^{1/3}\mathbf{I} \tag{4.9}$$

with $\mathbf{I}$ being the identity tensor, $c\left(\mathbf{X},t\right)$ the concentration of the lithium atoms in the reference configuration, and η the expansion coefficient (or partial molar volume of solute) assuming

isotropic volume expansion. Thus, the intercalation induced volume expansion can be characterized as

$$J_\theta = 1 + \eta c \tag{4.10}$$

4.4 BALANCE EQUATIONS AND BOUNDARY CONDITIONS

For the galvanostatic cycling of the electrode, initial and boundary conditions for lithiation in the anode can be described as $c(\mathbf{X},0) = c_0(\mathbf{X})$ on $\partial\Omega_{0c}$, and $\mathbf{J}\cdot\mathbf{N} = J_{Li}$ on $\partial\Omega_{0J}$ (the electrode surface exposed to the electrolyte) with $c_0(\mathbf{X})$ as the initial concentration of lithium in the anode, J_{Li} as the flux of lithium atom at point $\mathbf{X}$ on the electrolyte-anode interface $\partial\Omega_{0J}$ with normal $\mathbf{N}$. In case of potentiostatic cycling conditions, the initial concentration condition remains the same ($c(\mathbf{X},0) = c_0(\mathbf{X})$ on $\partial\Omega_{0c}$), while the boundary condition on the surface exposed to the electrolyte is $c(\mathbf{X},0) = c_{max}$. Diffusion of lithium occurs at a much slower time scale; hence mechanical equilibrium is assumed to be already achieved. Therefore, the balance of linear momentum can be expressed as:

$$\nabla_X \cdot \mathbf{P} = \mathbf{0} \text{ with } \mathbf{P} = \mathbf{FS} \tag{4.11}$$

where $\mathbf{P}$ and $\mathbf{S}$ are the first and second Piola-Kirchhoff stress tensors, respectively. The boundary conditions for mechanical equilibrium are given as $\mathbf{P}\cdot\mathbf{N} = \boldsymbol{t}$ on $\partial\Omega_{0t}$, and $\boldsymbol{u} = \boldsymbol{u}_0$ on $\partial\Omega_{0u}$.

4.5 THERMODYNAMICS OF INTERCALATION

The free energy functional of the anode material can be assumed as

$$\Psi(\mathbf{F},c)=\Psi_1(\mathbf{F}_e,c)+\Psi_2(c) \tag{4.12}$$

In the above equation, $\Psi_1(\mathbf{F}_e,c)=\Psi_1(\mathbf{F},\mathbf{F}_\theta,\mathbf{F}_p,c)$ represents elastic free energy density of the electrode in the undeformed configuration that depends on overall deformation gradient (through $\mathbf{F}$) as well as concentration of lithium atom (through $\mathbf{F}_\theta$). Recent findings illustrate that elastic free energy density of crystalline as well as amorphous Silicon depends on the amount of intercalated lithium concentration[57]. To account for such dependence, Ψ_1 is also considered a function of Li concentration. The last term $\Psi_2(c)$, represents the chemical energy density of the anode material, which is a function of the concentration of lithium.

Time derivative of the free energy can be written as

$$\dot{\Psi}=\frac{\partial\Psi}{\partial\mathbf{F}_e}:\dot{\mathbf{F}}_e+\frac{\partial\Psi}{\partial c}\dot{c} \tag{4.13}$$

Inserting $\mathbf{F}_e=\mathbf{F}\mathbf{F}_{\theta p}^{-1}$ in the above equation, it can be rewritten as

$$\begin{aligned}\dot{\Psi}&=2\mathbf{F}_{\theta p}^{-1}\frac{\partial\Psi}{\partial\mathbf{C}_e}\mathbf{F}_{\theta p}^{-T}:\frac{\dot{\mathbf{C}}}{2}-\mathbf{M}_e:\mathbf{L}_{\theta p}+\frac{\partial\Psi}{\partial c}\dot{c}\\&=2\mathbf{F}_{\theta p}^{-1}\frac{\partial\Psi}{\partial\mathbf{C}_e}\mathbf{F}_{\theta p}^{-T}:\frac{\dot{\mathbf{C}}}{2}-\mathbf{M}_e:\mathbf{L}_\theta-\mathbf{M}_e:\mathbf{F}_\theta\mathbf{L}_p\mathbf{F}_\theta^{-1}+\frac{\partial\Psi}{\partial c}\dot{c}\end{aligned} \tag{4.14}$$

The second Piola-Kirchhoff stress (PK-II) tensor $\mathbf{S}_e$ and Mandel stress tensor $\mathbf{M}_e$ at the intermediate configuration is expressed as $\mathbf{S}_e=2\frac{\partial\Psi}{\partial\mathbf{C}_e}$ and $\mathbf{M}_e=\mathbf{C}_e\mathbf{S}_e$.

Using the intermediate PK-II stress tensor $\mathbf{S}_e$ along with the expression of expansion velocity gradient $\mathbf{L}_\theta$ for isotropic intercalation, the time derivative of the free energy can be recast as

$$\dot{\Psi} = \mathbf{F}_{\theta p}^{-1}\mathbf{S}_e\mathbf{F}_{\theta p}^{-T} : \frac{\dot{\mathbf{C}}}{2} - \mathbf{M}_e : \mathbf{F}_\theta \mathbf{L}_p \mathbf{F}_\theta^{-1} - \frac{1}{3}\eta \,\mathrm{tr}\left[J_\theta^{-\frac{2}{3}}\mathbf{M}_e\mathbf{F}_\theta^{-1}\right]\dot{c} + \frac{\partial \Psi}{\partial c}\dot{c} \tag{4.15}$$

In the above equation, the first part represents the work conjugate of the variation of the right Cauchy-Green tensor while second and third term represent the work conjugate of variation of concentration. From the second part, a pressure like quantity p at the reference configuration is defined as

$$p = \frac{1}{3}\mathrm{tr}\left[J_\theta^{-\frac{2}{3}}\mathbf{M}_e\mathbf{F}_\theta^{-1}\right] \tag{4.16}$$

For an irreversible process, the Second law of thermodynamic states that variation of entropy is always larger than or equal to the rate of entropic flux induced by diffusion: $T\dot{s} - \nabla\cdot(\mu\mathbf{J}) \geq 0$ where, s is the entropy density, $\mathbf{J}$ is the diffusion flux and μ is the chemical potential. Incorporating the Helmoltz free energy function $\dot{\Psi} = \frac{1}{2}\mathbf{S} : \dot{\mathbf{C}} - T\dot{s}$ and mass conservation of Lithium in anode, the Clausius-Duhem inequality for anode with isothermal condition can be written as

$$D = \mathbf{S} : \frac{\dot{\mathbf{C}}}{2} - \dot{\Psi} + \mu\dot{c} - \mathbf{J}\nabla\mu \geq 0 \tag{4.17}$$

Substituting the expression for free energy functional (Eq A.1), the above inequality can be expressed as

$$D = \left[\mathbf{S} - \mathbf{F}_{\theta p}^{-1}\mathbf{S}_e\mathbf{F}_{\theta p}^{-T}\right] : \frac{\dot{\mathbf{C}}}{2} + \mathbf{M}_e : \mathbf{F}_\theta\mathbf{L}_p\mathbf{F}_\theta^{-1} + \left[\mu - \frac{\partial\Psi}{\partial c} + \eta p\right]\dot{c} - \mathbf{J}\nabla\mu \geq 0 \tag{4.18}$$

From first part of the above inequality, the thermodynamically consistent definition of second Piola Kirchhoff stress tensor $\mathbf{S}$ in the reference configuration can be derived as $\mathbf{S} = \mathbf{F}_{\theta p}^{-1}\mathbf{S}_e\mathbf{F}_{\theta p}^{-T}$, where, $\mathbf{S}$ can be interpreted as the pull back of second Piola Kirchhoff stress tensor $\mathbf{S}_e$ from the intermediate configuration ($\bar{\Omega}_{\theta p}$) to the reference configuration (Ω_0) configuration (see Figure 5). The second part offers the plastic dissipative power $W_p = \mathbf{M}_e : \mathbf{F}_\theta \mathbf{L}_p \mathbf{F}_\theta^{-1}$. The third part of the inequality offers the expression of the chemical potential μ in the reference configuration as

$$\mu = \frac{\partial \Psi}{\partial c} - \eta p \tag{4.19}$$

From the above equation it can be easily noticed that the chemical potential is coupled with the mechanical field variables though the pressure like quantity as defined in Equation (4.16). Furthermore, the inequality in Equation (4.18) can be ensured only when the fourth component is negative semi-definite, which offers the definition of intercalating lithium flux of anode in the reference configuration as

$$\mathbf{J} = -\mathbf{M}\nabla\mu \tag{4.20}$$

where the mobility $\mathbf{M}$ is a symmetric and positive definite tensor. In the case of crystalline material, the mobility tensor is highly anisotropic. For an amorphous material the isotropic mobility tensor is taken as $\mathbf{M} = M\mathbf{I}$. Thus, atomic flux can be restated as

$$\mathbf{J} = -M\nabla\mu = -M\nabla\left[\frac{\partial \Psi}{\partial c} - \eta p\right] \tag{4.21}$$

Assuming an ideal solution, the lithium flux can be further expressed as,

$$\mathbf{J} = -D\left[\nabla c + \frac{c}{RT}\nabla\left(\frac{\partial \Psi_1}{\partial c}\right) - \frac{\eta c}{RT}\nabla p\right] \tag{4.22}$$

where $D = MRT/c$ is the diffusivity of lithium atom in the anode material. Therefore, conservation of mass for lithium in the anode material can be given by

$$\partial_t c = \nabla D\left[\nabla c + \frac{c}{RT}\nabla\left(\frac{\partial \Psi_1}{\partial c}\right) - \frac{\eta c}{RT}\nabla p\right] \tag{4.23}$$

The above equation suggests that apart from concentration gradient, intercalation of lithium in the electrode depends on mechanical stress states, variation of elastic energy functional ($\Psi(c)$), and the expansion coefficient η. In the absence of these dependencies, this equation essentially reduces to Fick's law of diffusion. Solution of the above equation will offer the intercalation induced deformation gradient tensor $\mathbf{F}_\theta$.

4.6 INELASTIC RESPONSE OF THE ELECTRODE

In conjunction with the intercalation, inelastic response of the electrode is characterized by suitably defining (1) yield condition, (2) flow rule and (3) hardening/softening laws. The flow rule of electrode material is defined in terms of the plastic deformation gradient $\mathbf{L}_p$ as

$$\mathbf{L}_p = \dot{\mathbf{F}}_p \mathbf{F}_p^{-1} = \dot{\lambda}\mathbf{N}_p \quad \text{with} \quad \mathbf{N}_p = \frac{\partial g}{\partial \mathbf{M}_e} \tag{4.24}$$

where, $\mathbf{N}_p$ describes the direction of the plastic flow, and $\dot{\lambda}$ is the plastic rate parameter. In the above equation, g describes the potential function governing plastic evolution that depends on Mandel stress tensor $\mathbf{M}_e$. In the present formulation, the yield function for the isotropic linearly hardening case is assumed as the following type

$$f\left(\boldsymbol{M}_e, \bar{\varepsilon}_p\right) = \sqrt{\frac{3}{2}\boldsymbol{M}_e^d : \boldsymbol{M}_e^d} - \left[\sigma_y + H\bar{\varepsilon}_p\right] = 0 \tag{4.25}$$

with $\boldsymbol{M}_e^d$ as the deviatoric part of the Mandel stress tensor $\boldsymbol{M}_e$. The yield strength and hardening modulus are represented as σ_y and H, respectively.

4.7 MODELING OF INTERFACIAL DELAMINATION

The spontaneous nucleation and propagation of an interfacial crack at the active material - inactive material interface (e.g. Si-Cu, Si-CNT) is simulated using the cohesive zone modeling technique[68-70, 73-77]. This particular technique assumes that there is a process zone ahead of the crack tip where the material degrades monotonically towards complete failure to advance the crack. In its classic form, this degradation is assumed to be solely of mechanical origin. Following the approaches adopted by Ortiz and Pandolfi[70] the deformed cohesive surface $\boldsymbol{\Gamma}_c$ (see Figure 6 **(a)**) is defined in terms of the mean deformation gradient $\bar{\boldsymbol{\varphi}}(\mathbf{X}, t) = [\varphi^+(\mathbf{X}, t) + \varphi^-(\mathbf{X}, \mathbf{t})] / 2$ and $\varphi^{\pm}(\mathbf{X}, \mathrm{t}) = \bar{\boldsymbol{\varphi}}(\mathbf{X}, t) + \delta / 2$. The normal and tangential components of the displacement jump vector $\boldsymbol{\delta}$ are

$$\delta_n = \boldsymbol{\delta} \bullet \mathbf{n},\ \delta_s = \mid \boldsymbol{\delta} - \delta_n \mathbf{n} \mid \tag{4.26}$$

where $\mathbf{n}$ is the unit normal on the cohesive surface and $\boldsymbol{a} \otimes \boldsymbol{b} = a_i b_j$. The traction separation law takes the following form:

$$\boldsymbol{t}_{\mathbf{c}} = \frac{t_c}{\delta_e}\hat{\boldsymbol{t}},\ \hat{\boldsymbol{t}} = [\beta^2 \boldsymbol{\delta} + (1 - \beta^2)(\boldsymbol{\delta} \bullet \mathbf{n})\mathbf{n}] \tag{4.27}$$

The above law is based on the effective opening displacement and associated effective traction. The effective opening displacement is defined as $\delta_e = \sqrt{\beta^2 \delta_s^2 + \delta_n^2}$ with β as the weighting parameter. The effective traction t_e is derived from the cohesive potential as $t_e = \partial \Phi / \partial \delta_e$. In the present work a computationally convenient cohesive potential is considered as:

$$\Phi = \exp(1)\sigma_c \delta_c \left[1 - \left(1 + \frac{\delta_e}{\delta_c}\right)\exp\left(\frac{-\delta_e}{\delta_c}\right)\right] \tag{4.28}$$

which leads to the effective cohesive traction as:

$$t_e = \exp(1)\sigma_c \frac{\delta_e}{\delta_c}\exp\left(\frac{-\delta_e}{\delta_c}\right) \tag{4.29}$$

In the above equation, σ_c is the maximum cohesive normal traction and δ_c is a characteristic opening displacement. The graphical representation of the chosen cohesive law is shown in Figure 6 **(b)**.

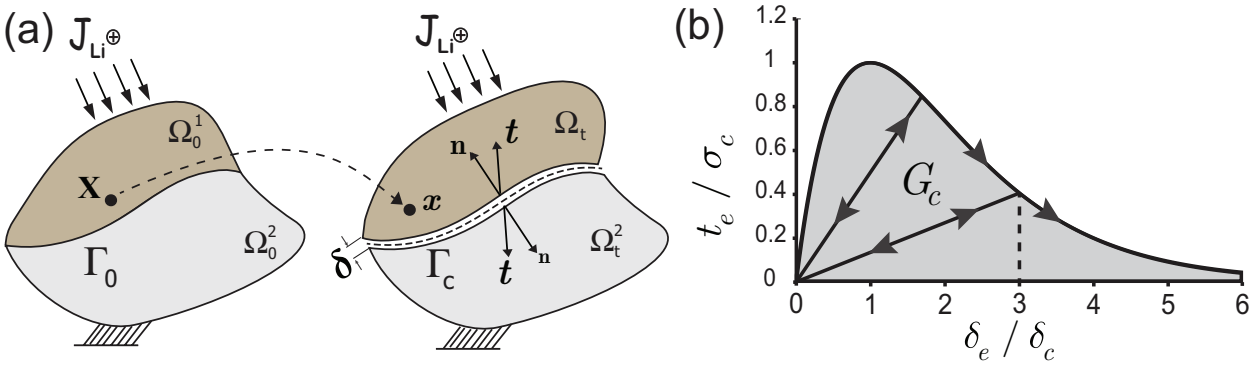

Figure 6. (a) Mathematical domain with reference and deformed configuration. (b) Schematics of the traction-separation law[70].

The model contains an internal variable $\dot{\delta}_{e,max}$ to account for energy dissipation. The evolution of $\dot{\delta}_{e,max}$ is given as:

$$\dot{\delta}_{e,max} = \begin{cases} \dot{\delta}_e & \text{if } \delta_e = \delta_{e,max} \text{ and } \dot{\delta}_e \geq 0 \\ 0 & \text{otherwise} \end{cases} \tag{4.30}$$

The unloading of cohesive zone is characterized as:

$$t_e = \frac{t_{e,max}}{\delta_{e,max}} \delta_e, \text{ if } \delta_e < \delta_{e,max} \text{ or } \dot{\delta}_e < 0 \tag{4.31}$$

The fracture toughness of the interface is calculated as:

$$G_c = \int_0^\infty t_e \, \mathrm{d}\delta_e = \exp(1)\sigma_c \delta_c \tag{4.32}$$

Complete delamination of the cohesive interface is considered when effective traction at the interface becomes zero. In the present study, delamination (fracture) is characterized by a parameter denoted as the delamination index (DI), which is measured in terms of the characteristic opening displacement δ_c with the following conditions:

$$DI = \begin{cases} \delta_e \,/\, 6\delta_c & \text{if } \delta_e < 6\delta_c \\ 1 & \text{if } \delta_e \geq 6\delta_c \end{cases} \tag{4.33}$$

It should be noted that during interface closure ($\delta_n < 0$), cohesive surfaces are subjected to contact constraint. The penetration of interfaces is restricted through a penalty traction that depends on the negative normal displacement jumps. Also, the delamination model incorporates interfacial adhesion strength through a prescription of maximum traction σ_c that can be achieved, as well as surface energy through the fracture toughness G_c. Thus it can closely mimic physical situations and simulate a wide range of interface conditions ranging from perfectly

bonded ones that do not allow any delamination to very weak cases that separate easily. The framework is not limited to simulating only interfacial delamination. It can also be used to simulate fracture in the bulk of the material for the known fracture properties (fracture strength and toughness).

4.8 MODELING OF LI SEGREGATION INDUCED EMBRITTLEMENT

The presence of segregated species near the interface has an additional effect on the decohesion process and often manifests itself by a reduction in the work of separation of the interface. To obtain this law, the existence of a Helmholtz type surface potential Φ in terms of Gibbs-like excess quantities is assumed as[78-80]

$$\Phi = \boldsymbol{t}_{\mathbf{c}}\mathrm{d}\boldsymbol{\delta} + \mu_s \mathrm{d}\Gamma \tag{4.34}$$

In this equation, μ_s stands for the chemical potential of the segregant, and Γ denotes its interfacial excess. Note that the displacement jump $\boldsymbol{\delta}$ in the above equation can be thought of as an excess interfacial displacement to keep the definition of the potential in the spirit of Gibbs adsorption isotherm.

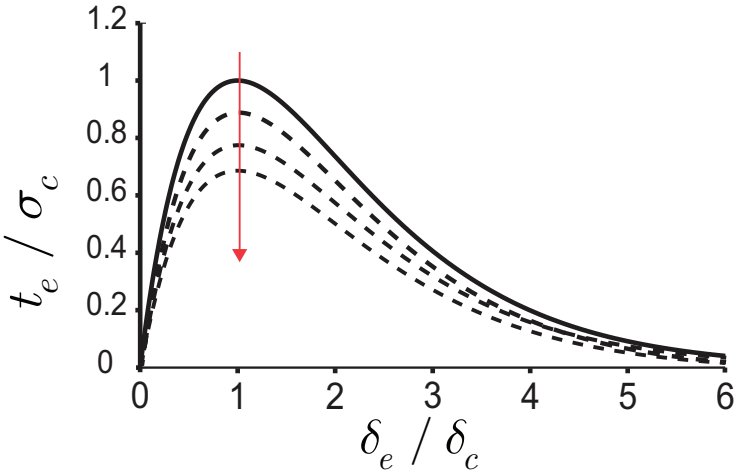

Figure 7. Interfacial traction separation law showing the effect of segregation induced embrittlement. Gradual reduction of the fracture strength σ_c (and correspondingly fracture toughness G_c), indicated by the red arrow, takes places as the embrittlement of the interface progresses.

Segregation of lithium atoms in the process zone further assists crack propagation through a net reduction of the fracture toughness. This reduction in toughness due to Li segregation can be computed as [79]

$$(\Delta G_c) = wRT\Gamma^0 \left(\ln \frac{(1-\theta_b)}{(1-\theta_t)} - \frac{1}{2}(\theta_b + \theta_t) \ln \frac{(1-\theta_s)}{(1-\theta_t)} \right) \tag{4.35}$$

where θ_t is the current Li interfacial coverage and θ_b is the Li interfacial coverage at the start of electrochemical cycle. The maximum attainable interfacial coverage of segregate is θ_s, while Γ^0 is the saturation excess. Li coverage at the interface is calculated as $\theta_t = c(x,t)/\Gamma^0$, where Γ^0 is the surface saturation excess, and $c(x,t)$ is given by Equation (4.36) as described below. For the derivation of Equation (4.35), ideal conditions for the segregation in a binary system have been assumed.

Experimental observations[12] reveal the presence of Cu_2LiSi precipitates in the interfacial region that may alter the extent of embrittlement due to ideal segregation and thus may not allow the full reduction in fracture toughness as predicted by the above equation. Accordingly, an embrittlement factor w is introduced that controls the rate of interface embrittlement. A value of zero for this factor signifies no embrittlement mechanisms due to lithium segregation are operative, while $w=1$ indicates ideal segregation conditions. Atomistic calculations[81] have suggested that the reduction in toughness is typically realized through a reduction in the maximum cohesive strength. Accordingly, the cohesive law for the interface in the presence of segregation mechanisms is modified as presented in Figure 7**.**

Finally, the quantification for the amount of segregant present in the interface is needed so that the interfacial coverage θ_t can be calculated. This can be achieved by the consideration of various forms of segregation kinetics available in the literature[82]. While sophisticated segregation kinetics models exist in the literature, the presented computational framework accounts for the segregation of Li at the Si anode and Cu current collector interface using McLean segregation kinetics[83]. This particular model is chosed as it is numerically simple, but incorporates all the essential features of the segregation phenomenon. The original expression for this kinetics is provided for the case of constant concentration of the solute in the bulk. However, during galvanostatic charge-discharge for the anode, concentration of lithium will vary temporally in the vicinity of the interface throughout the electrochemical cycle. Accordingly, this expression is modified to take into account this variation in the boundary condition as described below.

Note that a length scale needs to be introduced for the calculation of surface coverage as the concentration of lithium in the bulk is given in terms of unit volume while the surface

coverage requires the unit of area. This is taken into account by the interfacial thickness, Δ_i. In accordance with the assumption by McLean[83], as the interface volume is small compared to the Si thin film volume, the interface is assumed to be fed with Li atoms from a narrow region in the thin film close to the interface. The governing the rate of segregation at the interface of thickness Δ_i can be described by the diffusion equation

$$c_t = Dc_{xx} \quad 0 \le x \le \Delta_i, 0 < t < \infty \tag{4.36}$$

Initial concentration of lithium at the interface is taken to be zero i.e. $c(x,0) = 0$, as no lithium may reach the interface at the beginning of the electrochemical cycle. With the progress of lithiation and subsequent delithiation, Li concentration inside the Si bulk adjacent to the interface can be described as a function of time, $c(0,t) = f(t)$, and can be obtained from the solution of the coupled transport equation as described in **Section 4.5**.

Solution of Equation (4.36) along with the initial and boundary conditions expressed above furnishes the concentration of Li at the interface as

$$c(x,t) = \int_0^t \frac{x}{4\pi D(t-s)} \exp\left(-\frac{x^2}{4D(t-s)}\right) f(s)ds \tag{4.37}$$

where D is the diffusivity of Li in Si.

The above-described framework is employed in a nonlinear finite element framework to solve for the intercalation of lithium into a solid domain and associated stress generation. Further details of the finite element implementation are given in **Appendix A-C**. The framework is verified against analytical solutions[43] for Li diffusion and diffusion induced stresses generated in a spherical electrode particle under galvanostatic and potentiostatic conditions (see **Appendix D**). It should be noted that application of this framework is not limited to performing analysis of electrodes in Li ion batteries, but can be applied to

understand diffusion induced stresses in insertion based electrodes in other battery chemistries such as Na ion, Mg ion, etc., This framework can also be used to analyze other problems involving the phenomenon of solid diffusion (e.g. dopant diffusion in semiconductors[84]). Furthermore, systems involving conductive heat transfer can also be investigated for thermal stresses using the analogy between heat transfer and mass transfer.

5.0 UNDERSTANDING THE EFFECT OF CURRENT COLLECTOR PROPERTIES ON THE DELAMINATION OF AMORPHOUS-SILICON

5.1 INTRODUCTION

With the growing energy storage demands and continued miniaturization of advanced portable and consumer systems, there is a stringent need for longer lasting portable energy storage systems with high energy and power densities. Among the different materials studied to replace the existing state of the art graphite anode (capacity 372 $mAhg^{-1}$), silicon has been the forerunner due to its high theoretical capacity of ~4200 $mAhg^{-1}$. In past decade, *a*-Si thin film electrodes have been extensively researched due to their ease of fabrication and near theoretical performance (~3600 $mAhg^{-1}$)[19, 20]. Experiments show that after the first electrochemical cycle, *a*-Si film exhibits through-thickness cracks resulting in separate islands attached to the current collector[12]. However, after a few cycles, the capacity drops precipitously as the islands delaminate entirely from the metallic current collector resulting in complete loss of performance. Hence, the Si-Cu interface stability is a direct criterion to retain the anode capacity.

Modification of the substrate surface morphology to increase the adhesion of a-Si thin film with the substrate has shown to improve the cycling performance[24]. Annealing the a-Si thin film deposited on Cu substrate at high temperature is also known to improve the adhesion between the two surfaces by interdiffusion of Si and Cu[23]. Thus, it has been reported that better

attachment of thin film with the substrate delays the interfacial crack propagation resulting in lower capacity fade. Recently, patterning of the thin film has garnered attention as a possible avenue to mitigate delamination at the interface[16, 18, 85]. In a series of papers, Gao and coworkers have theoretically studied the effect of size of thin film islands on interfacial delamination[86-88]. They have determined the existence of a critical size of the islands, below which delamination will not occur and further propagate.

Another strategy to suppress delamination that has not garnered much attention yet is the proper choice of current collector and its mechanical properties to safely accommodate the stresses generated during electrochemical cycling of the anode. Recent experiments show that the presence of an interfacial layer of amorphous carbon between a-Si thin film and substrate results in excellent capacity retention of the thin film anode[21]. Motivated by this observation, a systematic study of the effect of mechanical behavior of the current collector on the onset and propagation of the interfacial delamination of the thin film anode is carried out. The modeling framework described in **Chapter 4.0** is utilized to demonstrate the effect of substrate mechanical properties on the delamination of the thin film from the current collector. Elastic modulus and yield strength are selected as the two essential mechanical properties to effectively categorize the performance of the candidate current collector materials. In doing so, the goal is to provide and identify candidate current collector systems that will be conducive for effectively mitigating the deleterious effects of the catastrophic failure in Si.

5.2 PROBLEM DESCRIPTION

The numerical model presented in **Chapter 4.0** has been used to simulate the electrochemical and mechanical response of the silicon thin film along with the current collector as well as the interface between them. After the first electrochemical cycle, *a*-Si film exhibits through-thickness cracks forming separate islands attached to the current collector (see schematics in Figure 8 **(a)**)[12]. After stabilization of this crack pattern, the stresses generated in the film are not sufficient to generate additional vertical cracks[13]. However, further electrochemical cycling affects mechanical integrity of the anode configuration through the propagation of interfacial cracks that may peel the silicon island from the current collector. As maintaining the electrical contact between Si film and current collector is important, interfacial delamination at Si-Cu interface is an important criterion to quantify the mechanical integrity of the electrode.

In this study the focus is on the delamination of a single Si thin film island subjected to electrochemical cycling similar to the experimental conditions adopted by Maranchi et al.[19]. To simulate the delamination of *a*-Si thin film from the current collector, a three-dimensional domain as shown in Figure 8 **(b)** is considered, where the substrate represents the current collector and the island on top of substrate represents the Si thin film. Separation between the vertical cracks formed in the thin film during first electrochemical cycle has been observed to be in the micron range[12]. Thus a 1 μ m square thin film island of 250 nm thickness is considered for the modeling purpose. Three-fold larger dimension is considered for the current collector so that its boundaries do not influence the stress field in and around the interface between the film and substrate. For the galvanostatic charging and discharging, a constant Li-ion flux is applied through the top surface of the *a*-Si island as shown in Figure 8 **(b)**. Taking advantage of the

symmetry, only 1/4th of the domain presented in Figure 8 **(c)** is considered to minimize the computational burden.

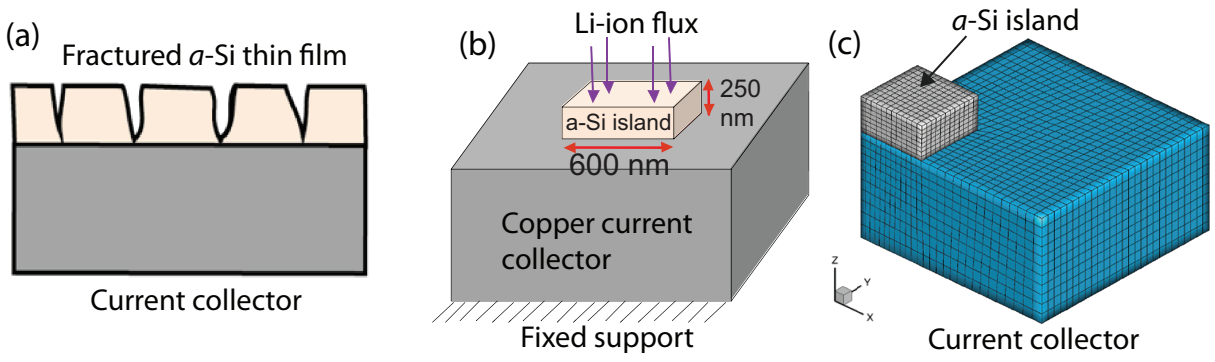

Figure 8. (a) Vertically fractured a-Si thin film anode after 1st electrochemical cycle. (b) Domain representing a single a-Si island on the current collector with Li flux from top (c) Finite element mesh of 1/4th of the a-Si island and current collector domain.

The electrode is cycled in the voltage window of 1.2 to 0.02 V at C/2.5 charge rate. The open circuit potential U_{OCP} is determined experimentally (For details, see **APPENDIX E**). The material properties of the Si film and the interface considered for simulation are reported in Table 1. The materials are modeled as compressible Neo-Hookean materials. A functional dependence of the Young's modulus on the lithium concentration is adopted as $E^{Si}\left(Li_{fraction}\right) = E_0^{Si} - \omega \times Li_{fraction}$, where $Li_{fraction}$ is the fraction of Li atoms present in the *a*-Si film[57]. The current collector is taken to be of elasto-plastic nature so that it can exhibit fully recoverable elastic deformation as well as permanent plastic deformation.

To analyze the effect of mechanical properties of the current collector on the delamination response of the thin film, its Young's modulus is varied from 9 GPa to 120 GPa. Further, to investigate the effect of onset of plastic flow of the current collector on interfacial

delamination, its yield strength is varied widely from 70 to 1000 MPa, while keeping the hardening parameter constant. As only the effect of substrate properties on the delamination is explored, properties of the interface are kept constant. A moderately strong interface with a fracture toughness of 25 Jm^{-2} and strength 2 GPa is chosen as reported in literature[12].

Table 1. Values of material parameters for simulation of *a*-Si thin film anode

Parameter	**Value**	**Parameter**	**Value**
c_e	1000 mol m^{-3}	H	5 GPa
c_{max}	3.651×10^5 mol m^{-3}	k (lithiation)	1.55×10^{-13} $m^{2.5}$ s^{-1} $mol^{-0.5}$
D	10^{-16} m^2s^{-1} [89]	k (delithiation)	60×10^{-13} $m^{2.5}$ s^{-1} $mol^{-0.5}$
E (silicon)	90 GPa	F	96485.34 C mol^{-1}
ν (silicon)	0.28	R	8.314 $JK^{-1}mol^{-1}$
ω	71.25 GPa [57]	T	298 K
σ_c	2 GPa	α_a,α_c	0.5
G_c	25 Jm^{-2}	η	4.5×10^{-6} m^3mol^{-1}

5.3 RESULTS

The results of a detailed parametric study of the effect of mechanical properties of the current collector on the delamination behavior of the thin film during electrochemical cycling are presented in following section for a single electrochemical cycle closely mimicking half-cell experiments. Since the formation of SEI layer and associated irreversible capacity loss as well as

the formation of islands due to vertical cracking of the thin film during the first electrochemical cycle are neglected in this analysis, simulations are reported for the 2nd charge/discharge cycle.

5.3.1 Experimental calibration of rate constants

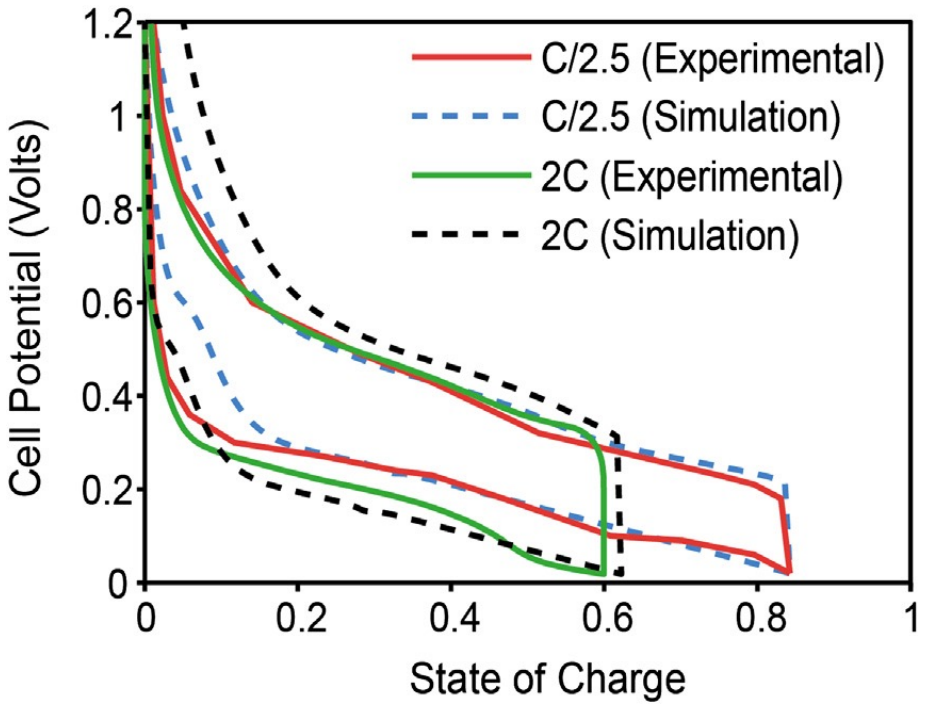

Figure 9. Comparison of experimental and simulated voltage-capacity plots for C/2.5 and 2C charge rate.

Reaction rate constant k to be used in the Butler-Volmer expression depends strongly on the anode configuration and experimental set up. To obtain a better estimate of this parameter, the simulated voltage-capacity curve is calibrated for a particular charge rate against experimental results reported in literature [19]. These experimental data is reported for a 250 nm a-Si thin film at $C/2.5$ and $2C$ charge rates. It was found that $k = 1.55 \times 10^{-13}\ \mathrm{m^{2.5}\,s^{-1}\,mol^{-0.5}}$ for lithiation and $k = 60 \times 10^{-13}\ \mathrm{m^{2.5}\,s^{-1}\,mol^{-0.5}}$ for the corresponding delithiation appear to be in excellent agreement with the experimental values for the 0.02-1.2 V voltage window, except at the onset of lithiation

for $C/2.5$ charge rate (Figure 9). Using the same parameters, the voltage profile for $2C$ charge rate is simulated and found to be in good agreement with the experimental results.

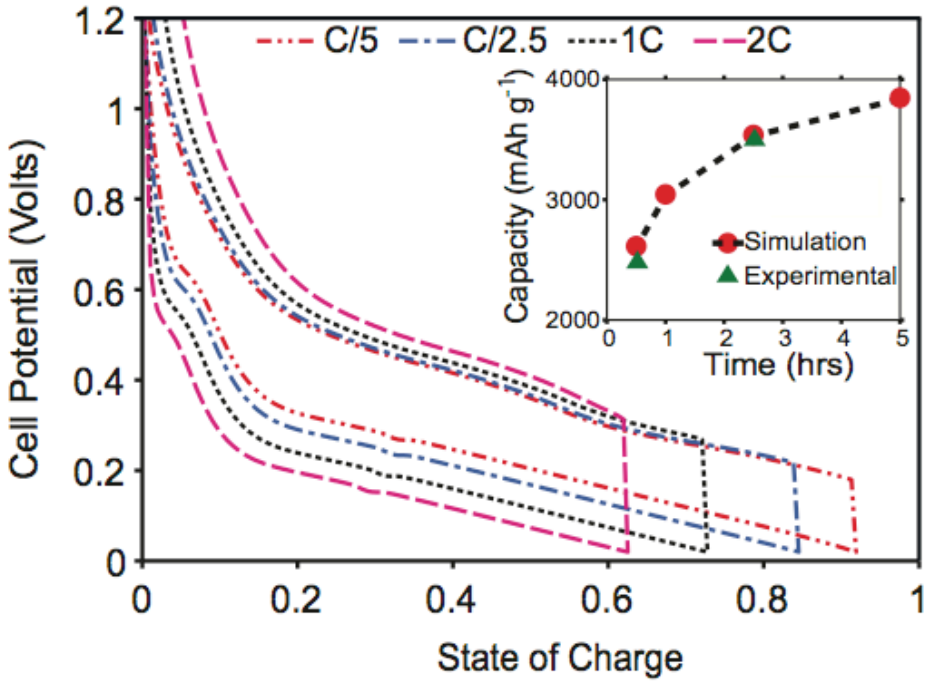

Figure 10. Comparison of a-Si anode half-cell potential vs. SOC at different charge rates. Inset compares the simulated and experimental capacities at different charge rates.

5.3.2 Voltage-Capacity simulation at various charge rates

To further investigate the validity of the estimated parameters and demonstrate model predictive capability, calibrated model from the last section has been utilized herein to predict the voltage-capacity curves at different $C-rates$. Figure 10 shows the effect of charge rates on the voltage-capacity curve. It can be observed that the electrochemical cycling at $C/5$ rate shows a 91.6% state of charge (SOC) while only 62% SOC can be achieved with $2C$ rate. This is to be expected as lithiation is carried out in shorter duration causing higher Li flux at $2C$ rate

compared to $C/5$ rate, and thus develops a comparatively higher concentration gradient inside the bulk of the thin film. This fact results in an increased over-potential due to kinetic limitations at higher charge rates and the lithiation cut-off voltage (0.02 V) is reached earlier limiting the deliverable capacity of the electrode. Maximum capacity at various charge rates was estimated and compared with the available experimental results (see inset in Figure 10). Maranchi *et al.* [19] experimentally observed an initial 2nd cycle reversible capacity of ~3500 $mAhg^{-1}$ for the charge rate of $C/2.5$ while that for a $2C$ charge rate was ~2500 $mAhg^{-1}$. The simulations predict the capacity of 3486 $mAhg^{-1}$ for the earlier case, and 2604 $mAhg^{-1}$ for the second one.

5.3.3 Mechanisms of silicon thin film delamination from the current collector

In order to understand how the current collector deforms and possibly contributes to the delamination behavior of the interface, two representative materials with disparate mechanical properties are considered. The first model material is chosen to be similar to graphite, which has a low modulus of elasticity of about 9 GPa and exhibits negligible plastic deformation; and another is similar to copper, a material with Young's modulus comparable to silicon (90 GPa) but possessing yield strength of 330 MPa.

Figure 11 shows the island and the elastic graphite substrate after completion of lithiation (Figure 11 **(a)**) and delithiation (Figure 11 **(b)**). Note that the thin film undergoes considerable deformation in the lateral directions during lithiation. Also, as the edges as well as the top of the island are free, the film bends in a convex upward manner and consequently deforms the current collector. However, as the substrate is very soft, it also deforms elastically to follow the island, and thus the interfacial displacement jump is minimal. Insets in the figure show the contours of Delamination Index (DI), the normalized effective displacement jump. DI<1.0 indicates no

interfacial delamination while DI=1.0 indicates complete delamination leading to loss of material contact (see Equation (4.33)). Note that maximum value of DI does not exceed 0.07. As a consequence, the interface remains intact and does not show any delamination. During delithiation the thin film as well as the current collector recover elastically and go back to their original configuration. The stress state in the system follows a reverse chronological path as compared to lithiation, and thus does not exhibit any delamination in this phase of the electrochemical cycling.

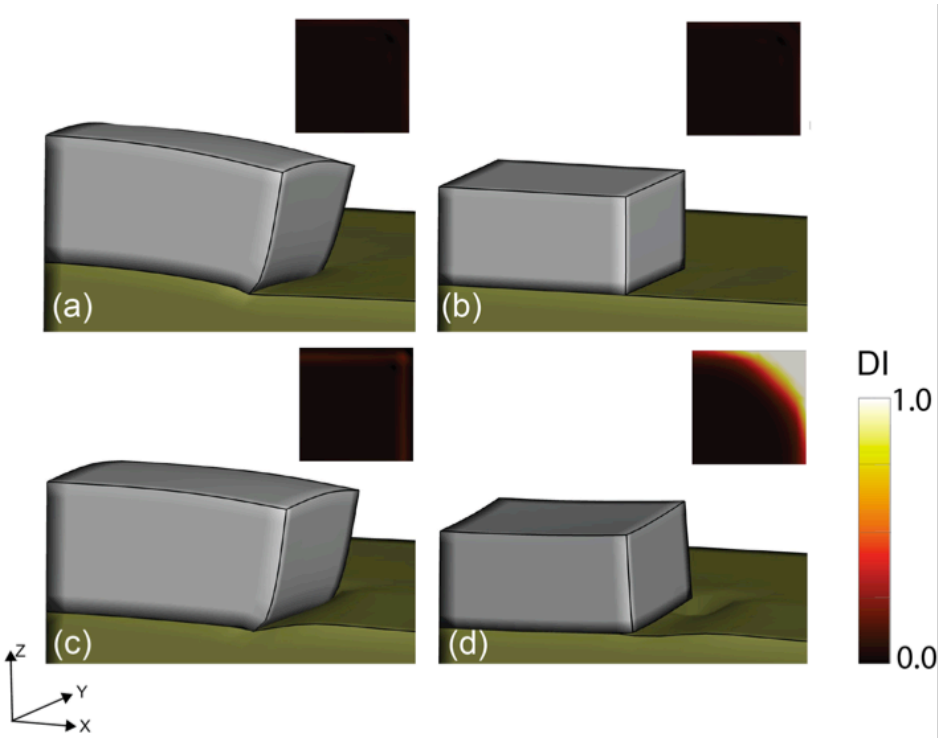

Figure 11. Silicon island and graphite current collector at the (a) end of lithiation and (b) end of delithiation. Silicon island and copper current collector at the (c) end of lithiation and (d) end of delithiation. The contour plot in inset of each figure shows the delamination index (DI) mapped on the silicon film-current collector interface.

The mechanical state for the elasto-plastic substrate with properties similar to copper is completely different. Deformation patterns for the island after completion of lithiation as well as delithiation are shown in Figure 11 **(c) and (d)**, respectively. Note that, in contrast to the previous figure, clear delamination can be observed for this case at the end of delithiation. The delamination starts at the corner of the island during delithiation and subsequently propagates towards the center. For the elasto-plastic substrate, stresses in the vicinity of the *a*-Si island base reaches its yield strength rather early during lithiation. Therefore, considerable plastic flow of copper occurs and continues till the end of lithiation. During de-lithiation, elastic recovery of the current collector is initiated albeit substantially lower in magnitude compared to the permanent plastic deformation already achieved. Therefore, the copper substrate retains the indentation mark at the edges of the island where the plastic deformation is maximum; **see** Figure 11 **(d)**. Such observation has been reported experimentally[18]. The contours of plastic strain on the current collector surface at the end of lithiation as well as delithiation are shown in Figure 16 **(d) and (e)**, respectively.

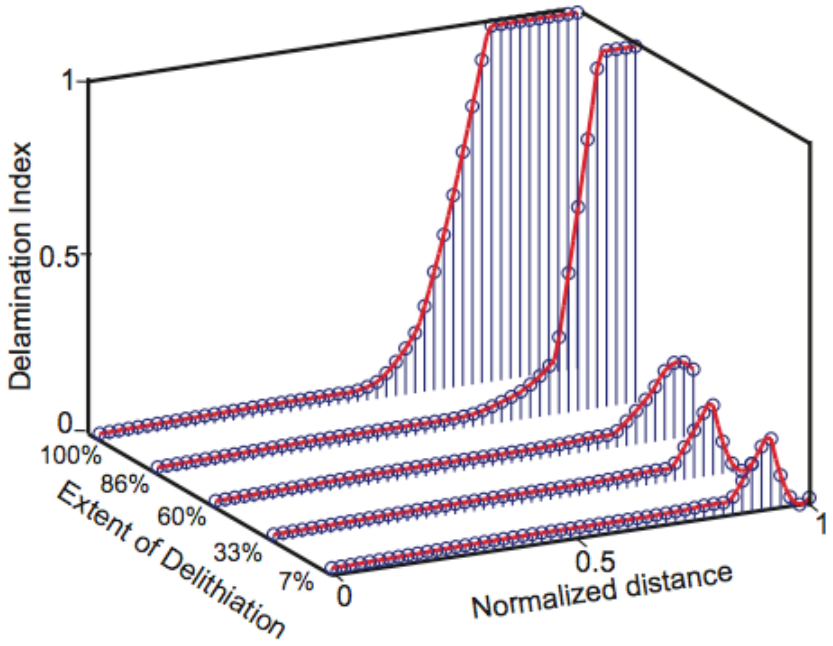

Figure 12. Propagation of delamination front along normalized distance from the center (indicated as 0) to the corner (indicated as 1) of the island-current collector interface at different extent of delithiation.

These figures also reinforce our observation that considerable inelastic deformation occurs in the current collector during electrochemical cycling. Figure 12 shows the evolution of DI during delithiation along a straight line from the center to the corner of the island. The normalized distance along this straight line is 0 for the center and 1 for the corner, respectively. This figure clearly shows that while interfacial displacement jump is minimal at the start of delithiation, it increases rapidly to the state of complete delamination ($DI=1$) at the corner of the island after about $2/3^{rd}$ of the delithiation phase. After its initiation, the delamination front propagates rapidly from the corner towards the center of the interface throughout the rest of the delithiation process. It can be concluded from the above discussion that properties of the current collector exert a profound effect on the mechanical integrity of the interface. In the following sections, these effects are studied in further detail.

5.3.4 Effect of current collector elastic modulus on interfacial delamination

To focus on the effect of elastic deformation of the current collector on the interfacial delamination, the current collectors that can undergo only elastic deformation but no plastic deformation are considered. The elastic modulus of the substrate is varied from 9 GPa to 120 GPa keeping the film elastic modulus constant at 90 GPa. Extent of the delamination of the interface as a percentage of the entire interfacial area has been recorded and is shown in Figure 13 for different substrate moduli. It is interesting to note that while cases with low current collector elastic modulus do not show any delamination at all, those with moduli greater than $1/3^{rd}$ of that of the film undergo complete delamination. It is found that delamination initiates during lithiation phase, and propagates through the entire interface readily after initiation. As discussed in the last section, soft substrates (< 30 GPa) can undergo very large deformation and thus interfacial stresses may not exceed the adhesion strength of the interface. However, stiffer current collectors produce higher stresses at the interfacial region and once the crack is nucleated it is driven through the entire interface, as no other energy dissipating mechanism is present. Thus, while soft elastic substrates (< 30 GPa) can prevent the onset of delamination, the situation differs entirely for elastic substrates with moderate to high stiffness: Delamination is catastrophic for these cases resulting in complete loss of electrochemical capacity.

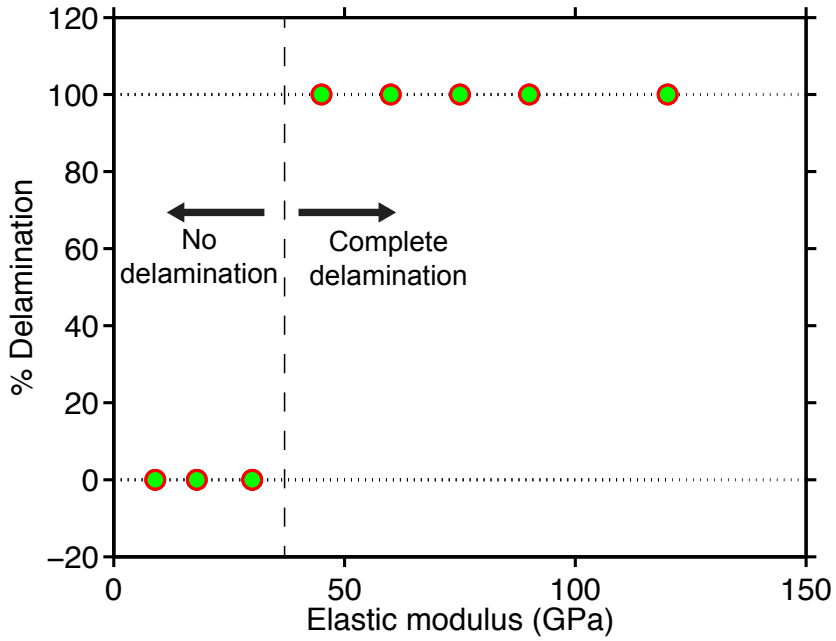

Figure 13. Percentage of delamination for different Young's moduli of an elastic substrate. Regime of no delamination and complete delamination regime are approximately marked by the vertical dashed line.

5.3.5 Effect of current collector yield strength on the interfacial delamination

In this subsection, the case of elasto-plastic substrate materials is reported. The yield strength is varied from 70 MPa to 1000 MPa. Three particular instances of modulus are chosen, one with a low value of E=18 GPa denoted as case 1, and other two with 60 and 90 GPa marked as cases 2 and 3, respectively. Interestingly, the soft substrate material of case 1 that did not exhibit any delamination in the absence of inelastic deformation mechanisms, can now show considerable delamination (in excess of 10%) depending on its yield strength (Figure 14). The extent of delamination decreases rapidly with increasing yield strength and effectively vanishes for simulation materials with yield strength in excess of 1 GPa. However, substrates in cases 2 and 3 that exhibited complete delamination of the island during elastic only deformation mode undergo

only limited delamination when plasticity is present, see Figure 14. Thus, inelastic deformation mechanisms have opposing effects on the substrate materials that resided on complete delamination or no delamination regime as found from purely elastic analysis (Figure 13). Plasticity limited the extent of delamination for the class of materials with an elastic modulus of >30 GPa while introducing delamination for the softer ones (< 30 GPa elastic modulus).

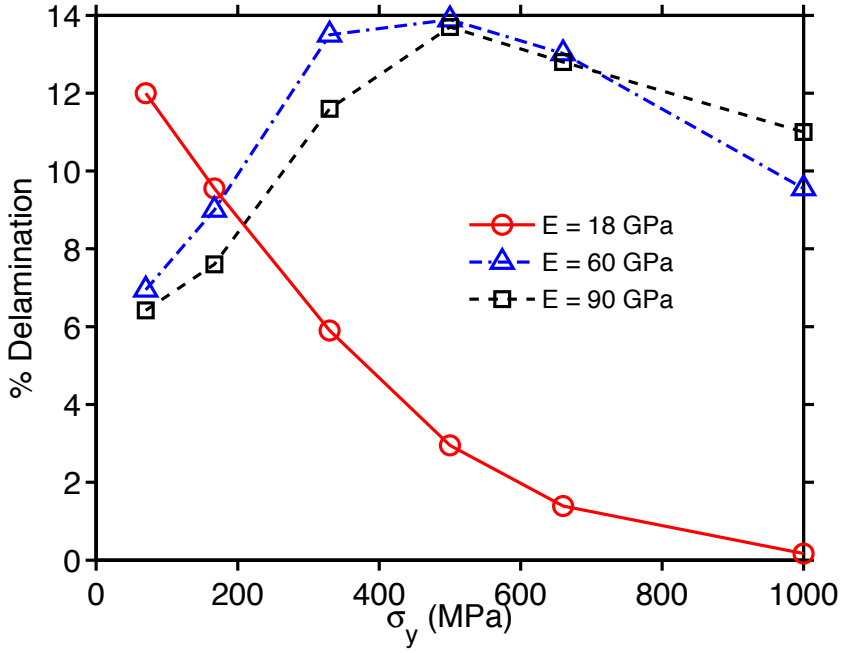

Figure 14. Variation of percentage of delamination at islande current collector interface with yield strength of elasto-plastic current collector. Simulations have been per- formed for three different elastic moduli of the current collector and are indicated by separate lines (18 GPa: solid line, 60 GPa: dash-dot line and 90 GPa: dashed line).

These findings were further explored by performing a parametric study on the extent of delamination by varying the elastic modulus of the current collector from 18 GPa to 120 GPa. Three instances of yield strength values chosen from its feasible range are presented the results in Figure 15**.** Note from this figure that for softer substrates (<30 GPa), an increase in yield

strength decreases the extent of delamination while opposite is true for substrates with higher modulus reinforcing our earlier observation. For all three cases of yield strength considered, the extent of delamination initially increases to reach a peak value as the elastic modulus is increased. A further increase in the modulus reduces the extent of delamination.

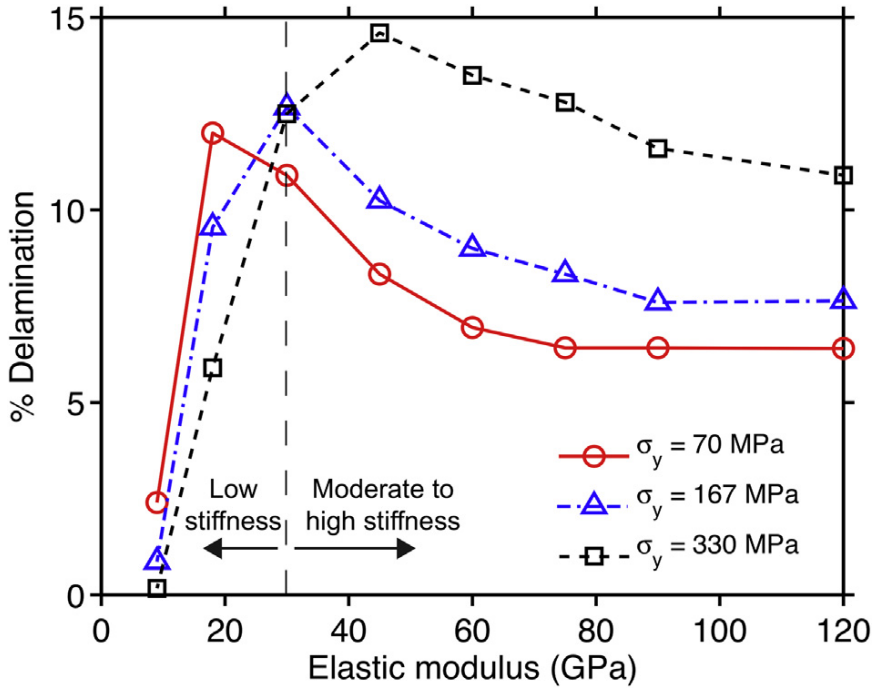

Figure 15. Variation of percentage of delamination at islandecurrent collector interface with Young's moduli of the elasto-plastic current collector. Simulations have been performed for three different yield strengths of the current collector and are indicated by separate lines (70 MPa: solid line, 167 MPa: dash-dot line, 330 MPa: dashed line).

A detailed study of the stress state and accumulated plastic strain in the substrate materials was undertaken to elucidate the observed extent of interfacial delamination presented above. In general, there are two competing energy dissipating mechanisms occurring at and in the vicinity of the interface: permanent deformation due to plastic flow of the current collector,

and creation of new surface due to delamination of the interface. During lithiation, stress state in the vicinity of the island corner remains compressive and shear dominant while during delithiation it becomes tensile and shear dominant. For the range of material properties studied, stress in the substrate typically exceeds the yield strength during lithiation. Plastic deformation of the current collector thus can be observed around the corner of the island for all cases. During delithiation, a complex interplay between these two competing mechanisms takes place that determines the ultimate extent of delamination at the interface.

Figure 16 summarizes the results of this study. A current collector material with the same elastic modulus as silicon (90 GPa), and another soft material with a modulus of 18 GPa is chosen. Three different values of yield strength are taken for each of them thus resulting in six distinct material property combinations as presented in the rows of the figure. First two columns in this figure correspond to accumulated plastic strain in the current collector in the vicinity of the island at the end of lithiation (left) and delithiation (center), respectively, while the right column represents the extent of delamination of the island-current collector interface. Observe that the stiffer material (top three rows) undergoes plastic deformation that allows it not to delaminate during lithiation as would be the case for the pure elastic case with same stiffness. It undergoes further plastic straining during delithiation relieving the stress around the interface. However, extent of this mode of deformation decreases as the yield strength is increased. As a consequence, the extent of interfacial delamination shows an increasing trend as the yield strength is increased.

The substrate with low stiffness value (bottom three rows) can undergo very high elastic deformation and thus can keep the interfacial stresses low throughout the electrochemical cycle. However, their elastic recovery during delithiation is hindered in the presence of plasticity thus

channeling the stored elastic energy towards dissipating mechanisms. Lower yield stress in these materials increases the extent of plastic deformation during lithiation thus making elastic recovery during delithiation more difficult. As a consequence, the extent of delamination increases with the yield stress.

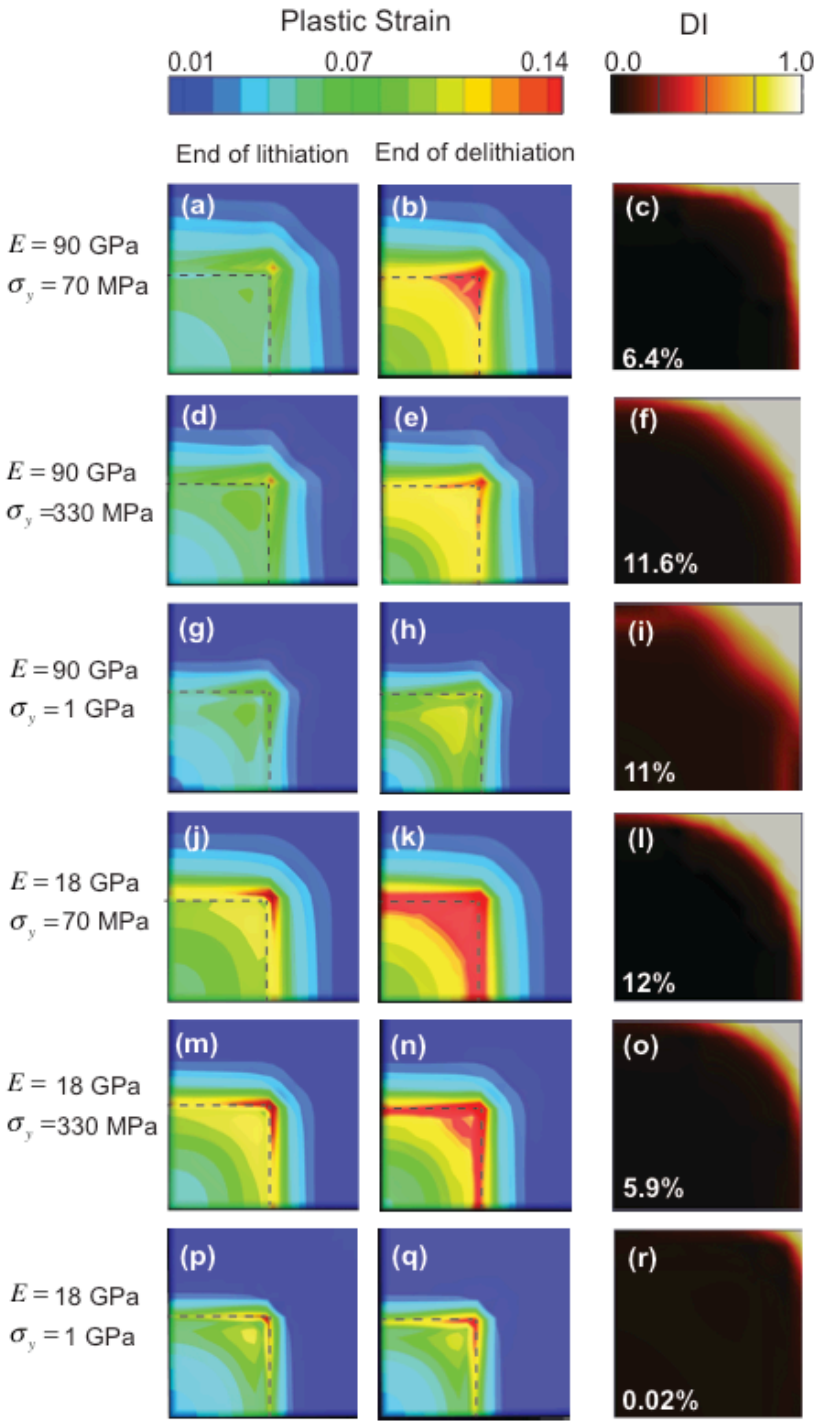

Figure 16. Contour plot of plastic deformation at the top surface of elasto-plastic current collector at the end of lithiation (Column 1) and the end of delithiation (Column 2). Dashed lines on the current collector top surface indicate the reference position of the island. The delamination index for corresponding Si islandecurrent collector interface is shown in Column 3. Percentage of delaminated area is also indicated.

5.4 CONCLUSION

The modeling framework presented in **Chapter 4.0** is utilized to understand the effect of the mechanical properties of the current collector on the interfacial delamination of silicon thin film based anodes. The model parameters are calibrated and validated against the voltage-capacity results obtained from half-cell experiments conducted on anodes of similar configuration. Our model predictions are in excellent agreement with the experimental results except at the start of the lithiation. This can be attributed to the fact that the presence of SEI layer on the thin film and the expected side reactions known to occur during lithiation are not considered. Once calibrated, the model can be used for voltage-capacity simulation at different charge rates and to estimate the maximum reversible charge capacity available. Often, experimentalists vary the voltage window in which the anode half cell is cycled for various reasons, in particular, to reduce the volumetric expansion, etc. The capacity obtained at various cut off potentials can also be estimated by this model.

The modeling framework has been next utilized to predict the crack propagation at the interface between *a*-Si thin film and current collector. The simulations reveal that the elastic modulus as well as extent of inelastic deformation of the current collector are important design parameters that influence the mechanical stability of the anode configuration. If a material with higher stiffness has to be chosen, it is better to consider the candidates that can undergo plastic deformation. However, they will exhibit some extent of delamination that may eventually extend through the entire interface in the course of further electrochemical cycling. An elastic substrate with low elastic modulus is the best design option to safe guard against interfacial delamination. Recent experiments with soft elastic current collectors such as graphite[21] and polymers[16] have shown excellent electrochemical cycling performance. While not mentioned explicitly in these

reports, our analysis suggests that the mechanical stability stemmed from the choice of substrate materials properties itself. It is therefore envisaged that these computational mechanics based models will help the experimentalists design improved silicon based anode systems.

6.0 MODELING OF LITHIUM SEGREGATION INDUCED DELAMINATION OF AMORPHOUS SILICON THIN FILM ANODE IN LITHIUM-ION BATTERIES

6.1 INTRODUCTION

Effect of the current collector material properties (elastic modulus and yield strength) on the *a*-Si - current collector interface has been demonstrated in detail in the pervious chapter (**Chapter 5.0**). The material of choice for current collector for *a*-Si thin film electrodes is copper, which can exhibit considerable plastic flow during electrochemical cycling[12]. During prolonged electrochemical cycling, this inelastic deformation of copper is expected to blunt the Si-Cu interfacial crack tip and may result in its eventually arrest. Failure mechanisms ahead of the crack tip can no longer be activated, as the stress levels would be sufficiently low. However, experimental observation of complete delamination of the Si thin film from the metallic current collector in LIB points to the presence of additional embrittling mechanisms at the interface.

One such mechanism can be segregation induced embrittlement that weakens the interface irreversibly on a cycle by cycle manner. Presence of small amounts of segregants and impurities may have a major effect on the interfacial adhesion[12], and can embrittle the interface sufficiently to cause this type of failure. Assuming that elastic distortion energy due to the presence of lithium atom at the interface is small, elastic distortion energy arising from the intercalation of lithium in silicon can be relieved almost entirely by segregating to the interface.

Thus there will be an energetic preference for the lithium to segregate to the interfacial region[90]. Indeed, evidence of lithium segregation into the interfacial region and the formation of second phase precipitates at the film-current collector interface has been observed experimentally[12, 90]. Selected Area Electron Diffraction (SAED) on post-cycled Si/Cu samples revealed patterns closely matching with Cu_2LiSi phase. Segregation of lithium along with the formation of this interfacial phase led to complete delamination of the thin film from the substrate around 30th cycle.

Several modeling studies have been reported in the literature focusing on lithium diffusion induced stresses in silicon thin film and resultant mechanical degradation of the electrode material[43, 48, 49, 52, 53]. A cohesive model using triangular traction-separation law for crack nucleation in the thin film electrode has been presented and a critical length scale for galvanostatic conditions below that the electrode is flaw tolerant, has been identified in[51]. Computational analysis of through thickness crack pattern formed in thin film electrode during electrochemical cycling has also been studied[14]. Recently, theoretical and experimental study on the size effect of the thin film patterns on interfacial delamination of the silicon film from the current collector has been reported[18, 87, 88]. However, these models typically carry out simulations for a single electrochemical cycle, and do not take into account progressive embrittlement of the interface due to the presence of segregants and other impurities.

Building on the knowledge base gained in **Chapter 5.0** , the thermodymically consistent modeling framework described in **Chapter 4.0** is utilized to simulate the Si thin film anode system over multiple consecutive electrochemical cycles. It is shown that during electrochemical cycling of the thin film island, crack initiates at the corner of the island-current collector interface, as observed in experiments[12]. It is postulated that a process zone precedes the actual

crack tip, and thus can be modeled using the cohesive zone technique. Crack propagation for first few electrochemical cycles is demonstrated. It is shown that as long as the interface properties are not altered, the crack propagation is arrested. Segregation of Li atoms at the thin film–current collector interface is modeled using a modified version of McLean-Langmuir theory. Degradation of interfacial adhesion properties, which leads to complete delamination of the thin film from the metallic current collector, is modeled using a thermodynamic–kinetic analysis of segregation-induced embrittlement (see **Section 4.8**).

In the next section, the boundary value problem and material properties are detailed. Results obtained from simulating the domain for consecutive multiple electrochemical cycles are reported in **Section 6.3**. A brief discussion of the results is presented in **Section 6.4** followed by the conclusions of this study in **Section 6.5**.

6.2 PROBLEM DESCRIPTION

Similar to the previous study in **Chapter 5.0** , a square *a*-Si thin film island on a Cu current collector is considered (see Figure 17). The square Si island is 600 nm wide and 150 nm high. The boundary conditions remain the same as those reported in **Section 5.2**. Young's modulus of *a*-Si in the absence of lithium is taken as $E_0^{Si} = 90$ GPa, while Poisson's ratio is assumed to be constant at $v_0^{Si} = 0.28$[57]. The a-Si thin film is considered to be an elasto-plastic material with yield strength $\sigma_y^{Si} = 1$ GPa and hardening parameter $H^{Si} = 1$ GPa. Material properties for the elasto-plastic copper current collector are given as $E^{Cu} = 90$ GPa and $v^{Cu} = 0.28$, σ_y^{Cu} =330

MPa and $H^{Cu} = 5$ GPa. Other material properties have been taken to be same as that reported in Table 1. Details of the Langmuir-Mclean theory of segregation kinetics and modeling of Li segregation induced embrittlement of the Si-Cu interface are presented previously in **Section 4.8**.

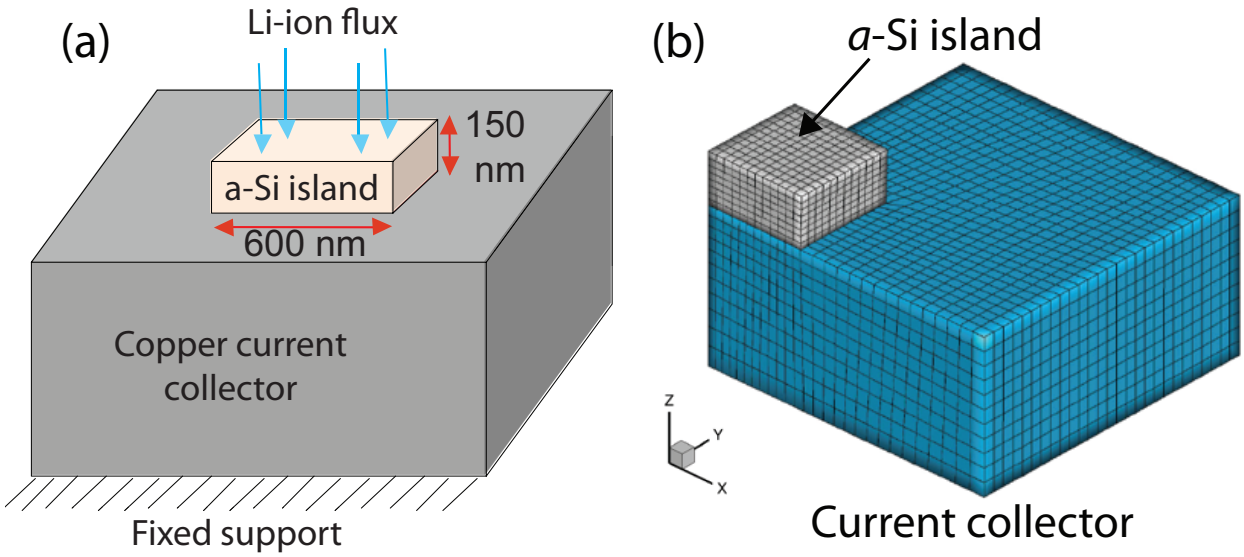

Figure 17. (a) Domain representing a single a-Si island (600 nm width and 150 nm height) on the current collector with Li flux from top (c) Finite element mesh of 1/4th of the a-Si island and current collector domain.

6.3 RESULTS

In this section the results of the simulation study on the interfacial crack propagation between the a-Si thin film anode and the copper current collector over 30 electrochemical cycles is presented. The focus of the results is on the mechanical integrity of the interface between the a-Si thin film and copper current collector and various parameters affecting the growth of delamination. Accordingly, the effect of segregation-induced embrittlement of the interface over multiple electrochemical cycles has been analyzed in detail. Significant attention is given to the

embrittlement kinetics parameters (ductile to brittle transition) of the interface keeping mechanical and electrochemical properties of the a-Si anode and current collector unchanged.

6.3.1 Si-Cu interface delamination over multiple electrochemical cycles: no embrittlement

Prior to the investigation of the effect of embrittlement on the delamination propagation over multiple charge discharge cycles, the crack growth characteristics when no embrittlement mechanisms are present are studied. Such assumption indicates that the interface retains its original failure properties over multiple charge-discharge cycles. The percentage of delaminated interfacial area against the number of electrochemical cycles is calculated for interfacial fracture toughness values ranging from 15 Jm^{-2} to 35 Jm^{-2}. The results are presented in Figure 18. Variation of the extent of delamination at Si-Cu interface with the number of electrochemical cycles for various interfacial fracture toughness magnitudes.. For all these simulations, the critical separation δ_c is kept constant at 4.6 nm while fracture strength σ_c varies according to Equation (4.32) for each case. It can be observed that the interfacial crack propagation shows two distinct regime over the number of cycles for the range of interfacial toughness considered here. In the first regime, the delamination propagates rapidly while in the second regime the percentage delamination shows almost no increase in magnitude indicating the arrest of crack. Number of cycles that separates these regimes depends on the fracture toughness of the interface. It can be as low as five cycles for the case of lowest fracture toughness considered, while the interface with $G_c = 35$ Jm^{-2} does not show a complete arrest of delamination for the range of electrochemical cycles simulated.

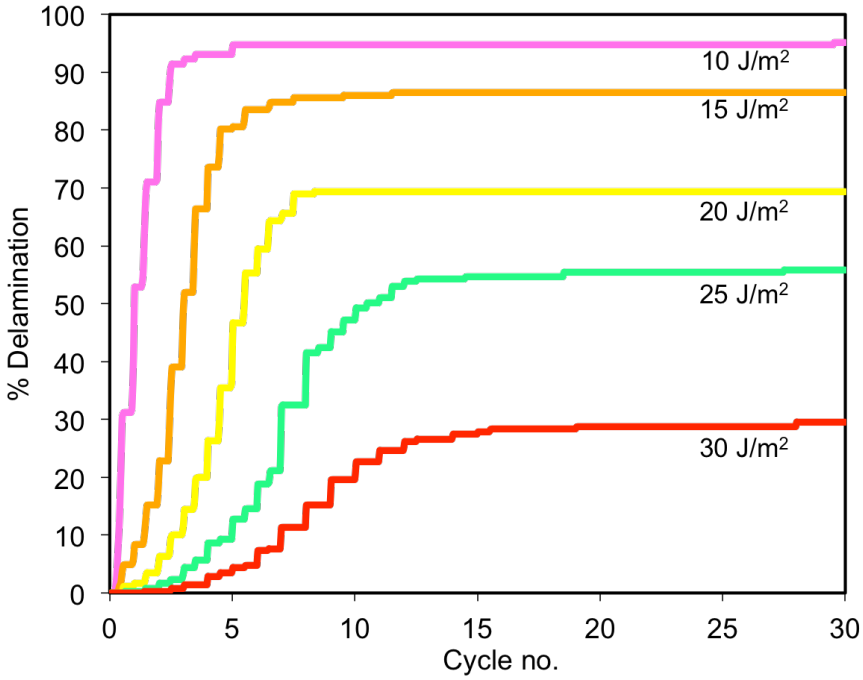

Figure 18. Variation of the extent of delamination at Si-Cu interface with the number of electrochemical cycles for various interfacial fracture toughness magnitudes.

It can be noticed that as the fracture energy is reduced, interfacial delamination is increased considerably compared to the cases with higher fracture energy. Interface with $G_c = 10$ Jm^{-2} attains the maximum delamination of 95% rapidly within first few cycles (<5); however it is arrested completely in subsequent cycles. For the interface with higher fracture energy ($G_c = 35$ Jm^{-2}), the interface continues to delaminate over the entire simulation of 30 cycles albeit at a much slower rate compared to the previous cases. However, the peak delamination reached even after 30 electrochemical cycles is only about 18%, and thus is not expected to delaminate completely even after undergoing further cycling.

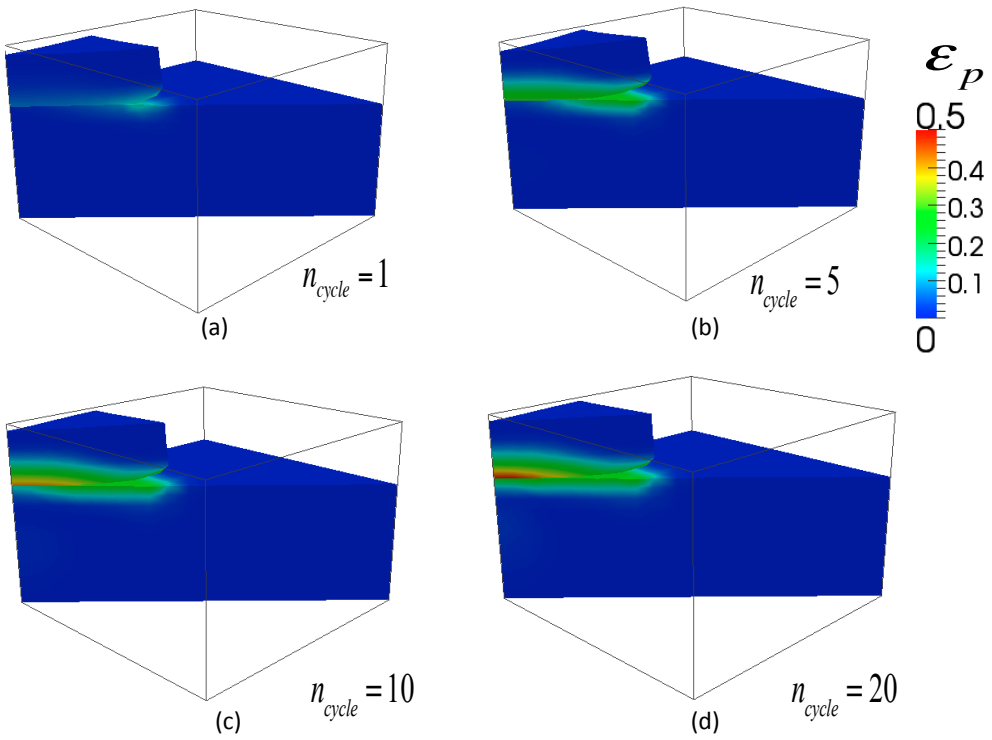

Figure 19. Contours of plastic strain (ε_p) at the interface between the a-Si island and Cu substrate at the end of different electrochemical cycles. For better representation, a cross- sectional view along the diagonal of the computational domain is shown.

To understand crack arrest mechanisms in the a-Si thin film and copper current collector system, plastic deformation in the vicinity of the interface is analyzed at the end of different cycles (Figure 19), while keeping the fracture toughness $G_c = 25$ Jm^{-2}. It should be noted that the plasticity for both the silicon thin film and the copper current collector is considered for the simulations. As the crack propagates diagonally from the corner towards the center of the island, a cross-sectional view of the thin film as well as the substrate along a vertical plane passing diagonally through the simulation domain is shown. The delamination of the interface for corresponding cycles is plotted in Figure 21 (top row). In this figure, the red region (DI=1.0) represents a completely delaminated interface while the blue one denotes the uncracked portion.

It can be seen that after the first cycle, a small delamination zone appears at the corner of the island (Figure 19 **(a)**). A small plastically deformed region is also visible in both the island as well as the substrate in Figure 19 **(a)**. At the completion of 5^{th} cycle, crack propagates quickly towards the center of the thin film island (Figure 21 **(b)**). A well-developed plastic region can be seen around the crack in Figure 19 **(b)**. At the end of 10^{th} cycle, delamination propagates further inside (Figure 21 **(c)**). At this stage, Figure 19 **(c)** shows a wide spread plastic region that has evolved along the entire interface. Note that it is localized along the thickness direction: Its extent scales with the thickness of the thin film. When the cycling reaches to 20^{th} cycle, there is no significant increase in the delamination as seen in (Figure 21 **(d)**). In this cycle, Figure 19 **(d)** shows the extent of plastic zone around the delamination, which is almost similar to the previous one except for a small region ahead of the crack tip that shows an increased plastic strain. This fact indicates that the material around the crack tip is mostly subjected to a stress state that remains around the yield strength from 10^{th} cycle to 20^{th} cycle. These electrochemical cycles only increased the value of the accumulated plastic strain thus keeping the stress at the crack tip well below the fracture strength.

6.3.2 Si-Cu interface delamination over multiple electrochemical cycles: with embrittlement

It has been observed in the previous section that the delamination is arrested after few cycles, contrary to the experimental observations. It is envisaged that the segregation of lithium atom into the interface between the thin film and copper current collector can drive the crack further leading to the complete failure of the film. Therefore, the effect of embrittlement is investigated by changing the embrittlement factor w while keeping all other parameters constant. w=1

indicates ideal conditions for segregation, while w=0 indicates no segregation induced embrittlement (see **Section 4.8** for details). Figure 20 shows the variation of percentage of delamination against the number of electrochemical cycles for different values of w. In this study, the interfacial fracture energy is kept constant at $G_c = 25$ Jm^{-2} with maximum interface strength $\sigma_c = 2$ GPa. The interface with no embrittlement is indicated by $w = 0$. The higher values of embrittlement factor indicated higher rates of degradation for the interface due to lithium segregation. It can be seen that as the embrittlement factor increases, the amount of delamination increases rapidly for first few cycles. Furthermore, delamination continues to grow in the second regime of crack growth where interfacial crack with no segregation exhibits almost complete arrest. Moreover, with an embrittlement factor w=0.4, the interface delaminates completely at ~24th cycle. It should be noted that the experiments performed on a similar anode system exhibited a rapid capacity fade after 29th cycle[12]. A complete delamination of the thin film from the copper substrate after this cycle is observed.

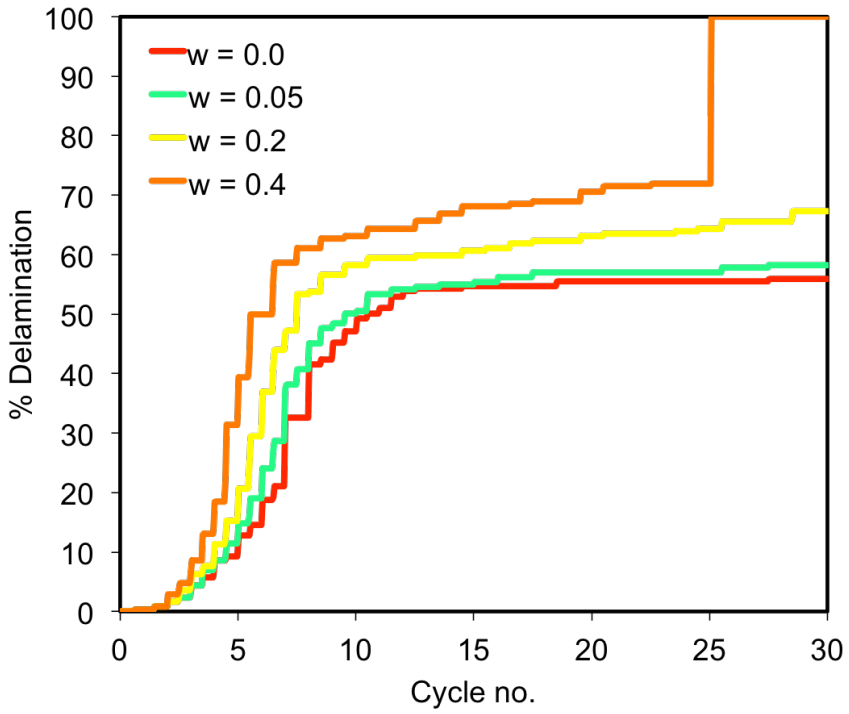

Figure 20. Variation of the delamination of a-Si thin film and Cu current collector interface with the number of electrochemical cycles for various degrees of interface embrittlement.

To describe crack propagation more elaborately, the delamination at different number of electrochemical cycles is compared in Figure 21 for w=0.4 and for w=0 (no embrittlement scenario). The red region represents a delaminated zone of the interface while blue zone denotes the uncracked portion. It can be found that the interface with embrittlement offers considerably higher amount of delamination (Figure 21 **(f)**) even after 5th cycle compared to the interface with no embrittlement (Figure 21 **(b)**). At 10th cycle, interface with embrittlement achieves more delamination (Figure 21 **(g)**) compared to no embrittlement case (Figure 21 **(c)**). As the charge discharge cycle proceeds further, the embrittlement imparts continuing delamination of the interface (Figure 21 **(h)**). However, interface with no embrittlement prevents its further delamination (Figure 21 **(d)**).

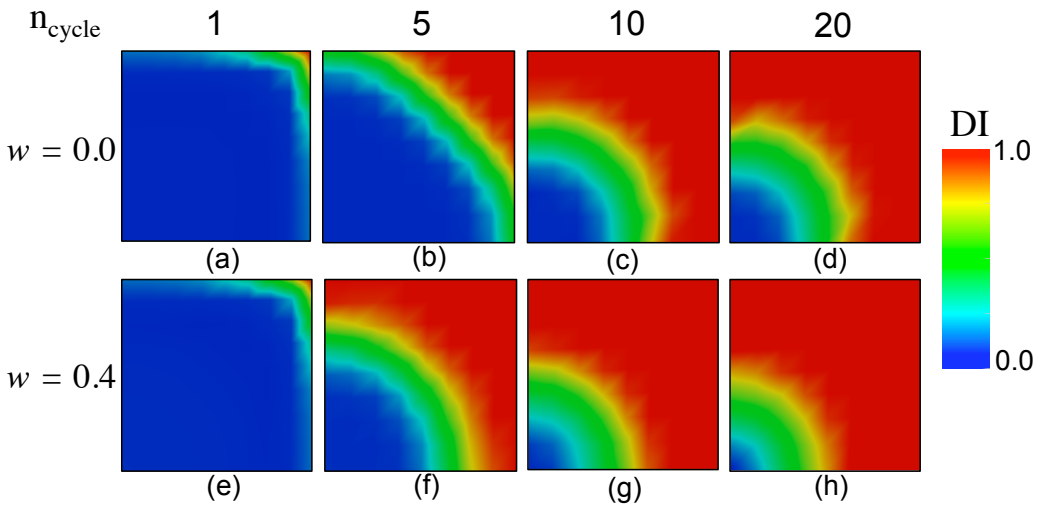

Figure 21. Contour plots for the delamination index (DI) with DI = 1 representing completely delaminated region and DI = 0 indicating uncracked zone for w = 0 (no interface embrittlement), top row, and w = 0.4, bottom row, at the end of different electrochemical cycles n_{cycle}.

6.4 DISCUSSION

The simulations reported in this chapter are performed on a model system closely mimicking the geometry and electro-chemo-mechanical boundary conditions of an actual LIB half-cell. For simulations reported in this chapter, the presence of plasticity in the film as well as in the substrate is considered. It is observed that if both the substrate and the film are considered elastic, significant delamination (even complete delamination) may occur only after the first electrochemical cycle. On the contrary, plastic dissipation in the copper substrate and silicon film retards the interfacial delamination to a great extent and may arrest it after a few cycles, see Figure 18. However, experiments on this system typically reveal a complete delamination after multiple electrochemical cycles[12]. To account for this observation, elasto-plastic material

response in the film and the substrate, and an embrittling interface between them possibly due to lithium segregation is considered.

It is found that without interface embrittlement, the crack propagation is completely arrested for a wide range of interfacial fracture energies when the interface is moderately strong with fracture strength of 2 GPa. The delamination of the silicon thin film from the copper substrate is simulated for a wide range of interfacial strength values keeping the toughness constant at 25 Jm^{-2}. The results show that the crack arrest is inevitable for all the cases with an interfacial strength in excess of 1 GPa. As the elastic distortion energy associated with the intercalation of lithium in silicon is quite high, it will have a propensity to segregate towards the surface of the thin film. This suggests that the segregation of lithium in the interfacial region is responsible for the gradual embrittlement of the interface. Such embrittlement is modeled here through a reduction in the interfacial fracture energy, which depends on the extent of segregation of Li atoms at the interface over multiple cycles. The present analysis shows that embrittlement plays a crucial role in the propagation of delamination in early as well as later stages of the crack propagation. As the segregation induced embrittlement takes place, the crack growth resistance reduces progressively. Crack driving force arising from the deformation of a-Si thin film and Cu substrate eventually surpasses the crack growth resistance leading to further propagation of delamination. Reduction of the crack growth resistance depends critically on the amount of lithium that can reach the interface, which in turn depends on a number of factors such as thickness of the film, applied charge rate, and presence of other species at the interface.

6.5 CONCLUSIONS

A novel multi-physics modeling framework has been utilized to understand the mechanisms responsible for delamination of a-Si thin film and copper current collector over multiple cycles. Furthermore, Langmuir-Mclean theory for segregation kinetics has been incorporated to model embrittlement induced degradation of the interface. It has been observed that with no embrittlement of the interface, crack propagates rapidly for first few cycles but is eventually arrested. If segregation induced embrittlement mechanisms are taken into account, extent of delamination is enhanced. For certain parametric combinations, complete delamination as observed in the experiments, can be achieved. Thus, the present computational framework provides a mechanistic understanding of the effect of interfacial properties and the Li segregation induced embrittlement on the growth of interfacial delamination of the a-Si thin film based LIB anode subjected to multiple electrochemical cycling.

7.0 EFFECT OF INSERTION OF AN ELASTIC BUFFER LAYER ON INTERFACIAL STABILITY OF AMORPHOUS-SILICON

7.1 INTRODUCTION

For the Si thin film based electrode structures, delamination of the electrochemically active thin film from the substrate is a major concern. Three primary approaches to delay the onset and propagation of delamination are discussed in the literature. A design philosophy pursued recently is the control of the size of the patterns to a flaw tolerant dimension. As thin films are prone to vertical cracking, a typical approach is to create patterned anodes with width less than the average vertical crack spacing referred to as the critical size for a given film thickness [18, 87, 91, 92]. In another class of approaches, stability is sought through the surface modification of the current collector surface and the properties of the Si-current collector interface. Nguyen and Song[24] attempted to stabilize the Si-Cu interface by anodic etching of the current collector surface to promote the interfacial contact area at Si-Cu interface. Cho et al. [93] has suggested an improvement of the electrochemical cycling performance of the patterned electrodes by fabricating them on a rough substrate rather than on a smooth surface. Chen et al. [23] showed that annealing the Si thin film anode at high temperature enhances the anode cycling stability by improving the Si-Cu interface adhesion.

A third promising approach that has not gained much attention is the optimal design of the electrochemically inactive substrate material and configuration. Analytical study by Song et al. [94] concluded that for cylindrical Li ion batteries, the current collector with small thickness and low elastic modulus minimizes stresses in the active material layer. Numerical studies by Zhang et al. [95] concluded that a soft and flexible current collector material would be ideal for the electrode. Yu et al. [16] showed that the capacity retention of the patterned thin film is greatly enhanced by incorporating an elastomeric layer as a part of the current collector. Work by Zhang et al. [96] demonstrated that including a graphene buffer layer between Cu current collector and *a*-Si thin film benefits the capacity retention of the electrode. In another earlier work, Datta et al. [21] experimentally demonstrated that the presence of a 50 nm thick carbon layer sandwiched between the active silicon thin film and copper current collector improves the cycling performance of the thin film anode. Tong et al.[97] also studied multilayer Si/C thin films deposited on Cu current collector and concluded that the carbon layer improves the anode structural stability by helping accommodate the volume expansion of Si. Choi et al.[98] used a current collector made by coating porous polyolefin polymer membrane with a thin layer of copper. Presence of the polymer membrane provides flexibility to the current collector, which helps the electrode performance by allowing it to freely expand and contract during electrode cycling.

A common aspect of all these[16, 21, 94-98] exhaustive reports is the introduction of a low stiffness elastic layer along with the usual silicon thin film and metallic current collector. Indeed, results in **Chapter 5.0** show that an elastic substrate with low modulus can retard the interfacial delamination significantly. However, the mechanisms operative in the presence of a soft elastic layer that give rise to improved cycling performance are not well understood. Therefore, the aim

of the present chapter is to provide a mechanistic understanding of the role of inserted elastic layer on the delamination behavior of a patterned *a*-Si thin film Li-ion anode.

The thermodynamically consistent modeling framework described in **Chapter 4.0** is employed to calculate energetic contributions of various mechanical events occurring at the anode during lithiation. The study is restricted to a single square shaped pattern made of silicon thin film and a thin elastic layer residing atop a copper current collector for numerical tractability, see Figure 22. However, the main conclusion that the modulus mismatch between the silicon thin film and the sandwiched elastic layer is essentially the key design parameter for the improvement of mechanical stability is general enough to be applicable to a broad spectrum of micro patterned layered anode architectures.

This chapter is organized as follows: In **Section 7.2**, energy balance of the lithium ion half-cell is detailed. The description of the boundary value problem is described in **Section 7.3**. Results of the study are presented in **Section 7.4**, followed by conclusions in **Section 0**.

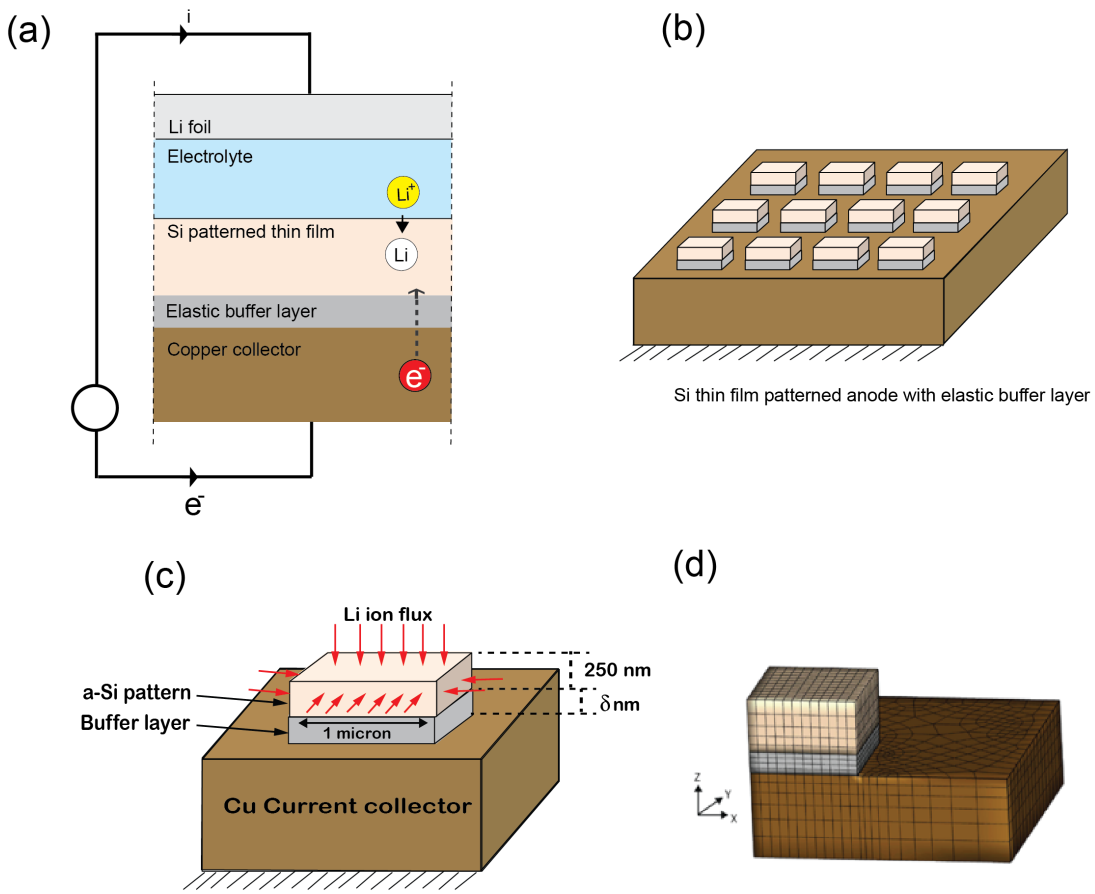

Figure 22. (a) Schematics of Si patterned thin film anode with elastic buffer layer half-cell (b) Schematic of patterned anode configuration with a-Si pattern, intermediate buffer layer and current collector. (c) Mathematical domain representing a single pattern with intermediate buffer layer attached to a current collector. Li flux is applied from all the surfaces exposed to electrolyte. (d) Finite element mesh of 1/4th of the mathematical domain.

7.2 ENERGY BALANCE OF THE LI ION HALF-CELL DISCHARGE PROCESS

Schematic of the Li ion half-cell discharge voltage curve under galvanostatic conditions is shown in Figure 22 **(a)**. The anode is cycled between the voltage limits of V_{max} and V_{min} at a

charge/discharge current of i, with the total discharge time t. During the galvanostatic half-cell discharge, maximum output energy $\Psi_{out\,max}$ is obtained when the cell discharge is carried out at an infinitesimally small current. In this case, $\Psi_{out\,max}$ can be calculated as the product of area under the open circuit potential (U_{ocp}) - time curve and the discharge current i.

$$\Psi_{out\,max} = i\int_0^t U_{ocp}\, dt \tag{7.1}$$

However, due to the energy loss associated with overpotential (η_s), the energy derived from the half-cell (Ψ_{out}) is less than ($\Psi_{out\,max}$) and is represented by the product of the discharge current i and the area under the output voltage ($V(t)$) - time curve. Thus,

$$\Psi_{out\,max} = \Psi_{out} + \Psi_{\eta_s} \tag{7.2}$$

and,

$$\Psi_{out} = i\int_0^t V(t)\, dt \tag{7.3}$$

Part of Ψ_{η_s} is lost in terms of heat (Ψ_q) and consists of the reaction overpotential, concentration overpotential and the resistance overpotential. The rest of this lost energy is contributed by the overpotential related to the transport of Li inside the electrode material ($\Psi_{Li\,transport}$) and the energy required for causing the mechanical changes Ψ_{mech} in the electrode system. Hence,

$$\Psi_{\eta_s} = \Psi_q + \Psi_{Li\,transport} + \Psi_{mech} \tag{7.4}$$

The mechanical contribution Ψ_{mech} can be further partitioned into three different categories: total elastic strain energy ($\Psi_{elastic}$) stored in the system, total plastic dissipation ($\Psi_{plastic}$) associated

with the plastic flow of the material, and total dissipated interfacial energy ($\Psi_{interface}$) which results from the delamination.

The rate of elastic strain energy accumulated at each layer is evaluated as

$$\dot{\Psi}_{elastic} = \int_{\Omega_i} \boldsymbol{S}^i : \dot{\boldsymbol{E}}^i \, d\Omega \quad with \;\; i \in [Si, buffer, Cu] \tag{7.5}$$

Therefore, the total elastic energy of the anode at a given time t can be estimated as

$$\Psi_{elastic} = \int_0^t \dot{\Psi}^{Si}_{elastic} \, dt + \int_0^t \dot{\Psi}^{buffer}_{elastic} \, dt + \int_0^t \dot{\Psi}^{Cu}_{elastic} \, dt \tag{7.6}$$

The rate of plastic dissipation in Si thin film and Cu substrate is calculated as

$$\dot{\Psi}_{elastic} = \int_{\Omega_i} \boldsymbol{S}^i : \dot{\boldsymbol{E}}^i \, d\Omega \quad with \;\; i \in [Si, buffer, Cu] \tag{7.7}$$

Therefore, total plastic energy at given time t is calculated as

$$\Psi_{plastic} = \int_0^t \dot{\Psi}^{Si}_{plastic} \, dt + \int_0^t \dot{\Psi}^{Cu}_{plastic} \, dt \tag{7.8}$$

As the buffer layer is elastic and does not exhibit any plasticity, the energy expended in propagation of delamination in Si/buffer and buffer/Cu interface is evaluated as

$$\dot{\Psi}^{(i)}_{interface} = \int_{\Gamma_i} \boldsymbol{t}^{(i)} \cdot \dot{\boldsymbol{\delta}}^{(i)} \, d\Gamma \qquad i \in [Si / buffer, buffer / Cu] \tag{7.9}$$

Therefore, the total energy dissipation due to delamination propagation at any given time t is given as

$$\Psi_{interface} = \int_0^t \dot{\Psi}^{Si/buffer}_{interface} \, dt + \int_0^t \dot{\Psi}^{buffer/Cu}_{interface} \, dt \tag{7.10}$$

Finally, the total mechanical energy is derived

$$\Psi_{mech} = \Psi_{elastic} + \Psi_{plastic} + \Psi_{interface} \tag{7.11}$$

When an anode system is lithiated, it begins to deform mechanically owing to the transport of the lithium ions into the anode leading to alloying with Si as the Li^+ combine with the electrons transported through the Si, and starts storing the mechanical part of the free energy by elastic deformation and plastic dissipation. As Ψ_{mech} increases further, a portion of the stored mechanical energy is released through the nucleation and propagation of delamination at the interface.

The previously presented numerical framework (**Chapter 4.0**) is used to precisely evaluate these quantities and study the effect of the different parameters on Ψ_{mech} evolution in the anode configuration detailed in this manuscript.

7.3 PROBLEM DESCRIPTION

To study the effect of a thin buffer layer present between the patterned Si thin film and current collector on the mechanical stability of a patterned thin film based anode, a domain as shown schematically in Figure 22 (b) is considered. The square shaped *a*-Si patterns are each 250 nm thick and 1 micron wide. In the simulations, the gap between the adjacent patterns is assumed to be sufficient such that the patterns do not interfere with each other in the fully lithiated state. Accordingly a model domain is isolated with only one pattern, as shown in Figure 22 (c), for this study. Considering the advantage of pattern configuration symmetry and only $1/4^{th}$ of the domain for the simulation purpose (Figure 22 (d)) is taken. The intermediate buffer has the same width as the pattern. The thickness of the buffer layer (h_b) is kept constant at 100 nm. Thickness of the

current collector is assumed to be three times that of the pattern to avoid any influence of the boundary on the simulation results. The domain has two interfaces, Si/buffer interface and the buffer/current collector interface. Both of these interfaces are prone to delaminate during the lithiation process. It is assume that the anode is cycled under galvanostatic conditions and hence consider a constant flux of lithium atom through the surfaces of the active material that are exposed to the electrolyte. It should be noted that some possible buffer layer materials such as carbon, undergo lithium intercalation. Consideration of contribution of buffer layer to the Li anode capacity would effectively reduce the contribution of Si film pattern to the anode capacity and hence the associated volumetric expansion. The aim of this manuscript is to understand the effect of mechanical properties of elastic buffer layer on the mechanical stability of the patterned a-Si anode. Hence, in order to consider maximum volumetric expansion associated with the a-Si film, it is further assume that the buffer layer and the current collector have no lithium diffusion and hence, no associated diffusion induced volumetric expansion.

In the galvanostatic lithiation of the anode, the anode capacity is taken to be 3000 mAh/g. All the studies performed in this article are conducted at C/2.5 charge rate. The anode discharge simulation is performed between the voltage window of 1.2 to 0.02 V, similar to experiments[12, 19]. The rate constants for lithiation and delithiation process are listed in Table 2. The diffusivity of Li inside the bulk *a*-Si is considered to be 10^{-16} m^2/s while the expansion coefficient is assumed to be 4.5×10^{-6} m^3/mol. Compressible Neo-Hookean constitutive model has been used for all the materials to simulate large deformation mechanical response. The buffer layer is taken to be elastic for all the simulations, while elasto-plastic behavior of the copper current collector is assumed throughout. Lithiation induced softening of amorphous Si is taken into account in the

model using the relationship $E_0^{Si}(Li_{fraction}) = E_0^{Si} - m \times Li_{fraction}$. The corresponding material properties and the interface properties considered for the simulations are compiled in Table 2.

Using the computational framework described in chapter 4.0 , the effect of buffer layer on the stability of Si patterned Si anode configuration is investigated. As it is known, complete delamination of the Si pattern to the current collector and will thus lead to complete loss of electrical connectivity to the Si pattern and render the anode non-functional for electrochemical cycling. Also, upon partial delamination, the delaminated area will get exposed to the electrolyte leading to growth of SEI layer causing additional capacity loss. Hence, to characterize the mechanical integrity of the thin film pattern, the delamination of the Si pattern from the rest of the anode configuration is tracked. A systematic parametric study of the effect of the elastic buffer layer stiffness was thus undertaken. Furthermore, to understand the effect of adhesion between different anode components, the interfacial fracture strength and fracture toughness is varied to observe its effect on Si pattern delamination. The results of this study are presented below.

Table 2. Material Properties

Young's modulus of *a*-Si (E_0^{Si})	$90\,\text{GPa}$ [57]
Rate of change of elastic modulus of *a*-Si with Li fraction (m)	$71.25\,\text{GPa}/\text{Li}_{fraction}$ [57]
Poisson's ratio of *a*-Si (ν_0^{Si})	0.28
Yield strength of *a*-Si (σ_y^{Si})	1GPa
Young's modulus of buffer layer (E_b)	$0.1\,\text{to}\,200$ GPa
Poisson's ratio of the buffer (ν_0^{Buffer})	0.28
Young's modulus of Cu (E_0^{Cu})	$100\,\text{GPa}$
Poisson's ratio of Cu (ν_0^{Cu})	0.34
Yield strength of Cu (σ_y^{Cu})	$300\,\text{MPa}$
Hardening modulus of Si (H^{Si})	1GPa
Hardening modulus of Cu (H^{Cu})	$5\,\text{GPa}$
interface fracture toughness (G_c)	$15\,\text{J/m}^2$ [12]
Interface fracture strength (σ)	2 GPa
k (lithiation)	$1.55\times10^{-13}\,(\text{ms}^{-1})(\text{mol}\,\text{m}^{-3})^{-0.5}$ [99]
k (delithiation)	$60\times10^{-13}\,(\text{ms}^{-1})(\text{mol}\,\text{m}^{-3})^{-0.5}$ [99]

7.4 RESULTS

The effect of buffer layer elastic modulus and interface properties (fracture strength and toughness) of Si-buffer and buffer-Cu interface are studied systematically. In the following the results of the simulations are presented and discussed in detail.

7.4.1 Effect of buffer layer stiffness on the *a*-Si pattern anode stability

First, the effect of insertion of an elastic buffer layer on the stability of the patterned *a*-Si anode is demonstrated. Comparison of the mechanical integrity of the patterned *a*-Si thin film directly deposited on a Cu current collector is done against the mechanical integrity of the anode configuration which has an elastic buffer inserted between the patterned *a*-Si thin film and the Cu current collector (Figure 22 (b)). The buffer layer thickness is considered to be 100 nm, while varying the buffer layer elastic modulus (E_b) from 0.1 to 200 GPa. The Interfacial fracture strength of the Si-buffer and buffer-Cu interfaces is taken to be $\sigma_c = 2$ GPa and the fracture toughness is kept at $G_c = 15$ J/m^2, unless otherwise specified.

Figure 23 shows the evolution of delamination of the Si thin film pattern during the half-cell discharge (lithiation) process. On the x-axis, soc (state of charge) of 0 corresponds to the start of lithiation and $soc = 1$ corresponds to end of the lithiation step. It should be noted that soc of the anode is linearly related to the time in the half-cell galvanostatic discharge process. The percentage of Si thin film delamination, shown on the y-axis is calculated with respect to the referential interfacial area. Thus, a percentage of zero signifies no delamination and a percentage value of 100 represents complete delamination. In Figure 23, higher slope of the curve signifies a

higher degree of delamination, and thus the propensity for increased loss in capacity of the anode system. In the absence of the elastic buffer layer, 6.2% delamination of patterned Si film from the Cu current collector is observed. On the other hand, with the elastic buffer layer present, the delamination of the patterned *a*-Si varies depending on the elastic modulus of the buffer layer. The amount of delamination increases as the buffer elastic modulus is increased beyond 20 GPa and reaches about 7.6 % for a buffer stiffness of 200 GPa. It should be noted, that the % delamination reported in Figure 23 are all only after the 1st lithiation. Experimental[12] and simulation[100, 101] studies in the literature have reported that the interfacial delamination progressively increases over the course of electrochemical cycling. Thus, even though the amount of delamination reported in Figure 23 is a few percent, it is expected to increase during prolonged cycling. Thus, for the longevity of the anode cycling performance, it is of paramount importance to completely prevent the onset of interfacial delamination.

To understand the influence of the stiffness of the buffer layer placed in between the active Si layer and Cu current collector, Figure 23 is portioned into two zones. The green zone is below the delamination curve for no buffer case (red solid line), which essentially represents the conditions where the magnitude of delamination is lower than the base case with no buffer layer. On the other hand, the pink zone above the no buffer condition curve signifies the conditions with the amount of delamination higher than that for the no buffer situation. Curves falling in zone 1 thus show delamination higher than that observed for Si pattern directly deposited on Cu current collector. Observation of the plot indicates that when the buffer elastic modulus is higher than the elastic modulus of the Cu current collector (E_{Cu}=100 GPa), insertion of the elastic buffer layer does not really aid in improving the mechanical integrity of the patterned Si anode. The curves falling in zone 2 are of interest, as they show reduction in amount of Si pattern

delamination upon insertion of the buffer layer. When the buffer elastic modulus is less than 20 GPa, the Si thin film pattern shows no delamination at all, indicating that the anode maintains its mechanical integrity.

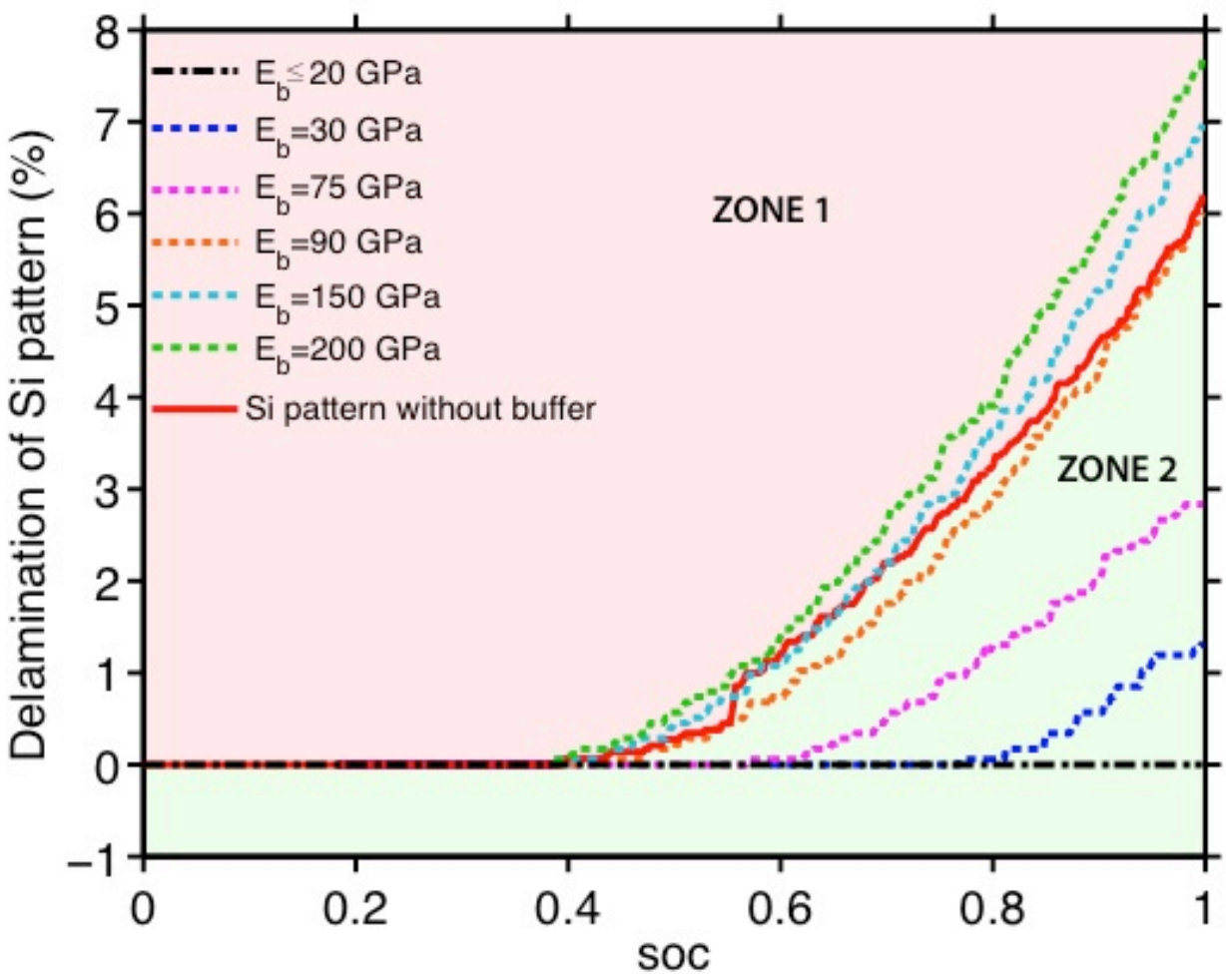

Figure 23. Evolution of delamination of Si pattern during lithiation of the Si pattern with elastic buffer layer of different stiffness of 100 nm thickness and without the presence of buffer layer (σ =2 GPa, G_c= 15 J/m^2). The curve showing the evolution of delamination of the Si thin film on Cu current collector (solid red line) divides the plot into two zones.

In Figure 24 (a)-(c), the deformation contours for the three different conditions at the end of lithiation are shown. The conditions shown are: patterned Si on Cu current collector, patterned Si with an elastic buffer layer of 0.1 GPa stiffness and patterned Si with an elastic buffer layer of 200 GPa stiffness. The corresponding delamination state of the patterned Si / buffer or patterned Si/ Cu interface is shown in Figure 24 (d)-(e) where the red color indicates delamination and blue color indicates the intact interface. Figure 24 (a) and (d) show that at the end of lithiation, the patterned Si partially delaminates from the current collector at the corner of the Si/Cu interface. Details of the mechanism of the delamination of Si thin film on Cu current collector are discussed in our previous work [99, 101]. The observed delamination of the patterned Si on copper is about 6.2 % of the interfacial area. Delamination of 7.6 % is observed when an elastic buffer of 200 GPa stiffness is present below the Si pattern (Figure 24 (c) and (f)). In both the cases, Si pattern seems to have delaminated at the corner of Si/buffer interface. However, when the stiffness of elastic buffer is 0.1 GPa, the elastic buffer layer seems to have deformed significantly (Figure 24 (b)) as compared to the buffer layer with 200 GPa stiffness and the patterned Si /buffer interface is intact (Figure 24 (e)). Thus results in Figure 23 and Figure 24 clearly indicate that the presence of an elastic buffer layer can alter the mechanical stability of the thin film pattern during electrochemical cycling depending on the mechanical properties of the buffer layer.

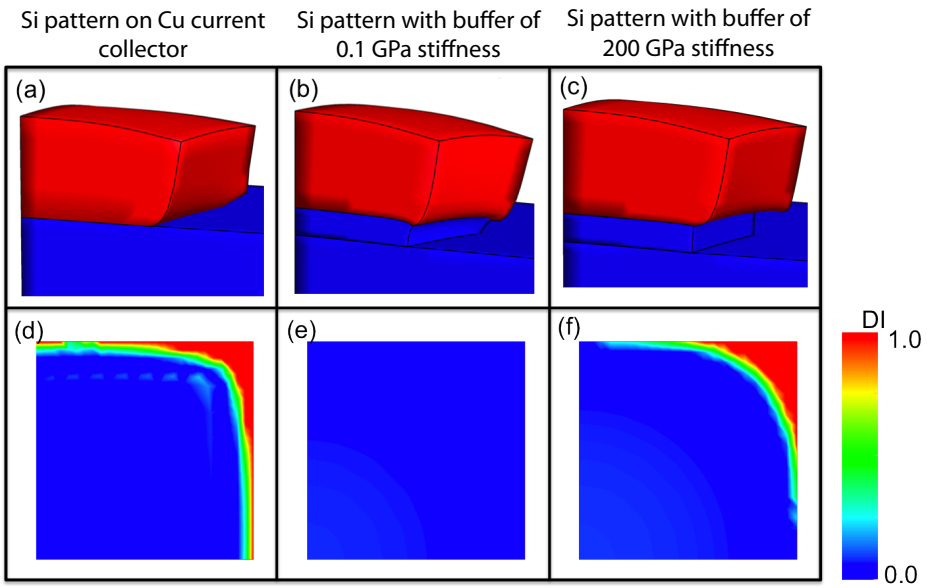

Figure 24. Deformation contour of Si pattern film at end of lithiaion (a) on a Cu current collector (E_{Cu} = 100 GPa), (b) with elastic buffer layer of 0.1 GPa and (c) 200 GPa stiffness. Delamination of Si pattern corresponding to these cases is represented by Delamination Index (DI) in (d), (e) and (f), respectively (σ =2 GPa, G_c= 15 J/m^2).

(a)

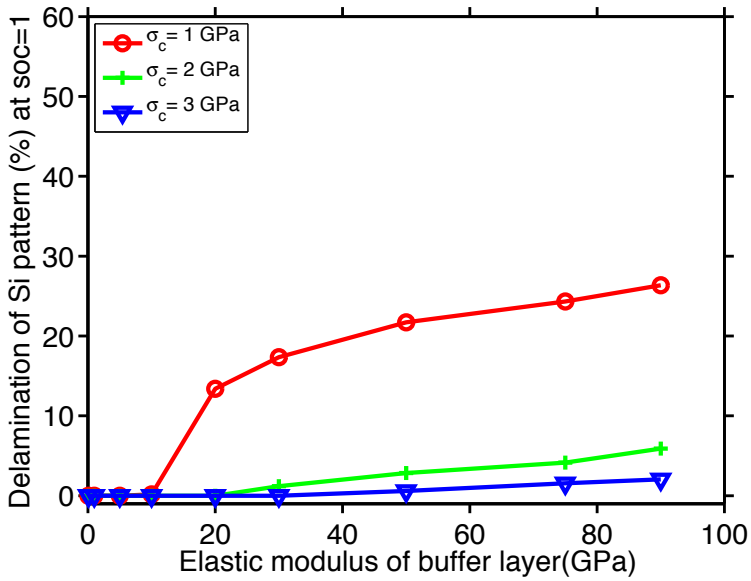

(b)

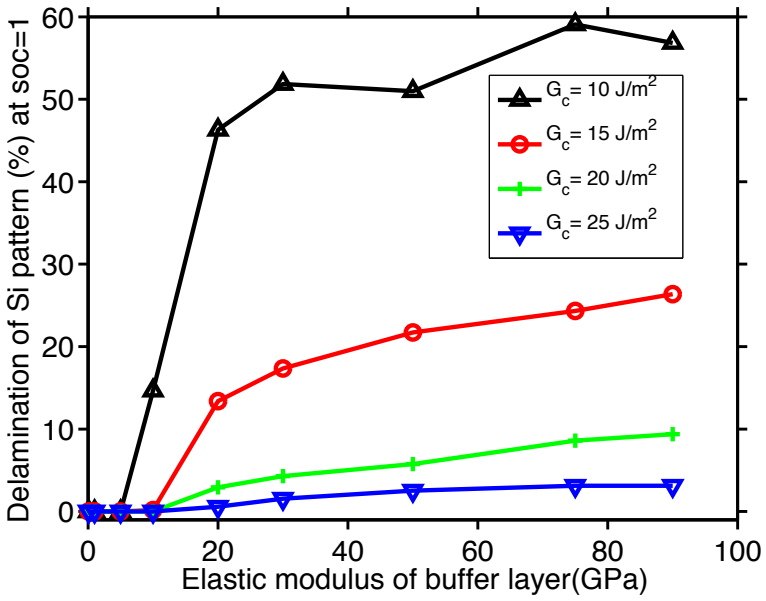

Figure 25. (a) Amount of Si pattern delamination at the end of lithiation with different interface fracture strengths and G_c= 15 J/m^2. (b) Amount of Si pattern delamination at the end of lithiation with different interface fracture toughness and σ_c =1 GPa.

7.4.2 Effect of interfacial adhesion properties on the *a*-Si patterned anode stability

To understand the effect of the interfacial fracture strength on the mechanical integrity of the patterned Si anode configuration, the fracture strength (σ_c) of the Si-buffer and the buffer-Cu interface is varied from 1 GPa to 3 GPa in increments of 1 GPa. The fracture toughness (G_c) of the interface was kept constant at 15 J/m^2. As observed in Section 7.4.1, inclusion of an elastic buffer with modulus greater than the elastic modulus of Cu (100 GPa) does not reduce the patterned Si delamination (see zone 1 in Figure 23). Thus, the buffer elastic modulus was varied from 0.1 to 90 GPa.

The delamination of the patterned Si from the buffer layer for different fracture strengths at the end of lithiation half cycle is shown in **Figure 25** (a). It can be observed that increasing the fracture strength from 1 to 3 GPa reduces the amount of the delamination of the patterned Si irrespective of the buffer elastic modulus. When the fracture strength is 1 GPa, the critical buffer elastic modulus below which the delamination of the patterned Si pattern is suppressed is 10 GPa. In case of 2 GPa and 3 GPa fracture strength, the critical elastic modulus is 20 and 30 GPa, respectively. Thus, these results clearly indicate that increasing the interfacial fracture strength helps to enhance the mechanical integrity of the patterned Si anode.

In order to investigate the effect of interfacial fracture toughness on the mechanical integrity of the patterned Si anode configuration during electrochemical cycling, the fracture toughness of the Si-buffer and buffer-Cu interface is varied from 10 to 25 J/m^2. The fracture strength of the interface was kept constant at 1 GPa. **Figure 25** (b) reports the amount of interfacial delamination of the patterned Si at the end of lithiation half-cycle for different values of fracture toughness and elastic moduli of the buffer.

As shown, increasing the interfacial fracture toughness decreases the amount of delamination of the patterned Si pattern, thus improving the mechanical integrity of the patterned Si anode during electrochemical cycling. In the case of E_b =90 GPa, the delamination is reduced from 57 to 3% as the fracture toughness is increased from 10 to 25 J/m^2. The critical buffer elastic modulus below which the delamination of the patterned Si is avoided is 5 GPa when fracture toughness is 10 J/m^2. However, for the fracture toughness of 15-25 J/m^2, the critical buffer elastic modulus is increased to 10 GPa.

7.5 DISCUSSION AND CONCLUSION

The simulations performed in this chapter are aimed to study the effect of presence of an elastic buffer layer on the mechanical stability of the patterned *a*-Si thin film closely mimicking the electro-chemo-mechanical boundary conditions prevalent in an actual experimental Li ion half-cell. In this chapter, a thin elastic buffer layer is introduced between the metallic current collector and the patterned *a*-Si thin film to study its effect on the stability of the patterned *a*-Si anode configuration.

Electrochemical cycling of the active material requires the presence of other components in the anode configuration for different reasons. For example, a Cu current collector is needed in the a-Si thin film anode for electron conduction, while the PVDF binder and carbon black additive are required in an anode containing Si nanoparticles as the active material to bind the active material while also providing adequate electronic conduction [4]. If the active material could be cycled without the presence of these components, the stresses generated in the nano-scale active material would be negligible. However, due to presence of other components that make up

the anode configuration, additional mechanical constraints are imposed on the active material during its electrochemical cycling.

In case of the Si thin film anode, the mechanical constraints on the lithiation-induced expansion of the Si thin film arise from its adhesion to the underlying current collector. However, when an elastic buffer layer is present between the current collector and the Si film, the extent of the constraint depends on the mechanical properties of the buffer layer. In Section 5.1, the effect of buffer layer elastic modulus on the amount of Si pattern interfacial delamination is reported. In Figure 26 (b-c), the deformed shapes of the buffer layer at the end of lithiation half-cycle with 3 different elastic moduli are shown (1 GPa, 10 GPa and 90 GPa) corresponding to the results reported in Figure 23 (i.e. $\sigma_c = 2$ GPa, $G_c = 15$ J/m^2). The contours of von Mises stress are also shown. For reference, Figure 26 (a) shows the undeformed shape of the buffer layer before the onset of lithiation. In the case of E_b=0.1 GPa and E_b =10 GPa (Figure 26 (a-b), the buffer layer is deformed significantly as the patterned Si adhered to it expands upon lithiation. Thus, the buffer allows unhindered expansion of the patterned Si film. However, when E_b=90 GPa, the buffer layer shows almost no deformation. Observation of the von Mises stress indicates that the stresses in the buffer with E_b=0.1 GPa do not exceed 0.2 GPa. On the other hand, stress in the buffer with E_b= 90 GPa exceed 3 GPa, with most of the buffer encountering stress higher than 1.3 GPa. The maximum von Mises stress present in the patterned Si at the end of lithiation in case of E_b=0.1, 10 and 90 GPa are 0.2, 1.1 and 1.3 GPa, respectively (not shown in the figure). This indicates that the mechanical constraints presented by the stiffer buffer ($E_b \geq$ 90 GPa) are significantly higher than that presented by relatively softer buffer layer ($E_b \leq 10$ GPa).

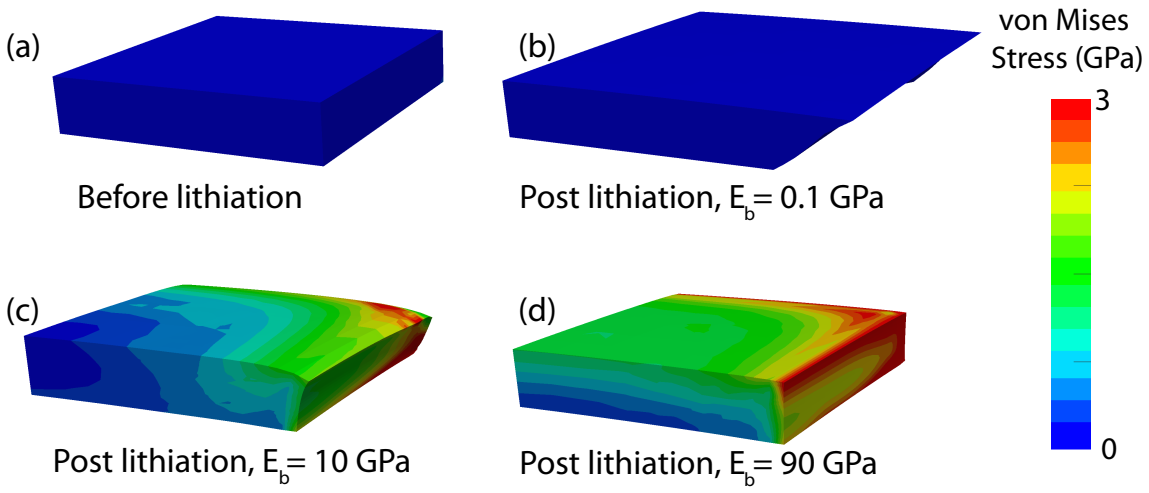

Figure 26. (a) Undeformed 100 nm thick buffer layer before lithiation of the anode system. von Mises stress contours in deformed shape of buffer layer with elastic modulus (b) 0.1 GPa, (c) 10 GPa and (d) 90 GPa. The shape of buffer layer are corresponding to the results reported in Figure 23 (σ =2 GPa, G_c= 15 J/m^2).

Presence of such mechanical constraints (e.g. adhesion of the patterned *a*-Si to the current collector) results in higher mechanical energy stored in the anode. In the case of the patterned Si anode, some energy is stored by elastic deformation of the anode components. For Si based anodes, some energy can also be dissipated by the plastic deformation of the Cu current collector[12] and the lithiated Si film [102]. Energy released through delamination (fracture) at the Si-buffer interface also caps the Ψ_{mech} as the mechanical constraints are reduced upon delamination.

In order to further understand the improved stability of the patterned thin film anode upon insertion of the elastic buffer layer, we studied the total mechanical energy in the anode configuration Ψ_{mech} (Equation (7.11)). To wit, we accounted for the mechanical energy in the Si thin film, Cu current collector as well as the elastic buffer layer. We partitioned the energy in the elastic and plastic part, and also enumerated energy required to propagate the interfacial

delamination. Corresponding to the results reported in Figure 23 (i.e. $\sigma_c = 2$ GPa, $G_c = 15$ J/m^2), we have plotted the total mechanical energy Ψ_{mech} of the patterned anode system at the end of lithiation ($soc = 1$) in **Figure 27** (a). The figure also shows the energy stored in the anode system by elastic deformation $\Psi_{elastic}$, and the energy dissipated by plastic deformation of its components $\Psi_{plastic}$, as well as the energy dissipated due to the interfacial delamination at the Si-buffer interface $\Psi_{interface}$. Mechanical energy in the anode system is directly indicative of the amount of mechanical constrains present on the patterned Si film during its electrochemical lithiation. We remind the readers here that our numerical framework assumed the volumetric expansion of the silicon thin film is stress free. Thus, in the absence of any mechanical constraint such as adhesion to the buffer layer and current collector, Ψ_{mech} in the anode system would be zero. Higher constraints lead to generation of higher stresses and is reflected in higher mechanical energy in the anode configuration. As it can be clearly seen from **Figure 27** (a), decreasing the buffer stiffness leads to decrease in Ψ_{mech}. This observation indicates that softer buffer layer reduces the mechanical constraint against free expansion of the patterned Si film by undergoing large deformation itself. Thus, the soft buffer layer acts as an intervening medium between highly deforming active component and lower deformation of current collector.

The distribution of $\Psi_{elastic}$ into the Si film ($\Psi^{Si}_{elastic}$), buffer layer ($\Psi^{Buffer}_{elastic}$) and the current collector ($\Psi^{Cu}_{elastic}$) is shown in **Figure 27** (b). Similar to **Figure 27** (b), distribution of $\Psi_{plastic}$ into the patterned Si film ($\Psi^{Si}_{plastic}$) and the Cu current collector ($\Psi^{Cu}_{plastic}$) is shown in **Figure 27** (c). When E_b < 1 GPa, the buffer layer deforms significantly as the patterned Si film expands during lithiation (as seen in Figure 26 (b)). As a result, the mechanical constraints on the patterned Si

are minimal. The stresses in Si film are low enough such that there is no plastic deformation. Furthermore, no stresses are transferred to the current collector which is reflected by the value of $\Psi_{elastic}^{Cu}$ and $\Psi_{plastic}^{Cu}$ (see **Figure 27** (b) and (c)). As the buffer layer has deformed significantly, $\Psi_{mech} \cong \Psi_{elastic}^{Buffer}$. Thus, when $E_b < 1$ GPa, the anode system undergoes only elastic deformation and no permanent deformation is encountered during the electrochemical cycling.

When the buffer layer is made stiffer ($E_b \geq 10$ GPa), the buffer layer cannot deform to sufficient extent owing to its higher stiffness (see Figure 26 (b-c)), as the patterned Si film expands during lithiation. Thus, the mechanical constraints imposed on the patterned Si due to its adhesion to the buffer layer increase as the buffer layer stiffness is increased. The stresses in the patterned Si film increase beyond its yield strength and the patterned Si film starts deforming plastically (indicated by the values of $\Psi_{plastic}^{Si}$ in **Figure 27** (c)). Plastic deformation in the lithiated Si limits the stresses generated in the active material [64, 103]. However, when sufficient energy can no longer be dissipated through plastic deformation of the Si, energy is released through delamination at the Si-buffer interface (see **Figure 27** (a), E_b>10 GPa), which releases the mechanical constraints on the patterned Si to some extent. Indeed, the properties of the interface significantly influence the amount of delamination as seen in Section 7.4.2.

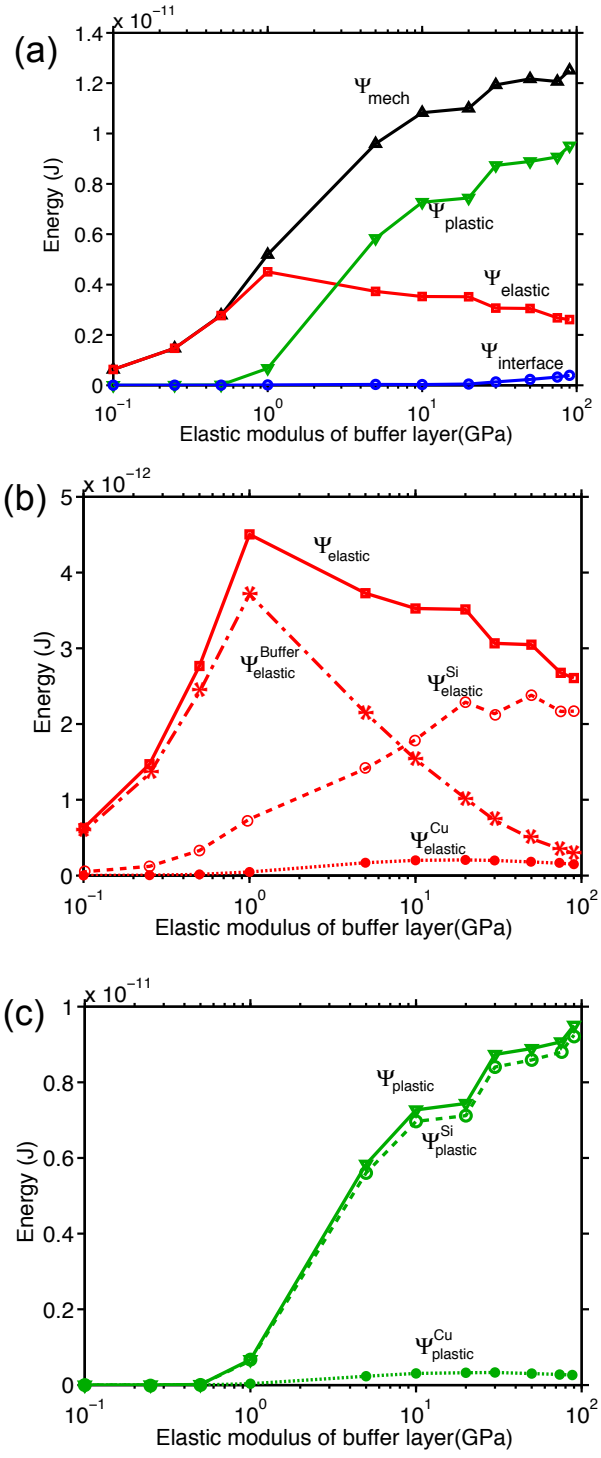

Figure 27. (a) Variation of the total mechanical energy, elastic energy, plastic energy and the energy dissipated due to fracture at interfaces in the anode configuration. (b) Distribution of the elastic energy in the anode components. (c) Distribution of the plastic energy in the anode components. All values are reported at soc = 1, σ =2 GPa and G_c= 15 J/m^2.

Another interesting aspect of reduction in the mechanical energy absorbed by the anode system Ψ_{mech} can be elucidated by Equation (7.12) and (7.14). Reduction in Ψ_{mech} would results in reduction of the overpotential energy loss (Ψ_{η}) [104]. Thus, reduction in the Ψ_{η} would increase the output energy Ψ_{out}. Since the output energy during discharge of a battery is directly proportional to the voltage, a higher output voltage will be observed in the voltage-capacity plot of anode electrochemical cycling for a given output current. Similar phenomenon has been experimentally observed by Yu et al. [16]. They show that due to incorporation of soft PDMS (Elastic modulus ~1 GPa) polymer layer in the current collector, the stresses in the active material are significantly relaxed. This results in observation of higher electrode potential during lithiation process. In fact, Sethuraman et al.[56] have estimated the stress-potential coupling and have shown that reduction in 1 GPa of stress in the active material can increase the lithiation potential ~62 mV. As a result, the overpotential losses are minimized and the energy efficiency of the anode can be expected to be higher.

Outcomes of simulations presented in Section 7.4 can be directly related to the excellent cycling performance shown by Datta et al. [21]. The report showed that presence of a 50 nm thick carbon buffer layer between the Cu current collector and the a-Si thin film electrode improves the anode capacity retention and prevents electrode mechanical degradation as otherwise observed in Si thin film present on Cu current collector. The concept of presence of buffer layer to alleviate volumetric expansion induced stresses in active material on an electrode is applicable not only in thin film electrodes but also in electrodes containing particles. Zhang et al. [96] have shown that presence of a layered material such as graphene in a composite with Si nanoparticles buffers the stresses resulting from alloying of Li-Si and thus preserving the integrity of the

composite electrode. In another study, Zhu et al. [105] have shown that the cellulose fiber can act as a natural buffer in a Sn coated cellulose fiber anode for Na ion battery.

Therefore, it can be concluded that the insertion of a softer buffer layer between patterned a-Si and Cu current collector facilitates accommodation of the strains caused by the diffusion-induced expansion of the patterned *a*-Si by reducing the mechanical constraints on the patterned *a*-Si thin film. Reduction in the total mechanical energy of the anode configuration prevents the dissipation of excess mechanical energy through the interface preventing delamination and thus improves the integrity of the anode configuration.

8.0 EFFECT OF SILICON CONFIGURATIONS ON THE MECHANICAL INTEGRIYT OF THE SILICON-CARBON NANOTUBE HETEROSTRUCTURED ANODE FOR LITHIUM ION BATTERY: A COMPUTATIONAL STUDY

8.1 INTRODUCTION

In order to address the issue of mechanical failure of silicon as the anode material, size of the active material has been identified as a major factor. Experimental as well as modeling studies have revealed that the use of nano-sized amorphous Silicon (*a*-Si) anode configurations in the form of nanoparticles [15], hollow nanospheres [106], nanowires [17], nanotubes [16], or nanofilm patterns [18] significantly improve the anode capacity retention over multiple electrochemical cycles. The critical sizes below which mechanical failure can be averted during electrochemical cycling have been identified for these configurations [13, 87, 106-108]. However, *a*-Si suffers from other issues such as poor electronic conductivity and charge transport, significant first cycle irreversible loss, inferior performance at higher charge rates, and low columbic efficiency. On the other hand, multiwall carbon nanotubes (MWCNTs) are known to have very good mechanical strength along with excellent electrical and thermal properties [25-27]. In addition, they exhibit moderate capacity of $\sim 300\ mAhg^{-1}$ following Li intercalation [109]. Thus, core-shell heterostructures comprised of carbon nanotube (CNT) core and nanostructured Si shell that combines the merits of both these anode elements have emerged as a promising candidate for Si based anode for Li-ion batteries.

Many researchers have recently reported synthesis of a Si-CNT core-shell heterostructure consisting of a thin continuous Si coating on the CNT. Hu et al. [10] deposited Si coating on CNT sponge structure by CVD. Electrochemical cycling of the heterostructure in a voltage range of 0.05 to 1 V showed an impressive first cycle discharge capacity of $3200\ mAhg^{-1}$ with 14% irreversible loss. After 50 cycles, however, the anode capacity faded to $1900\ mAhg^{-1}$. Formation of nanopores in the Si coating due to the high stresses encountered during electrochemical cycling was determined to be responsible for the capacity fade. Fu et al. [8] observed formation of axial cracks in the Si coating in the Si-CNT herterostructure post electrochemical cycling. In-situ TEM investigation by Wang et al. [11] on a heterostructure comprising of a thin (~13 nm) Si coating adhered to a carbon nano-fiber showed cracking of the Si coating during electrochemical cycling. They concluded that accumulation of damage in the Si coating over prolonged electrochemical cycling to be the mechanism for eventual capacity fade of the anode structure. A similar observation was reported by Sun et al. [9], where they observed the formation of axial cracks along the length of the continuous Si coating on CNT during in-situ electrochemical cycling of the heterostructure. It should be emphasized here that such axial cracks might not cause complete loss of capacity as long as the active material remains adhered to the CNT. For complete capacity fade, substantial loss of electronic contact between current collector and the active material mediated by disintegration of the active component is required.

Experimentalists have tested different strategies to limit the mechanical failure of the Si-CNT heterostructure thus improving its capacity retention, such as: providing sufficient inter-wire spacing [110, 111], improving adhesion at the Si-CNT interface [110], coating the Si film on CNT with a thin carbon layer [8, 112], and employing a binder free approach by directly scribing the active material onto current collector [113]. Another approach that has been tested to improve the

capacity retention of Si-CNT heterostructured anode is by tailoring the geometry of silicon shell to limit the Li alloying induced mechanical degradation. Gohier et al. [28] decorated vertically aligned thin CNTs of 5 nm diameter with 10 nm sized Si droplets. Providing sufficient free space for expansion of Si droplets resulted in a high reversible capacity of $3000\ mAhg^{-1}$ at 1.3 C *C-rate* with 90% capacity retention after 37 cycles. Work done in the Kumta group by Wang et al. [114, 115] has demonstrated the electrochemical performance of the hybrid Si-CNT heterostructure anode by synthesizing ~40 nm diameter droplets of Si tethered to MWCNT by CVD process. The heterostructure anode showed a steady capacity of $\sim 2000\ mAhg^{-1}$ for 22 cycles. Building on the work of Wang et al. [114, 115], Epur et al. [29] varied the morphology of *a*-Si coated on the CNT by changing the flow conditions in the CVD process. The synthesis yielded two different Si geometries in the Si-CNT heterostructure based on the flow conditions: continuous Si film on CNT, and Si droplets deposited on CNT. The heterostructure with continuous Si film showed an initial capacity of $\sim 3200\ mAhg^{-1}$ with 10% first cycle irreversible loss. After 20 cycles the capacity dropped to $\sim 1950\ mAhg^{-1}$. In case of the heterostructure with Si droplet configuration, an initial capacity of $\sim\sim 2700\ mAhg^{-1}$ with 10% first cycle irreversible loss was observed. However, the capacity fade rate was considerably less and a capacity of $\sim 2340\ mAhg^{-1}$ was retained after 20 cycles. Thus, the electrochemical cycling results consistently demonstrated that the droplet configuration outperformed the film configuration. It can be inferred from the above-mentioned experimental observations that the geometrical features of Si can alter the anode cyclic performance significantly, and thus can be a promising route to design anode configurations with improved cyclic performance.

Motivated by this objective, the effect of the geometry of the active material in the Si-CNT heterostructures on its mechanical integrity during a single electrochemical cycle is explored. The modeling framework presented in **Chapter 4.0** is utilized to study alloying induced stress and consequent mechanical failure of the electrode material. In the course of this paper, the geometry of the Si film coating on CNT is systematically varied from a continuous Si film to a Si particle in the shape of $1/8^{th}$ of a nano-ring adhered to CNT. Mechanical integrity of the different configurations is analyzed by studying mechanical stress state as well as plastic flow within the active material. Possible nucleation and growth of voids in the plastic solid leading to the mechanical failure of silicon is of particular interest. It is demonstrate that the mechanical constraints arising from the adhesion of Si shell to the CNT core, as well as the configuration of the active material itself, is responsible for the mechanical failure of the anode configuration. Providing sufficient free space for Si expansion and thus reducing the mechanical constraints significantly reduces the stresses, thus improving its mechanical integrity during electrochemical cycling. The simulation results are related to the experimental observations found in the literature whenever possible.

In the next section, description of the heterostructure configurations under consideration and the relevant materials properties as well as boundary conditions utilized in the simulation are detailed. Results obtained from the simulation studies and a brief discussion on it is presented in **Sections 8.3 and 8.4**, respectively. The conclusions and future directions from the work presented in this research article are summarized in the last section.

8.2 MODEL GEOMETRY AND SIMULATION PARAMETERS

Epur et al. [29] previously reported electrochemical performance of Si-CNT heterostructure consisting of nano-crystalline / amorphous continuous Si film of 50 nm thickness deposited on multi-walled CNTs. Accordingly, a single multi-walled CNT (inner diameter of 10 nm and outer diameter of 80 nm) with a continuous Si coating of thickness 50 nm is considered for the modeling purpose. A finite sized straight segment of length 400 nm is selected for this configuration, as shown in Figure 28 **(a)**. However, the experimental heterostructures are very long in the axial direction. To include the effect of "infinite" length in our finite sized model, top and bottom edges of the computational domain were constrained with generalized plane-strain boundary conditions.

To study the effect of geometry of the active component, the Si domain was varied systematically while keeping the dimensions of the CNT constant. The continuous film discussed above is labeled as Configuration I. For Configuration II, the span of the Si film coating in the axial direction was reduced creating nano-rings of Si having a thickness of 50 nm in both radial and axial directions. It is assumed that the adjacent nano-rings were separated sufficiently so that they do not interact with each other mechanically. Accordingly, for the simulation purpose, only one nano-ring of Si tethered to the CNT was considered (Figure 28 **(b)**). The generalized plane-strain boundary condition was applied only on CNT for this case; the Si domain was free to move in the axial direction. In the third configuration (labeled as Configuration III), continuity of the active material in the circumferential direction was reduced further: A particle of Si in the shape of $1/8^{th}$ of the nano-ring adhered to the CNT was considered (see Figure 28 **(c)**). The dimensions of the active material in the radial and axial directions were chosen as 50 nm so that it approximates a droplet. As before, the ends of the carbon nanotube were provided with

generalized plane-strain boundary condition, while the surfaces of the active material not adhered to the CNT were free.

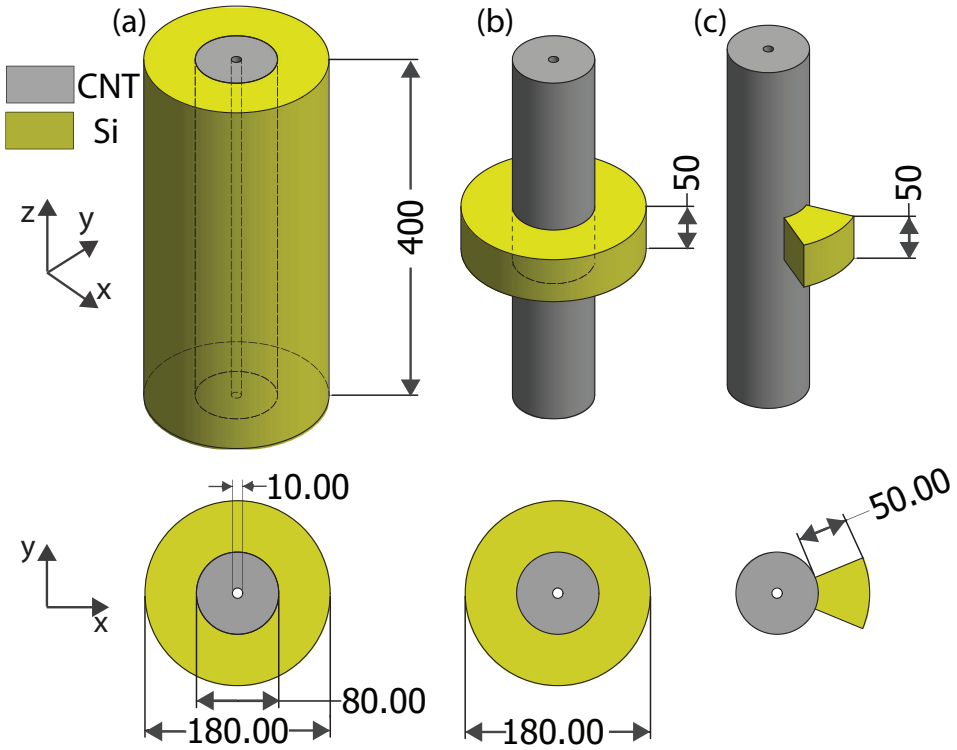

Figure 28. Schematics of Si-CNT heterostructure anode geometries studied. (a) Continuous Si film coating on CNT (b) Si nano-ring adhered to CNT and (c) 1/8th of Si nano-ring adhered to CNT. Dimensions of the anode heterostructure components are specified in nm.

Exploiting the advantage of the axisymmetric geometry of the anode configurations, only 1/8th of the actual geometry is considered for the FE simulations of the Si-CNT heterostructure with continuous Si coating and Si nano-ring to reduce the computational effort. Assuming the length of the CNT oriented along the z-axis and the origin (0,0,0) located midway along the length of the CNT, a 1/8th section of the geometry between the X, Y and Z planes passing through the origin was taken for simulation in case of the Configuration I and II (see Figure 28

for orientation of axes). Symmetry boundary conditions were employed on the XY, YZ and XZ planes. In case of the 1/8th of the Si nano-ring adhered to CNT, 1/4th section of the geometry between the X and Z planes passing through the origin and having symmetry boundary conditions on the XZ and XY plane was utilized for FE simulation. The domains were meshed with 8 noded hexahedral elements using the CUBIT meshing software [116], resulting in 8959, 9568 and 6996 elements for Configuration I, II and III, respectively. The interface between Si and the CNT was modeled with 289. 130, and 132 8-noded cohesive elements of zero thickness for Configuration I, II and III, respectively [76, 117, 118].

During the simulation of one electrochemical cycle of the Si-CNT heterostructure, the active material (*a*-Si) was cycled (alloyed and de-alloyed) at C/4 charge rate under galvanostatic conditions up to the theoretical electrochemical capacity of $4200\ \mathrm{mAh\,g^{-1}}$. The partial molar volume of Li in Si (η) was considered to be $4.5\times10^{-6}\ \mathrm{m^3\,mol^{-1}}$ [76, 117] (see Equation (4.9)). Li concentration dependent diffusivity of Li during lithium alloying/de-alloying with silicon was taken as [9, 119-121] $D(\boldsymbol{X},t) = D_0(1/(1-c(\boldsymbol{X},t)) - 4\,c(\boldsymbol{X},t))$, where D_0 is the diffusivity constant. To avoid any numerical instability during the finite element simulations, the maximum Li diffusivity was limited as $\max(D(\boldsymbol{X},t)) = 10^3 D_0$ i.e. $10^{-15}\ \mathrm{m^2\,s^{-1}}$, which is comparable to the experimentally calculated average value of $0.51\times10^{-15}\ \mathrm{m^2\,s^{-1}}$ [122].

Table 3. Material properties employed for the Si-CNT heterostructure simulations.

Young's modulus of *a*-Si (E_0^{Si})	90 GPa [57]
Rate of change of elastic modulus of a-Si with Li fraction (ω)	71.25 GPa/ $Li_{fraction}$
Poisson's ratio of *a*-Si (ν_0^{Si})	0.28
Yield strength of *a*-Si (σ_y^{Si})	1.5 GPa [107]
Hardening modulus of Si (H^{Si})	1 GPa
Average fracture strength of *a*-Si during electrochemical cycling (σ_c^{Si})	1.6 GPa [123, 124]
Young's modulus of multiwalled CNT (transverse isotropic material properties)	E_r^{CNT} = 10 GPa [125] E_t^{CNT} = 200 GPa [25]
Si-CNT interface fracture strength (σ_c^{Si-CNT})	0.5 GPa
Si-CNT interface toughness (G_c^{Si-CNT})	5 J/m^2
Diffusivity of Li in Si (D_o)	10^{-18} m^2/s [9]

Experiments have shown that lithiated Li-Si alloy has significantly lower fracture strength as compared to the pristine Si [123, 124]. Accordingly, for the simulations, an average fracture strength (σ_c^{Si}) of 1.6 GPa [124] for Si was assumed. Since CNTs are known to be stiffer in the axial direction as compared to the radial direction, it was assumed to have transversely isotropic materials properties [125]. As the CNTs are known to have very high mechanical strength,

the study focuses on the mechanical response of the Si. Compressible Neo-Hookean constitutive model was used for all the materials to simulate the large deformation mechanical response. The materials and interfacial properties used for the simulations are reported in Table 3.

8.3 RESULTS

In this section a detailed parametric study of the effect of Si configuration on the mechanical response of heterostructured anodes during an entire electrochemical cycle is presented. First the evolution of Li concentration and mechanical stress field generated in the active material during the entire electrochemical cycle is examined. The calculated stress components were post-processed to enumerate hydrostatic stress σ_m, effective stress σ_e (also called von Mises stress) and the stress triaxiality ($T = \sigma_m / \sigma_e$) at different normalized cycle time (τ). Visualization of the results were performed using the software ParaView [126]. It is found that the magnitude of peak effective stress (σ_e) is high enough to cause plastic flow of silicon. Accordingly, next the evolution of plasticity in the different Si configurations considered in this study with the electrochemical cycling is presented. One of the prominent mechanisms of ductile failure of materials is the nucleation, growth and coalescence of voids in the plastic region. Thus finally study the possibility of void nucleation and growth in the active silicon component during electrochemical cycling that might give rise to mechanical failure is presented.

8.3.1 Electrochemical cycling of the heterostructure and volume expansion of silicon

Evolution of Li concentration and the attendant volumetric expansion for the different Si configurations of the active material during lithium alloying half-cycle ($\tau = 0$ to 0.5) are presented in Figure 29 **(a-c)**. Figure 29 **(a)** shows the evolution of the normalized lithium concentration ($c_{Li} / c_{Li\max}$) at different normalized cycle times (τ) along the longitudinal (LONG) section (XZ plane) of the Si film coating (Configuration I). Normalized cycle time $\tau = 0.0$ corresponds to the start of lithium alloying, $\tau = 0.5$ indicates end of lithium alloying, while $\tau = 1.0$ indicates the end of a full alloy-based delithiation (de-alloying) i.e. completion of one electrochemical cycle.

The Li concentration at the outer regions of silicon that are exposed to the electrolyte builds faster as compared to the inside and the resulting front of Li moves inwards expanding the silicon domain as the lithium alloying progresses. It can be observed from Figure 29 **(a)** that the Si film expands primarily in the radial direction (~83.6%), accompanied by a small expansion in the axial direction (~2.4%). In the case of Configuration II, the lithium alloying front in the Si nano-ring propagates inwards from the top, bottom and the circumferential boundaries that are exposed to the electrolyte. Si can be seen to expand in the radial as well as axial direction (Figure 29 **b)**). Displacements calculated from the FE simulations indicate that Si expands about ~41% in both the radial as well as axial directions. In the third configuration, Li transport occurs in the radial, axial and circumferential directions as it has five surfaces exposed to the electrolyte. In this case, the ratio of the surface area exposed to the electrolyte to the active material volume is the highest among the three different heterostructured configurations considered. Therefore, the Li concentration profile in the active material geometry is more uniform as compared to the first

two configurations (Figure 29 **(c)**). Reducing the continuous Si film coating to 1/8th of the Si nano-ring allows the Si expansion to occur in the radial, axial as well as the circumferential direction during the alloying half cycle. The simulations show that Si expands ~39% in the radial and axial direction, and ~37 % in the circumferential direction, indicative of the uniform expansion occurring from Li alloying.

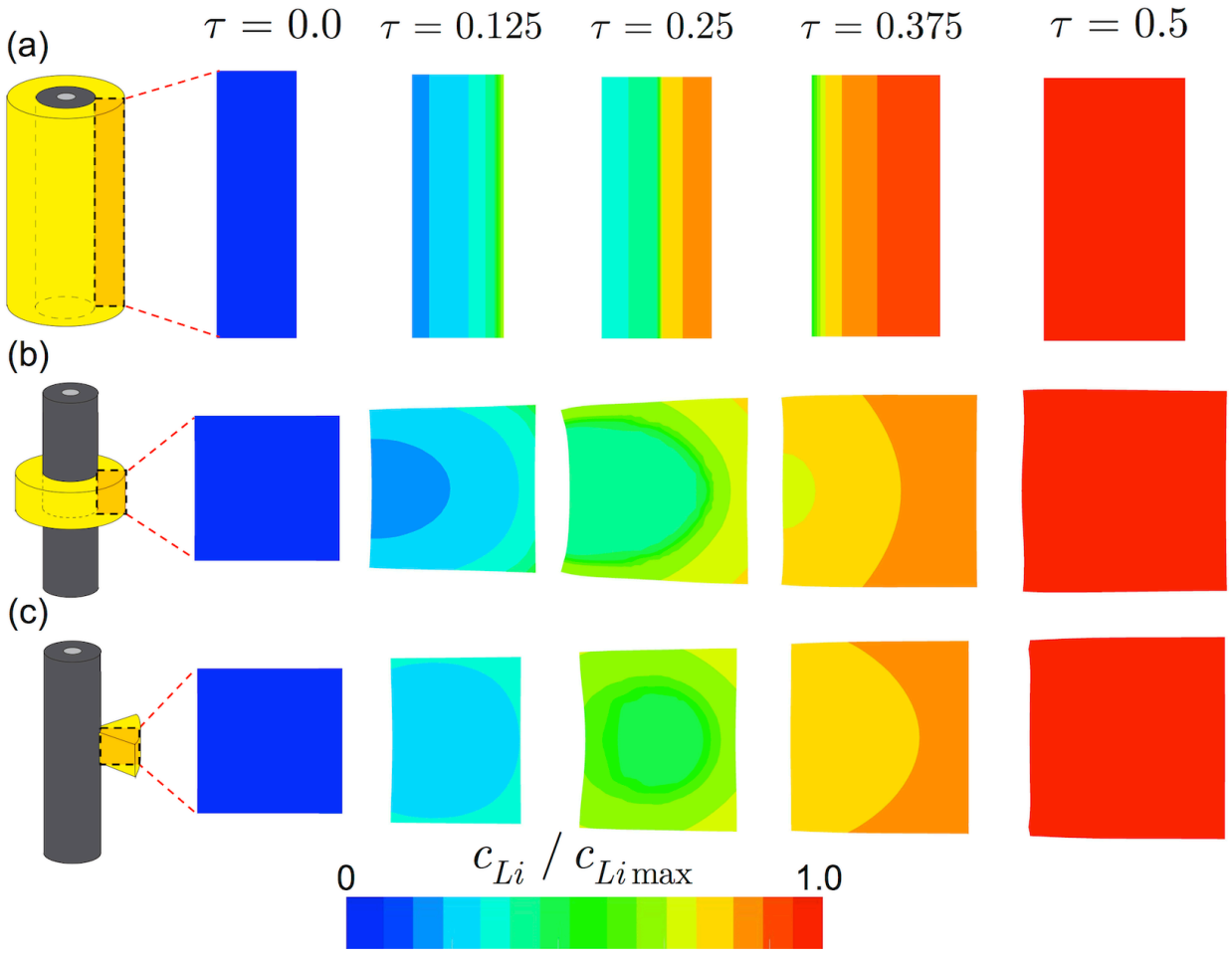

Figure 29. Evolution of normalized Li concentration ($c_{Li} \,/\, c_{Li\,\max}$) in Si during lithium alloying half cycle along the longitudinal (LONG) section (XZ plane) of a (a) **continuous Si thin film on CNT,** (b) **Si nano-ring tethered around CNT and** (c) **1/8th of Si nano-ring tethered to CNT at different normalized cycle times (τ).**

Along with the geometry of the Si configuration, the dimensions of the active material are also expected to affect the Li concentration profile in the Si. The effect of Si configuration dimensions on the Li concentration profiles and the attendant stresses in Si is detailed in **APPENDIX F**.

8.3.2 Stress analysis of different silicon configurations in Si-CNT heterostrcutres

Figure 30 **(a-j)** shows the contours of the radial stress (σ_{rr}), axial stress (σ_{zz}), circumferential stress ($\sigma_{\theta\theta}$), effective stress (σ_e) and the plastic strain (ε_p) in the longitudinal section of the Si film coating in the continuous Si-CNT heterostructure at the end of alloying ($\tau = 0.5$) and de-alloying ($\tau = 1.0$). The scale bar for normal stress components shows a lower limit of compressive stress of magnitude $1.0\ GPa$ and the upper limit is capped at 1.75 GPa tensile stress, which is slightly greater than the average fracture strength of Si ($\sigma_c^{Si} = 1.6\ \text{GPa}$) [124]. From Figure 30 **(a) and (f)**, it can be seen that the magnitude of σ_{rr} is negligible at the end of alloying as well as de-alloying. As discussed in **Section 8.3.1**, during electrochemical cycling, the Si film coating can expand freely in the radial direction and thus no stress is generated in this direction. However, as the axial deformation is constrained due to continuity of the Si domain in that direction, large compressive axial stress is generated during alloying of lithium (Figure 30 **(b)**). Distribution of effective stress at the end of cycling (Figure 30 **(d)**) reveals that the yield stress of the material (1.5 GPa) is exceeded in the Si coating. This phenomenon causes Si to undergo inelastic deformation leading to accumulation of plastic strain (Figure 30 **(e)**). During de-alloying, as the Li is extracted out from the Li_xSi alloy, presence of the plastic regions leads to tensile stresses in the axial direction in the active film. The tensile axial stress observed at the

end of de-alloying (Figure 30 **(g)**) is greater than its fracture strength σ_c^{Si}. This fact putatively validates and also inexplicably serves to explain the experimental observation of axial cracks in the Si nanofilm adhered to the carbon nanotube post electrochemical cycling [8]. In addition, there is further accumulation of considerable plastic strain in the Si coating (Figure 30 **(j)**) during de-alloying. Observe that plastic strain is highest (and in excess of 0.5) at the interfacial region as well as near the free edge of Si film. Presence of substantial plastic flow in the Si nano-films has also been reported by [55, 56]. These are also the potential locations for void nucleation and growth that will be discussed in the next section. The circumferential stress at the end of alloying shows the presence of compressive stress near the Si-CNT interface (~-0.9 GPa). However, during de-alloying the inelastic deformation of Si leads to generation of tensile circumferential stress of magnitude ~1.5 GPa near the Si-CNT interface (Figure 30 (h)). This magnitude is comparable to the fracture strength of *a*-Si σ_c^{Si} signifying circumferential cracking in the XZ plane may also appear near the interface at the end of de-alloying half cycle. The results could substantiate the observed capacity fade reported by Epur et al. [29] as per discussed in the next section.

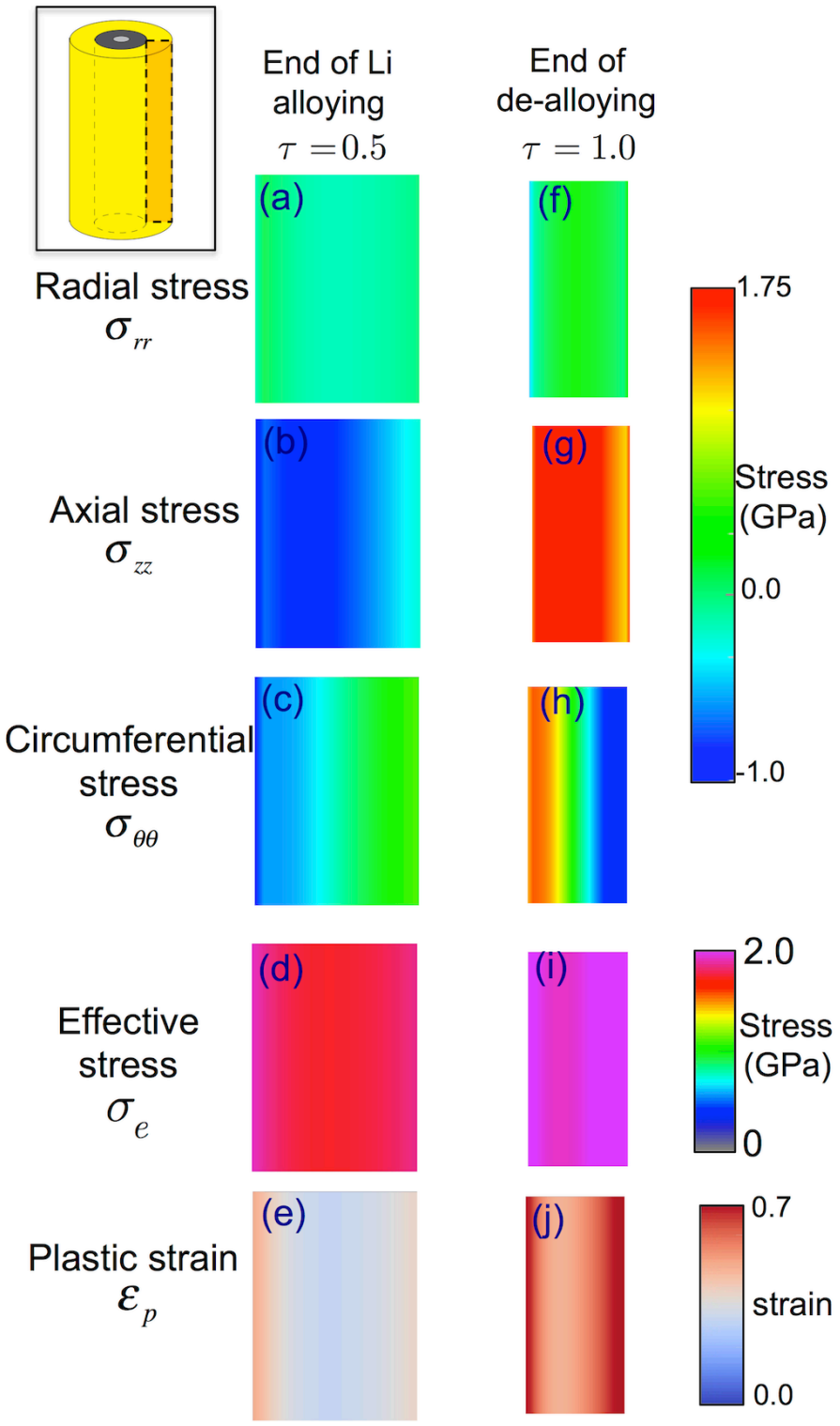

Figure 30. Radial stress, axial stress, circumferential stress, von Mises stress and plastic strain contours in the longitudinal section (XZ plane) of continuous Si coating in first Si-CNT heterostructure configuration at the end of lithium alloying (a-e) and at end of de-alloying (f-j).

Stress and plastic strain contours at the longitudinal section of Si nano-ring in the second heterostructured configuration at the end of alloying ($\tau = 0.5$) and dealloying half cycle ($\tau = 1$) are shown in Figure 31 **(a-j)**. As observed from Figure 31 **(a) and (f)**, the radial stresses occurring at any location in the Si nano-ring are much lesser than σ_c^{Si}. During Li alloying, the adhesion of Si nano-ring to the CNT presents mechanical constraints to the axial expansion of Si only in the vicinity of the Si-CNT interface. As a result, the fully lithiated Si nano-ring shows presence of compressive stress near the Si-CNT interface (Figure 31 **(b)**). Interestingly, the axial stresses show a significant reduction (Figure 31 **(g)**) compared to the continuous nanofilm configuration presented (Figure 30 **(g)**). Again, this reduction is a direct consequence of release of the axial constraint on the active material by choosing the nano-ring configuration. However, contours of circumferential stress shown in Figure 31 **(h)** indicate that near the center of the nano-ring, the Si still has significant circumferential stress (1.45 GPa) that is comparable to σ_c^{Si}. Plastic region in the Si nano-ring at the end of the electrochemical cycle (Figure 31 **(j)**) is also reduced as compared to that shown in Figure 30 **(j)**. The maximum value of plastic strain is observed near the Si-CNT interface, albeit much reduced in magnitude compared to the last configuration. Corresponding to the maxima of plastic strain, the maximum value of effective stress are obtained near the Si-CNT interface (Figure 31 **(i)**) at the end of the de-alloying cycle.

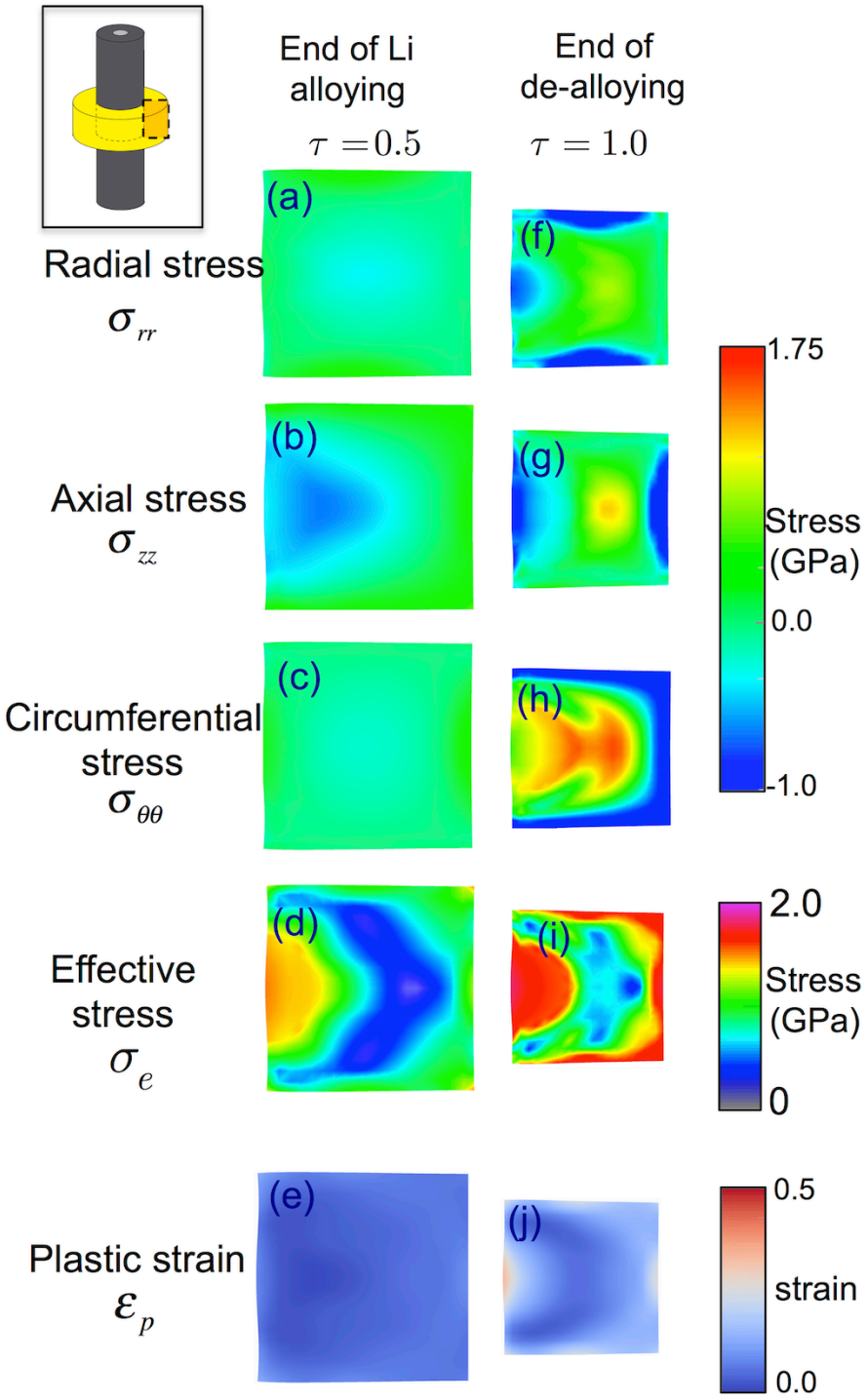

Figure 31. Radial stress, axial stress, circumferential stress, von Mises stress and plastic strain contours in the longitudinal section (XZ plane) of the Si nano-ring in second Si-CNT heterostructure configuration at the end of lithium alloying (a-e) and at end of de-alloying (f-j).

For Configuration III, the mechanical constraints on Si are further reduced in the circumferential direction as compared to the Si nano-ring. Accordingly, the active material expands in radial, axial, as well as circumferential directions. Stress contours in Figure 32 show a significant reduction of all three components of stresses (radial, axial and circumferential) as compared to that observed in the continuous Si film coating (Figure 30) as well as the Si nano-ring configuration (Figure 31). Again, similar to the nano-ring configuration, the axial stresses observed at the end of de-alloying half cycle near the Si-CNT interface are compressive (Figure 32 **(b)**). However, it is important to note that the effective stress (Figure 32 **(i)**) and the residual plastic strain (Figure 32 **(j)**) accumulated in the active material at the end of electrochemical cycling ($\tau = 1$) are considerably less (less than ~0.2 everywhere except two points at the interface) than that observed in both the previous Si morphologies (continuous Si film coating and Si nano-ring).

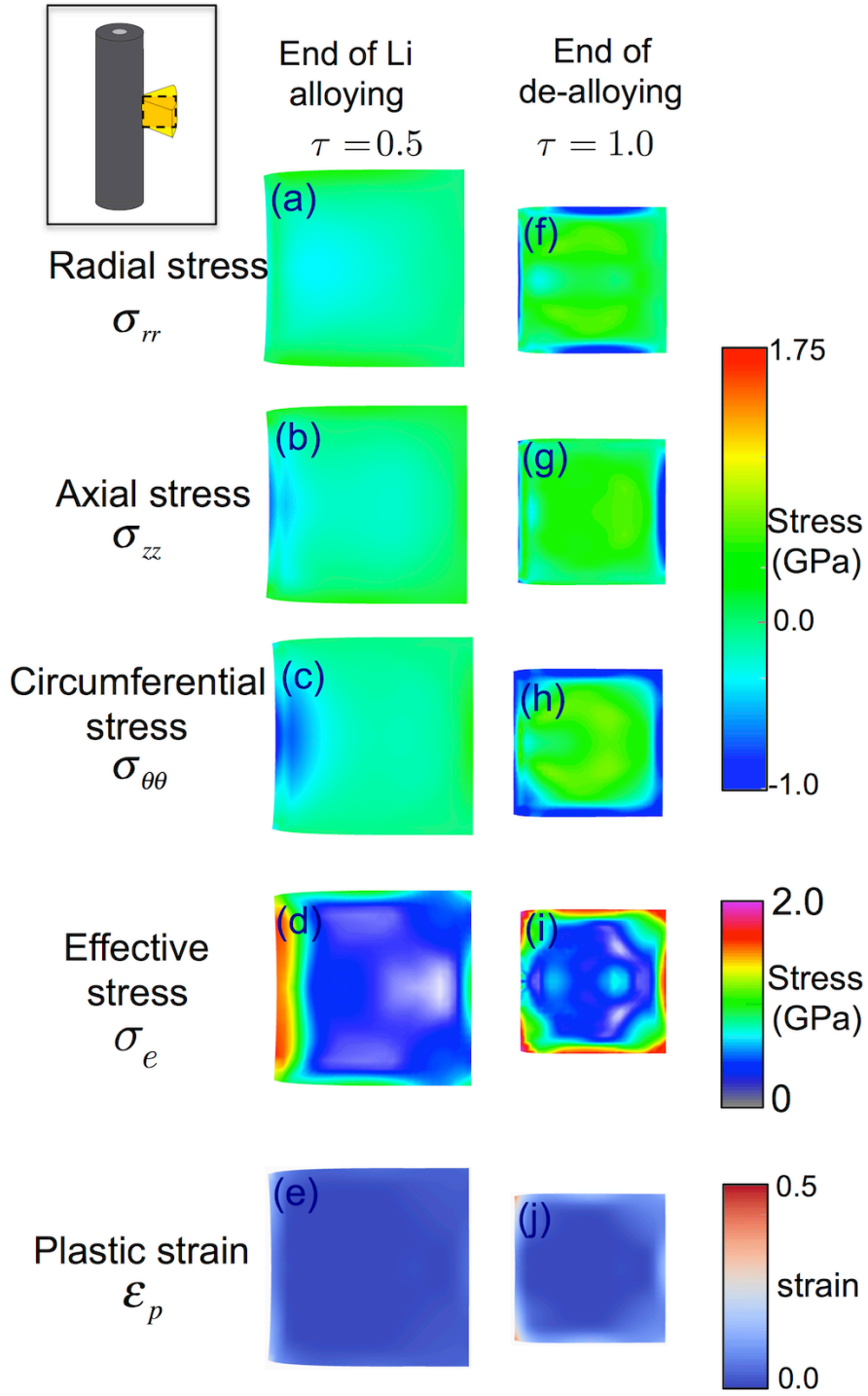

Figure 32. Radial stress, axial stress, circumferential stress, von Mises stress and plastic strain contours in the longitudinal section (XZ plane) of the 1/8th of the Si nano-ring in third Si-CNT heterostructure configuration at the end of lithium alloying (a-e) and at end of de-alloying (f-j).

8.3.3 Evolution of effective stress, hydrostatic stress and stress triaxility

Plastic regions in the silicon domains serve as potential locations for void nucleation and growth induced material degradation and failure. Voids may nucleate when the linear combination of effective stress and tensile hydrostatic stress exceeds the local void nucleation strength [127]. Once nucleated, the voids may grow under the influence of high stress triaxiality [128-130]. To understand the feasibility of void nucleation and growth in the Si-CNT heterostructured anode, the evolution of the combination of the effective and hydrostatic stress ($\sigma_e + \sigma_m$) and the stress triaxiality ($T = \sigma_m / \sigma_e$) is studied during electrochemical cycling of the anode. In Figure 33 **(a-c)**, plot of $\sigma_e + \sigma_m$ and T at different normalized radial thicknesses ($\overline{r}$) in the continuous Si coating for the first Si-CNT heterostructure configuration considered is shown. Normalized radial thickness of $\overline{r} = 1$ corresponds to the outer surface of Si exposed to the electrolyte, while $\overline{r} = 0$ corresponds to the inner Si-CNT interface. For better representation of the stress triaxiality data, the lower limit of T is capped at 0 (i.e. when hydrostatic stress is negative) and the upper limit at 1.5. As the de-alloying progresses, $\sigma_e + \sigma_m$ can be seen to increase steadily at $\overline{r} = 1$. After $\tau = 0.7$, $\sigma_e + \sigma_m$ exceeds 2 GPa (higher than σ_c^{Si}=1.6 GPa) indicating conditions favorable for void nucleation. The stress triaxiality remains low beyond this time point signifying that voids may not grow even if they nucleate. However, conditions favorable to the nucleation as well as growth of voids can be found to exist in at $\overline{r} = 0.5$ (Figure 33 **(b)**) and at $\overline{r} = 0$ (Figure 33 **(c)**) towards the end of Li de-alloying.

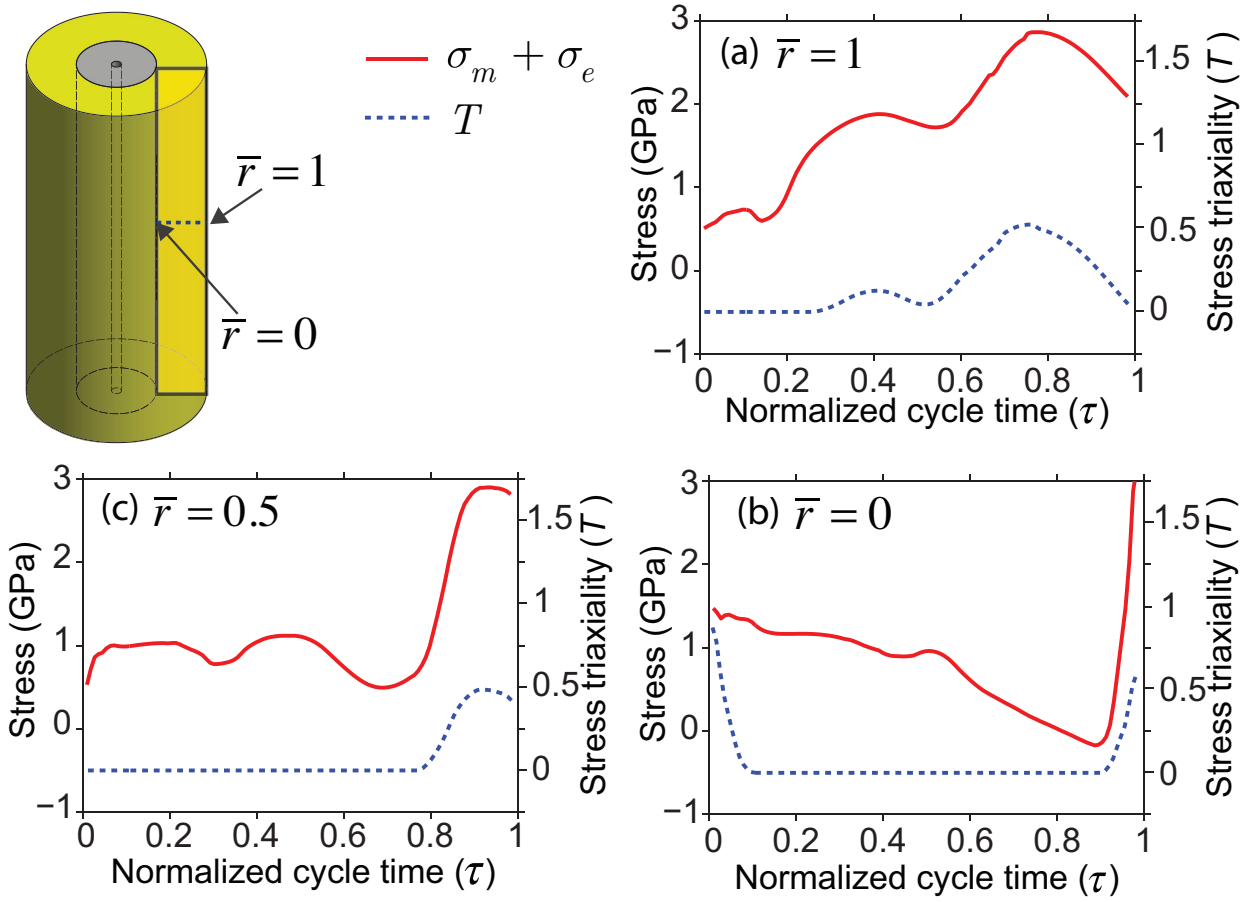

Figure 33. Evolution of combination of effective and hydrostatic stress ($\sigma_e + \sigma_m$) and stress triaxiality (T) in the continuous Si coating in the first Si-CNT heterostructure at the normalized radial thickness of (a) $\overline{r} = 1$, (b) $\overline{r} = 0.5$ and (c) $\overline{r} = 0$.

In Figure 34 **(a-c)**, the evolution of $\sigma_e + \sigma_m$ and T at three different normalized radial thicknesses along a central line in the Si nano-ring is plotted. From Figure 34 **(a)**, it can be observed that the stress triaxiality T never exceeds 0.5. Similar situation can be observed in Figure 34 **(c)**). Nonetheless, Figure 34 **(b)** shows that at $\tau = 0.97$, the value of $\sigma_e + \sigma_m$ can reach 1.7 GPa with concomitant very high stress triaxiality (≥1.5). Thus, at the completion of the

electrochemical cycle, the Si nano-ring may show void growth induced mechanical degradation around $\overline{r} = 0.5$.

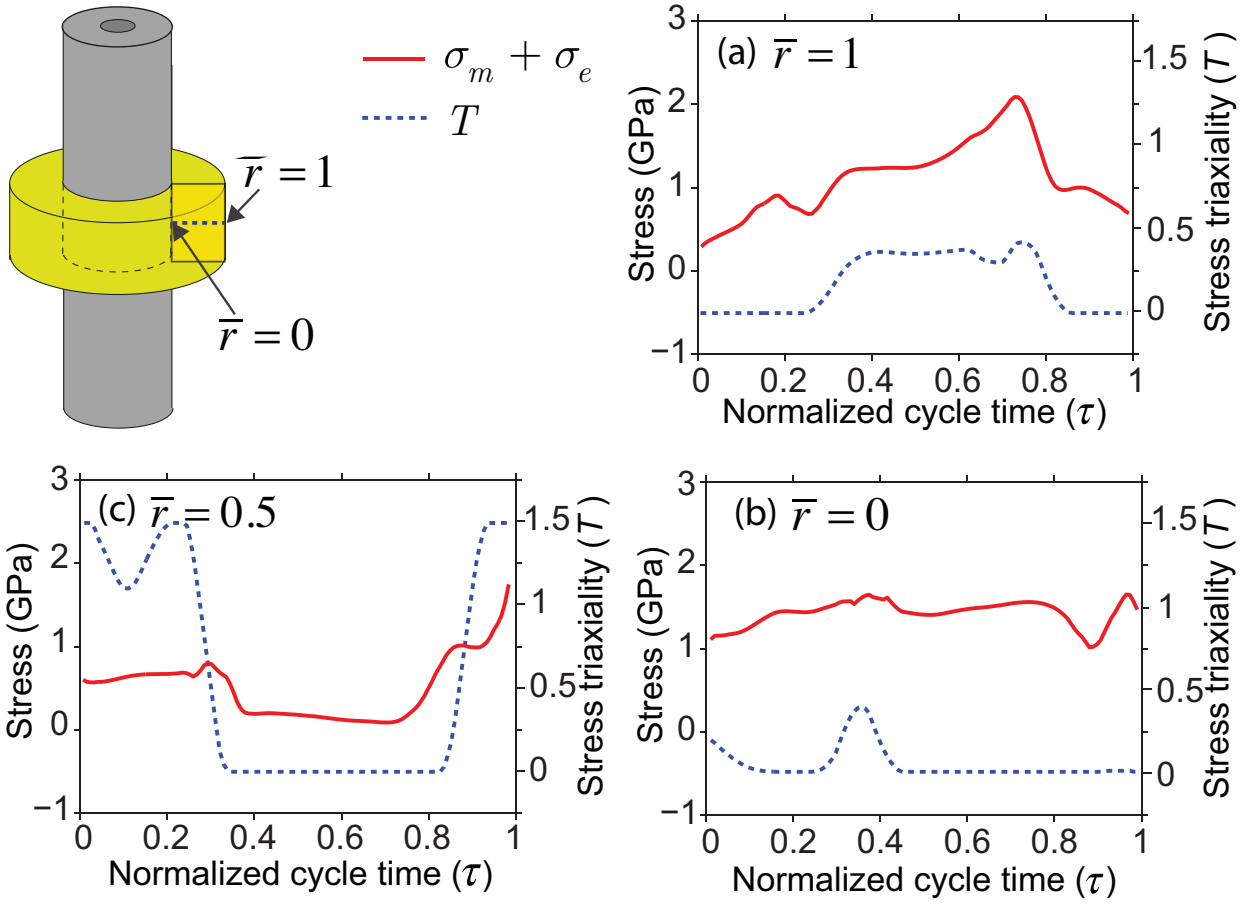

Figure 34. Evolution of combination of effective and hydrostatic stress ($\sigma_e + \sigma_m$) and stress triaxiality (T) in the Si nano-ring in the second Si-CNT heterostructure at the normalized radial thickness of (a) $\overline{r} = 1$, (b) $\overline{r} = 0.5$ and (c) $\overline{r} = 0$.

Similar to Figure 34, data is plotted in Figure 35 **(a-c)** for the 1/8th of the Si nano-ring. At $\overline{r} = 1.0$, although the combination of effective and hydrostatic stress ($\sigma_e + \sigma_m$) exceeds the fracture strength of Si, the stress triaxiality T is not sufficient to cause void growth (Figure 35

(a)). In case of $\bar{r} = 0.5$ and $\bar{r} = 0$, it can be observed that $\sigma_e + \sigma_m$ does not exceed the fracture strength (Figure 35 **(b) and (c)**), even though the stress triaxiality is favorable for void growth at these locations. Thus, void nucleation is unlikely to occur in the active material in this Si-CNT heterostructure configuration indicating the likely uncanny stability of this configuration during electrochemical cycling as reported in the experimental work of Epur et al., [29] further discussed in detail in the next section.

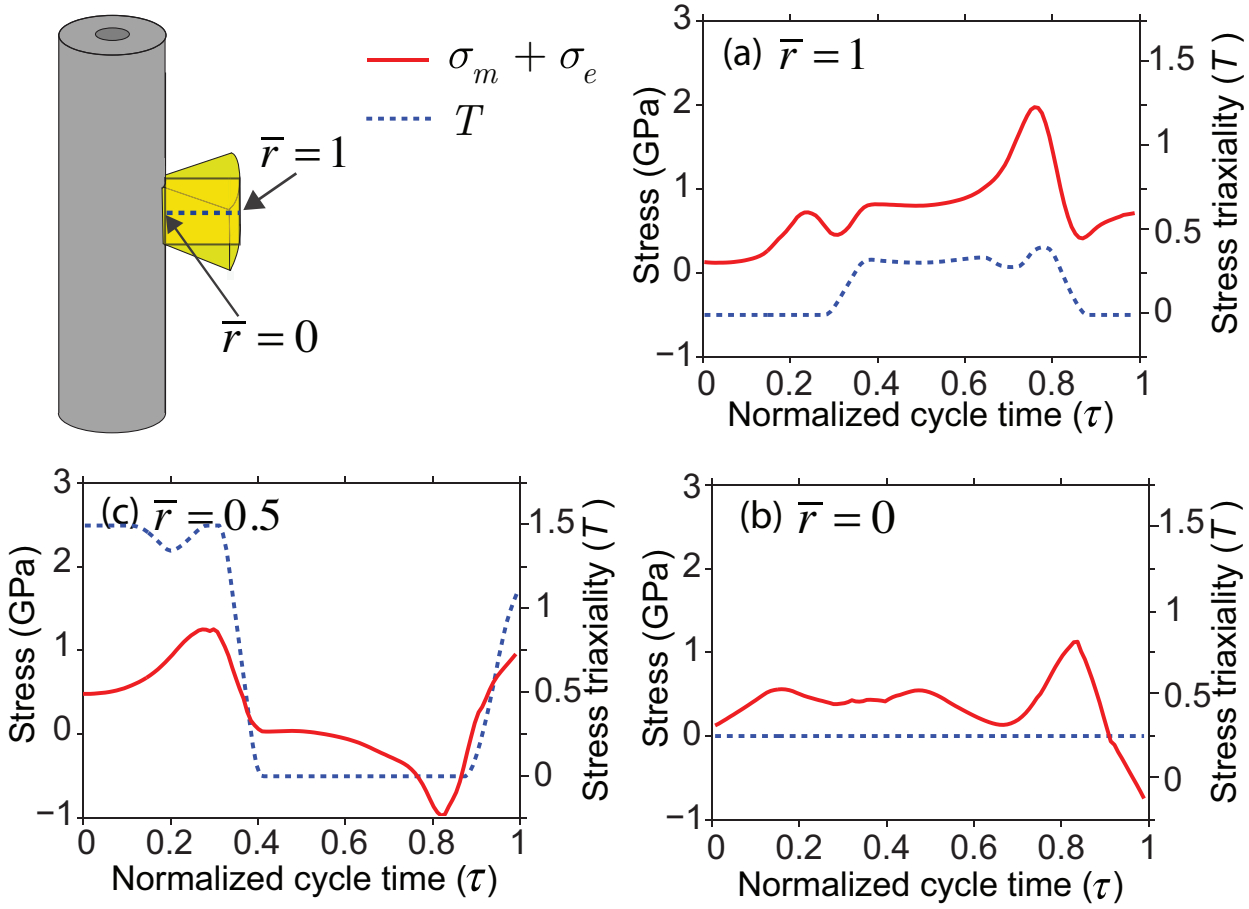

Figure 35. Evolution of combination of effective and hydrostatic stress ($\sigma_e + \sigma_m$) and stress triaxiality (T) in 1/8th of the Si nano-ring in the third Si-CNT heterostructure at the normalized radial thickness of (a) $\bar{r} = 1$, (b) $\bar{r} = 0.5$ and (c) $\bar{r} = 0$.

8.4 DISCUSSION

In this chapter, mechanical response of different Si morphologies in Si-CNT heterostructure is studied during a complete electrochemical cycle by utilizing a novel multiphysics modeling framework presented in **Chapter 4.0** . It is demonstrated that mechanical constraints from the bonding between carbon nanotube and silicon domain have a profound effect on the stress state in the active component. In the Si-CNT heterostructured configuration with continuous Si coating, the mechanical constraints imposed by the adhesion of Si film to CNT limits the expansion of Si in axial direction. Thus, the lithium alloying induced volumetric expansion was accommodated only along the radial direction (Figure 29 **(a)**). Similar observation has been reported by in situ TEM studies by Wang et al. [11]. In the case of the Si nano-ring adhered to CNT, the dimensions of the continuous Si film coating was reduced in the axial direction, which alleviated the mechanical constraints on the Si in the axial direction. Adhesion of the Si nano-ring to CNT at the inner surface of Si nano-ring presents a certain amount of mechanical constraint. However, expansion of Si in the axial direction at the Si-CNT interface was allowed, the extent of which would depend on the adhesion properties of the interface. Away from the Si-CNT interface, the active material can expand in radial as well as axial direction as it can be seen from Figure 29 **(b)**. For the last configuration with $1/8^{th}$ of the Si nano-ring adhered to the CNT, the mechanical constraint on the active material are the least as Si can expand in radial, axial, as well as the circumferential direction during electrochemical cycling (Figure 29 **(c)**).

The stress contours shown in Figure 30 reveal that there is significant axial and circumferential stress in the continuous Si film coating at the end of the electrochemical cycle. Similar observations have been made by Wang et al. [120] for the stresses observed at the end of the electrochemical cycle in a thin layer of Si coated on carbon nano-fibers. Such high axial tensile

stress observed at the end of de-alloying can cause axial fracture in the Si coating. These axial cracks can expose additional area of Si to the electrolyte and the formation of solid-electrolyte interphase (SEI), irreversibly consuming lithium and resulting in poor coulombic efficiencies. However, axial cracking of silicon thin film may alone not cause electrochemical capacity fade as long as the Si film maintains a current collecting pathway. Thus additional mechanisms must be in effect to explain the substantial loss of capacity for Si-CNT heterostructures after repeated electrochemical cycling. It is determined that very high diffusion induced stress in silicon may result in its substantial plastic flow, which may activate ductile failure mechanisms and eventual disintegration of the active component. The ductile failure can be mediated by nucleation, growth and coalescence of voids from the structural pores present in lithiated amorphous silicon. This phenomenon may bring gradual mechanical failure of the active component over many electrochemical cycles. Fracture of silicon results in volumetric loss in active material and thus reduction in electrochemical capacity. This observation may explain the gradual disintegration of silicon and attendant capacity fade over multiple electrochemical cycles as observed in many experiments [8, 29, 112]. It has been experimentally observed that amorphous silicon can undergo substantial plastic flow during electrochemical cycling [55, 56]. Formation of voids in lithiated silicon during electrochemical cycling has been experimentally observed [10, 131, 132]. Choi et al. [131] have experimentally demonstrated that "nanopores" may form during extraction of lithium from silicon nanowires. During tensile testing of lithiated Si nanowires, Kushima et al. [124] have also observed void formation in the Si nanowire under tensile stress. Lu et al. [110] have noticed that the Si coating becomes rough and porous on the electrochemical cycling of the Si coating-Ni-CNT heterostructure.

Argon et al. [127] have suggested that voids may nucleate under the influence of combined effective stress σ_e and tensile hydrostatic stress σ_m. The results presented in **Section 8.3.3** indicate that this combination, i.e., $\sigma_e + \sigma_m$ exceeds 2 GPa in continuous Si thin films coated on CNT towards the final stage of Li de-alloying, see Figure 33. The average fracture strength of silicon which is being electrochemical cycled is observed to be in the range of 1.6 GPa [124]. Thus, the magnitude of combined stress $\sigma_e + \sigma_m$ may be sufficient to nucleate voids from the migration of Li atoms. Post nucleation, voids grow under the influence of stress triaxiality [129, 130]. Observe the occurrence of high stress triaxiality (~0.5) near the interface and the middle of the silicon domain in the same figure at the end of the electrochemical cycle. In the case of the Si nano-ring adhered to the CNT, the continuity of the Si coating in Si-CNT heterostructure configuration is reduced in the axial direction. This change is reflected in the reduced axial stress observed in the Si nano-ring (Figure 31 **(a)**). However, plot of combination of effective and hydrostatic stress in Figure 34 **(b)** shows that the magnitude of $\sigma_e + \sigma_m$ can exceed 1.6 GPa with attendant high stress triaxiality at $\overline{r} = 0.5$. Thus, void nucleation and growth may occur for this configuration in the mid-depth region of the active component.

For the Si-CNT heterostructure containing a particle in the shape of 1/8th of the Si nano-ring adhered to CNT, representative of the Si nano droplet configuration on CNT obtained experimentally [29, 114, 115], the mechanical constraints are further reduced by allowing the active material to expand in the circumferential direction. Even though the surface area per volume of the active material is highest in this configuration, which is expected to give a relatively higher first cycle irreversible loss due to the large surface area based SEI layer formation, this configuration shows the least magnitude of stress (Figure 32) and plastic flow. Also note that

void nucleation and growth condition does not occur anywhere within the domain, signifying possible long-term mechanical failure resistance of this configuration (Figure 35).

The heterostructured configuration consisting of 1/8th of the Si nano-ring adhered to CNT is compared to that synthesized previously in Dr. Kumta's laboratory, the details of which can be found in [29, 114, 115]. The synthesized Si-CNT heterostructure consists of multi-walled CNT decorated by ~60 nm diameter droplets of nano-crystalline / amorphous Si. The droplets are separated from each other by a defined, sufficiently spaced distance. This allows lithium alloying induced expansion of Si without interference and coalescence with the adjacent droplets. The diameter of the droplets is less than the critical diameter of Si particles (~150 nm) predicted by Liu et al. [107] below which fracture of Si particles during electrochemical cycling is averted. Furthermore, there is a noticeable geometrical similarity between the droplet configuration synthesized by Epur et al. [29] and the 1/8th of the Si nano-ring configuration considered by us here in this study. The active material volume of an individual Si droplet is ~11.4% lower than that of 1/8th of Si nano-ring considered (Figure 28 **(c)**). Also, the Si droplet geometry and the 1/8th of Si nano-ring have a similar surface area/volume ratio of ~0.1 and ~0.107 m^{-1}, respectively. Thus, the Si droplet configuration is expected to be mechanically stable.

The electrochemical cycling results shown by Epur et al. [29] show that the heterostructure with Si droplet configuration gives an initial capacity of ~ 2700 $mAhg^{-1}$ with 10% first cycle irreversible loss. The capacity fade rate was ~0.25% per cycle and a capacity ~ 2340 $mAhg^{-1}$ was retained after 20 cycles. The continuous Si film showed an initial capacity of ~ 3200 $mAhg^{-1}$ and a capacity with 10 % first cycle irreversible loss. However, a capacity of only ~1950 $mAhg^{-1}$ was retained after 20 electrochemical cycles, thus showing a higher capacity

fade rate of 1.7% per cycle (see Figure 33 (a) in the reference [29]). These results show that Si droplet configuration outperforms the Si continuous film configuration, in agreement with our findings.

8.5 CONCLUSIONS

Different Si configurations in Si-CNT heterostructured anode have been studied for its mechanical integrity during electrochemical cycling by utilizing a multiphysics framework employed in a finite element setting (see **Chapter 4.0**). It was observed that reducing the mechanical constraints on the active material reduces the ensuing stresses and the material inelastic flow; a conclusion that is not only limited to Si based nanostructured anodes. The Si-CNT heterostructured anodes for Li ion battery with continuous Si film coating configuration is prone to the formation of nano-voids which can cause active material disintegration during electrochemical cycling. Heterostructure with $1/8^{th}$ of the Si nano-ring, with the least mechanical constraint on the active component, was found to exhibit the least amount of stress, as well as plastic deformation of Si compared to other morphologies considered in this work. In addition, conditions for void nucleation were most unfavorable in this configuration. It is concluded that heterostructures with Si droplets adhered to CNT is thus expected to be mechanically stable during the operation of a Li-ion battery. The present computational study provides a mechanistic understanding of mechanical failure and attendant capacity fade of carbon nanotube based heterostructured anodes during electrochemical cycling. It is envisaged that this knowledge can be further applied to other anode geometries for the design of mechanical failure resistant electrode configurations.

9.0 CONCLUSIONS AND OUTLOOK

9.1 SUMMARY AND CONCLUSIONS

Silicon had indeed displayed the potential to be the next-generation anode material for Li-ion batteries with the high theoretical energy densities unmatched to that of the hitherto used carbon in commercial Li-ion batteries. However, the mechanical degradation of Si based electrodes during electrochemical cycling has proven to be the primary obstacle in the commercialization of Si based anodes. This dissertation thesis focuses on fracture mechanics based understanding of the mechanisms behind the mechanical degradation leading to loss of electrochemical capacity in Si based electrodes. Accordingly, state of the art computational methods were utilized towards that purpose.

A novel thermodynamically consistent multi-physics modeling framework was utilized to study the Li diffusion induced expansion of active material and the resulting mechanical degradation of the intercalation/alloying based electrodes. The well-known Butler-Volmer equation was used to model the surface charge transfer kinetics. Li intercalation/alloying induced large expansion and the elasto-plastic deformation of the active/passive material were modeled to evaluate the stress response of the electrode structure. Mechanical failure by interface delamination or bulk fracture of the material was simulated using the cohesive element method. Modified Mclean-Langmuir segregation kinetics was used to model the Li segregation induced

embrittlement of the Si-Cu interface properties. The modeling framework was implemented using the finite element method and verified against theoretical solutions for Li concentration evolution as well as attendant diffusion induced stress (DIS) during galvanostatic and potentiostatic electrochemical cycling.

The above mentioned modeling framework was first used to predict the voltage-capacity performance of the Si thin film anode. The open circuit potential of Si thin film anode was obtained by experiments. Reasonable agreement was observed between the capacities predicted by simulations and those obtained experimentally. Next, the effect of passive components, i.e., the current collector and Si film-current collector interface on mechanical integrity of the *a*-Si thin film anode during its electrochemical cycling was analyzed. Significant influence of the mechanical properties (elastic modulus and yield strength) of the current collector on the stress assisted delamination of the *a*-Si thin film was demonstrated. Results showed that utilization of a soft current collector material can alleviate the stresses generated in the *a*-Si thin film anode assembly and maintain the Si thin film-current collector interface integrity during electrochemical cycling.

Incremental delamination of Si thin film from the underlying copper current collector over multiple cycles was demonstrated through the simulations. It was shown that in the absence of interface embrittlement, crack at the Si-Cu interface propagates rapidly for first few cycles. However, the energy dissipation at the interface due to plastic deformation of the Si and Cu eventually leads to the arrest of the interfacial crack. Furthermore, the extent of interfacial delamination is increased when the interface embrittlement mechanisms are taken into account. It was shown that for certain parametric combinations, complete delamination as observed in experiments is achieved.

Building on the knowledge gained from the study of *a*-Si thin film anode, mechanical stability of the patterned *a*-Si thin film anode in the presence of a buffer layer during lithiation of the anode is explored. Effect of the buffer layer mechanical properties was studied by taking delamination of patterned *a*-Si thin film as the criteria for the anode mechanical stability. It was concluded that having a soft buffer (eg. carbon or a conductive polymer) between the pattern film and the current collector reduces the mechanical constraints on the active material and is thus beneficial for contributing to the stability of the patterned anode configuration. Apart from the properties of the thin buffer layer, the adhesion between different anode components is also important for mechanical stability of anode. Results from this study shed light on the factors that govern the stability of the patterned anode configuration with an elastic buffer layer by providing an understanding on mechanical failure mechanism of the anode.

Effect of active material configuration in Si-CNT heterostructured electrode has also been studied for its mechanical integrity during electrochemical cycling using the multi-physics computational framework. It was observed that reducing the mechanical constraints on the active material reduces the ensuing stresses and the material inelastic flow; a conclusion that is not only limited to Si based nanostructured anodes. The Si-CNT heterostructured anodes for Li ion battery with continuous Si film coating configuration is prone to the formation of nano-voids which can cause active material disintegration during electrochemical cycling. Heterostructures with $1/8^{th}$ of the Si nano-ring, with the least mechanical constraint on the active component, was found to exhibit the least magnitude of mechanical stress, as well as plastic deformation of Si compared to other morphologies considered in this work. In addition, conditions for void nucleation were most unfavorable in this configuration. It was thus concluded that heterostructures with Si droplets adhered to CNT are expected to be mechanically stable during

the operation of a Li-ion battery in line with the experimental observations. Thus, this study provides a mechanistic understanding of carbon nanotube based heterostructured anodes during electrochemical cycling.

9.2 OUTLOOK AND FUTURE WORK

In order to develop strategies to design next-generation flaw tolerant electrodes, understanding of the mechanism of mechanical degradation of Si based electrodes is of paramount importance. The material and electrochemical input parameters for the simulation of the novel electrode system can be obtained by performing a variety of characterization studies (such as XRD, SEM, TEM, X-ray tomography, Cyclic Voltammetry, GITT, AFM, etc.). Thus, integrating the experiments and the multi-physics modeling framework, in-silico electrochemical cycling experiments can be performed. As demonstrated in this thesis, the developed modeling framework can be used to understand the experimentally observed mechanisms of capacity fade. Further, before a novel electrode configuration is synthesized experimentally, the modeling framework can be used in a predictive manner to understand the mechanical integrity of the electrode configuration upon electrochemical cycling. It can be also used to understand failure mechanisms and provide regimes of safe operation. Thus providing important design suggestions to the experimentalist for electrode fabrication.

In future, some interesting studies can be performed by implementing minor additions into the modeling framework:

- As described in the modeling framework, the Li transport inside the active material is affected by the stress gradient in the active material. Thus, presence of stress in the active

material can enhance or retard Li diffusion as opposed to the uniform Fickian diffusion. As the stresses generated in the active material depend on the active material geometry as well as the mechanical constraints imposed by the accompanying passive materials, the electrode geometry and mechanical properties of its components can significantly alter the driving force for Li diffusion inside the active material. Comparison of the Li concentration and stress profiles generated in the active material by considering only Fickian diffusion and the stress coupled diffusion can be performed using the modeling framework.

- During electrochemical cycling, the electrode surface exposed to the electrolyte also undergoes severe deformation upon Li insertion. Thus, the free energy of the surface is also dependent on the current stress state and not just the concentration of reactants. As the reaction kinetics are dependent on the Gibb's free energy, the traditional Butler-Volmer equation can be modified by considering the effect of the surface stress state on the Gibb's free energy. Comparison of the voltage performance predicted by the traditional Butler-Volmer equation with its modified form can be performed. Furthermore, utilization of the modified Butler-Volmer equation may be able to improve the prediction of the electrode voltage performance.
- Prolonged electrochemical cycling causes accumulation of fatigue induced damage in the electrode assembly. Damage accumulation in the material leads to the loss of electrical contact as well as the reduction in Li diffusivity. Strain and stress based damage models are available in the literature. Implementation of such damage models in the modeling framework would allow studying the evolution of irreversible damage in the electrode assembly during electrochemical cycling. As evolution damage increases the tortuosity in

the material, its effect on electrochemical cycling performance can be studied by coupling the Li diffusivity with the state of material damage.

- Material defects, such as voids create free volume inside the active material. Furthermore, voids are created in the active material during electrochemical cycling. Presence of such defects may be beneficial in accommodating the Li diffusion-induced expansion and thus minimizing the generated stresses. On the other hand, void growth is detrimental to integrity of the material. This trade-off can be explored using the developed modeling framework, which may open new avenues to minimize the Li diffusion induced stresses and accordingly, improve the electrode mechanical integrity.

The phenomenon of Li intercalation/alloying induced expansion of active material is observed in all the anode and cathode materials (eg. carbon, aluminum, tin, lithium cobalt oxide, etc.). Thus, the modeling framework can be extended to other Li-ion battery electrode materials to understand the evolution of Li concentration, resulting mechanical stresses and the electrode mechanical integrity during electrochemical cycling. As the developed model has been implemented using the finite element method, it provides the flexibility to solve a variety of complex electrode structures for different boundary conditions. Various material parameters such as elastic modulus, fracture toughness, yield strength, diffusivity, etc. are known to be dependent on the active material state of charge. Also, many a times, material properties at the nano-scale vary significantly from the bulk material properties. Knowledge of accurate material parameters is necessary to produce trustworthy results.

One of the alternatives for the Li-ion battery that is getting attention in the past few years is Na-ion battery. In Na-ion batteries, sodium ions are cycled between anode and cathode as the

charge carriers. Na is accessible and abundant as compared to Li. Also, Na-ion batteries pose less safety and environmental challenges as compared to Li-ion battery[133]. Alloying of Na with tin (Sn), phosphorous (P) and antimony (Sb) has shown to give electrochemical capacity of ~850, ~2600 and ~600 mAh/g, respectively. However, upon Na insertion, the active material similar to the Li-Si case studied here in this dissertation undergoes large volumetric expansion (Sn: 423%, P:292% and Sb:293%)[134]. It leads to mechanical degradation of the electrode making it unfit for electrochemical cycling. This issue is similar to that observed in Si based electrodes for Li-ion battery. Thus, the current modeling framework can be extended to analyze electrodes for Na-ion batteries without any modification as long as the accurate material properties are known. These studies can be very well implemented in the future.

APPENDIX A

OPERATOR SPLIT TECHNIQUE

Our goal is to determine the concentration of lithium $c(\mathbf{X},t)$ in the host material and resulting displacement $\mathbf{u}(\mathbf{X},t)$ of the host material point $\mathbf{X}$ at a given time t. In the present approach, the intercalation of lithium is solved at the first stage assuming that the domain is held fixed at mechanical equilibrium. In the second stage, mechanical equilibrium is solved assuming no intercalation of lithium in the domain. The governing equations are summarized as

Stage I: Intercalation of lithium in electrode

$$\begin{aligned} &\partial_t c = \nabla D\left[\nabla c + \frac{c}{RT}\nabla\left(\frac{\partial \Psi_1}{\partial c}\right) - \frac{\eta c}{RT}\nabla p\right], \\ &\dot{\mathbf{u}} = \mathbf{0} \end{aligned} \tag{A1}$$

Stage II: Mechanical deformation of electrode and current collector

$$\begin{aligned} &\nabla \cdot \mathbf{P} = \mathbf{0} \\ &\dot{c} = 0 \end{aligned} \tag{A2}$$

APPENDIX B

VARIATIONAL FORM AND LINEARIZATION

As mentioned above, a finite element framework has been adopted to simulate the coupled processes. The variational form of the coupled Equations (4.23) is constructed through the weighted Galerkin method as

$$\begin{aligned}&\int_{\Omega_0} \delta c\, \partial_t c\, \partial\Theta + \int_{\Omega_0} \nabla\delta c D \nabla c\, \partial\Theta - \int_{\Omega_0} \nabla\delta c \frac{D\eta c}{RT} \nabla p\, \partial\Theta \\ &+ \int_{\Omega_0} \nabla\delta c \frac{Dc}{RT} \nabla\left(\frac{\partial \Psi_1}{\partial c}\right) \partial\Theta - \int_{\partial\Omega_0} \delta c J_n\, \partial\Gamma = 0\end{aligned} \tag{B1}$$

for any admissible variation δc. Furthermore, for any admissible displacement field $\delta\mathbf{u}$, the principle of virtual work states that

$$\int_{\Omega_0} \mathbf{S} : \delta\mathbf{E}\, \partial\Theta + \int_{\Gamma_c} \mathbf{t}_c \cdot \delta\boldsymbol{\delta}\, \partial\Gamma - \int_{\partial\Omega_0} \mathbf{t} \cdot \delta\mathbf{u}\, \partial\Gamma = \mathbf{0} \tag{B2}$$

To solve the variational form of lithium intercalation (B1) and principle of virtual work (B2), reference domain Ω_0 is discretized into n_{el} elements Ω_{0e}. Similar interpolation functions are assumed for the concentration of lithium and displacement field of the anode. Taking n_p as the number of nodes for a given element Ω_{0e}, the concentration of lithium atom within an

element $\tilde{c}$ can be approximated as $\tilde{c} = \sum_{i=1}^{n_p} N_c^i \bar{c}_i = \mathbf{N}_c \bar{c}$ where $\mathbf{N}_c$ is the nodal shape function matrix. The displacement field $\tilde{\boldsymbol{u}}$ of the anode within an element is approximated in a similar fashion as $\tilde{\mathbf{u}} = \sum_{i=1}^{n_p} N_u^i \bar{u}_i = \mathbf{N}_c \bar{\mathbf{u}}$ where $\mathbf{N}_u$ is the nodal shape function matrix for the displacement. To discretize the intercalation of lithium atom in time, the time interval of t is partitioned in to n_s subintervals. The intercalation of lithium atom in anode between $\left[t_n, t_{n+1}\right]$ is tracked using a backward Euler scheme with a time step size of $\Delta t = t_{n+1} - t_n$ while the material time derivative is evaluated using $\dot{c} = \left(c_{n+1} - c_n\right)/\Delta t$. The residual equations are obtained by substituting the discrete form of concentration of lithium atom $\tilde{c}$ in the variational form of intercalation (Equation (B1)) as

$$R_c = \int_{\Omega_0} \delta\tilde{c} \left\{ \frac{\tilde{c}^{n+1} - \tilde{c}^n}{\Delta t} \right\} \partial\Theta + \int_{\Omega_0} \nabla \delta\tilde{c} D \nabla \tilde{c}^{n+1} \partial\Theta - \int_{\Omega_0} \nabla \delta\tilde{c} \frac{D\eta\tilde{c}^{n+1}}{RT} \nabla p^{n+1} \partial\Theta$$
$$+ \int_{\Omega_0} \nabla\delta\tilde{c} \frac{D\tilde{c}^{n+1}}{RT} \nabla \left(\frac{\partial \Psi_1}{\partial c} \right)^{n+1} \partial\Theta - \int_{\partial\Omega_0} \delta\tilde{c} J^{n+1} \partial\Theta = 0 \tag{B3}$$

Similarly, substituting discrete form of displacement field $\tilde{\mathbf{u}}$ in principle of virtual work (Equation (B2)), the residual for the second stage can be expressed as

$$R_u = \int_{\Omega_0} \mathbf{S} : \delta\tilde{\mathbf{E}} \partial\Theta + \int_{\Gamma_c} \mathbf{t}_c \cdot \delta\tilde{\boldsymbol{\delta}} \partial\Gamma - \int_{\partial\Omega_0} \mathbf{t} \cdot \delta\tilde{\mathbf{u}} \partial\Gamma = 0 \tag{B4}$$

A Newton-Raphson scheme is adopted here to solve the residual Equations (B3) and (B4) through consistent linearization. Therefore, the set of linearized residual equations are written as

$$\frac{\partial R_c}{\partial \tilde{c}^{n+1}} \Delta\tilde{c}_{n+1}^{k+1} = -R_c^k \tag{B5.1}$$

$$\frac{\partial R_u}{\partial \tilde{\mathbf{u}}^{n+1}} \Delta\tilde{\mathbf{u}}_{n+1}^{k+1} = -R_u^k \tag{B5.2}$$

Substituting $\tilde{c} = \mathbf{N}_c \overline{c}$ in (B5.1) yields

$$\mathbf{K_c} \nabla \overline{\mathbf{c}}_{\mathbf{k+1}}^{n+1} = \mathbf{R_c^k} \tag{B6}$$

where, $\mathbf{K_c} = \mathbf{K_{c1}} + \mathbf{K_{c2}} + \mathbf{K_{c3}} + \mathbf{K_{c4}}$ and

$$\mathbf{K_{c1}} = \sum_{e=1}^{n_{el}} \int_{\Omega_0^e} \frac{\mathbf{N}_\mathrm{c}^\mathrm{T} \mathbf{N}_\mathrm{c}}{\Delta t} \, \partial\Theta \tag{B7.1}$$

$$\mathbf{K_{c2}} = \sum_{e=1}^{n_{el}} \int_{\Omega_0^e} \mathbf{B}_\mathrm{c}^\mathrm{T} D \mathbf{B}_\mathrm{c} \, \partial\Theta \tag{B7.2}$$

$$\mathbf{K_{c3}} = \sum_{e=1}^{n_{el}} \int_{\Omega_0^e} \mathbf{B}_\mathrm{c}^\mathrm{T} \frac{D\eta}{RT} \nabla p_k^{n+1} \mathbf{N}_\mathrm{c} \, \partial\Theta \tag{B7.3}$$

$$\mathbf{K_{c4}} = \sum_{e=1}^{n_{el}} \int_{\Omega_0^e} \mathbf{B}_\mathrm{c}^\mathrm{T} \frac{D\eta \, c_k^{n+1}}{RT} \nabla \left(\frac{\partial p^{n+1}}{\partial c^{n+1}} \right)_k \partial\Theta \tag{B7.4}$$

Also, $\mathbf{R_c} = \mathbf{R_{c1}} + \mathbf{R_{c2}} + \mathbf{R_{c3}} + \mathbf{R_{c4}}$ and

$$\mathbf{R_{c1}} = \sum_{e=1}^{n_{el}} \int_{\partial\Omega_0^e} \mathbf{N}_\mathrm{c}^\mathrm{T} J_0^{n+1} \, \partial\Theta \tag{B8.1}$$

$$\mathbf{R_{c2}} = \sum_{e=1}^{n_{el}} \int_{\Omega_0^e} \mathbf{N}_\mathrm{c}^\mathrm{T} \mathbf{N}_\mathrm{c} \, \partial\Theta \left\{ \frac{\overline{c}_k^{n+1} - \overline{c}^n}{\Delta t} \right\} \tag{B8.2}$$

$$\mathbf{R_{c3}} = \sum_{e=1}^{n_{el}} \int_{\Omega_0^e} \mathbf{B}_\mathrm{c}^\mathrm{T} D \mathbf{B}_\mathrm{c} \, \partial\Theta \, \overline{c}_k^{n+1} \tag{B8.3}$$

$$\mathbf{R_{c4}} = \sum_{e=1}^{n_{el}} \int_{\Omega_0^e} \mathbf{B}_\mathrm{c}^\mathrm{T} \frac{D\eta}{RT} \nabla p_k^{n+1} \, \mathbf{N}_\mathrm{c} \, \partial\Theta \, \overline{c}_k^{n+1} \tag{B8.4}$$

Similarly, linearization of residual equation of principal of virtual work (Equation (B5.2)) yields

$$\mathbf{K}_u \nabla \bar{\mathbf{u}}_{\mathrm{k+1}}^{n+1} = \mathbf{R}_u^{\mathbf{k}} \tag{B9}$$

Where, stiffness matrix $\mathbf{K_u}$ and load vector $\mathbf{R_u^k}$ can be written as

$$\mathbf{K}_u = \sum_{e=1}^{n_{el}} \int_{\Omega_0^e} \mathbf{B}_u^{\mathrm{T}} \mathbf{L} \mathbf{B}_u \, \partial\Theta + \sum_{e=1}^{n_{el}} \int_{\Omega_0^e} \mathbf{B}_0^{\mathrm{T}} \mathbf{S} \mathbf{B}_0 \mathbf{I} \, \partial\Theta \tag{B10.1}$$

$$\mathbf{R}_u = \sum_{e=1}^{n_{el}} \int_{\partial\Omega_0^e} \mathbf{N}_u^{\mathrm{T}} \mathbf{t} \, \partial\Gamma - \sum_{e=1}^{n_{el}} \int_{\Omega_0^e} \mathbf{B}_u^{\mathrm{T}} \mathbf{S} \, \partial\Theta \tag{B10.2}$$

where $\mathbf{B_u}$ and $\mathbf{B_0}$ given as

$$\mathbf{B_u} = sym(\nabla \mathbf{N_u F}) \text{, and } \mathbf{B}_0 = \nabla \mathbf{B}_u, \tag{B11}$$

respectively. The fourth order tensor $\mathbf{L}$ represents the Lagrangian constitutive moduli which can be derived directly from the linearization of second Piola Kirchhoff stress $\mathbf{S}$ with respect to total Cauchy green tensor $\mathbf{C}$ for a fixed $\mathbf{F}_\theta$ as

$$\mathbf{L} = 2\frac{\partial \mathbf{S}}{\partial \mathbf{C}} = [\mathbf{F}_\theta^{-1} \otimes \mathbf{F}_\theta^{-1}] : \mathbf{L}_e : [\mathbf{F}_\theta^{-T} \otimes \mathbf{F}_\theta^{-T}] \tag{B12}$$

The above equation can be interpreted as the pull back of the elastic moduli $\mathbf{L_e}$ onto the reference configuration, where $\mathbf{L_e} = 2\partial \mathbf{S_e} / \partial \mathbf{C_e}$ are the constitutive moduli of the elastic material.

APPENDIX C

SOLUTION STRATEGY

An iterative strategy has been adopted to solve the discretized equation for lithium intercalation and mechanical equilibrium of anode at each time step. Let $\left(\bullet\right)_k^n$ denote the value at iteration level k within time step n, while $\left(\bullet\right)^n$ denote converged value at time step t_n. Our goal is to obtain the converged concentration and displacement field at $n+1$ assuming all the field quantities are known at $t = t_n$.

1. Increment time t_n by Δt i.e., set $t_{n+1} = t_n + \Delta t$

2. Start iteration with $k = 0$ and $\left(\bullet\right)_0^{n+1} = \left(\bullet\right)^n$

   (a) If $k = 0$, set $\overline{\mathbf{u}}_0^{n+1} = \overline{\mathbf{u}}^n$ and find $\overline{c}_{n+1}^{k+1}$ from Equation (B6)

   (b) Compute $\overline{\mathbf{u}}_{k+1}^{n+1}$ from Equation (B9) using $\overline{c}_{n+1}^{k+1}$

   (c) Check the convergence criteria

$$\frac{\left\|\overline{c}_{n+1}^{k+1} - \overline{c}_{n+1}^{k}\right\|_2}{\left\|\overline{c}_{n+1}^{0}\right\|_2} \le \varepsilon_c \quad \text{and} \quad \frac{\left\|\overline{\mathbf{u}}_{k+1}^{n+1} - \overline{\mathbf{u}}_{k}^{n+1}\right\|_2}{\left\|\overline{\mathbf{u}}_{0}^{n+1}\right\|_2} \le \varepsilon_u$$

   then repeat step 1 else set $k = k+1$ and go to step 2(a).

APPENDIX D

VERIFICATION OF THE MODELING FRAMEWORK

The modeling framework detailed in **Chapter 4.0** is verified against theoretical results. For this purpose, a spherical graphite particle of $R = 1\,\mu m$ radius is considered. The particle is lithiated to its complete capacity (372 $mAhg^{-1}$) under potentiostatic and galvanostatic conditions. Due to the symmetry of the spherical particle, only $1/8^{th}$ of the spherical volume is taken for the finite element simulation. The domain is meshed with 7000 '8 noded' hexahedral elements and contains 7951 nodes (Figure 36). The material constants considered for the simulations are given in Table D1. Graphite is assumed to be a linear elastic material. The generated concentration and stress profiles are compared against the analytical solutions available for diffusion induced stress (DIS) for a spherical particle in literature[43]. It should be noted that since the analytical solutions neglect the effect of mechanical stress on the Li transport, only Fickian diffusion is considered for the FE simulations.

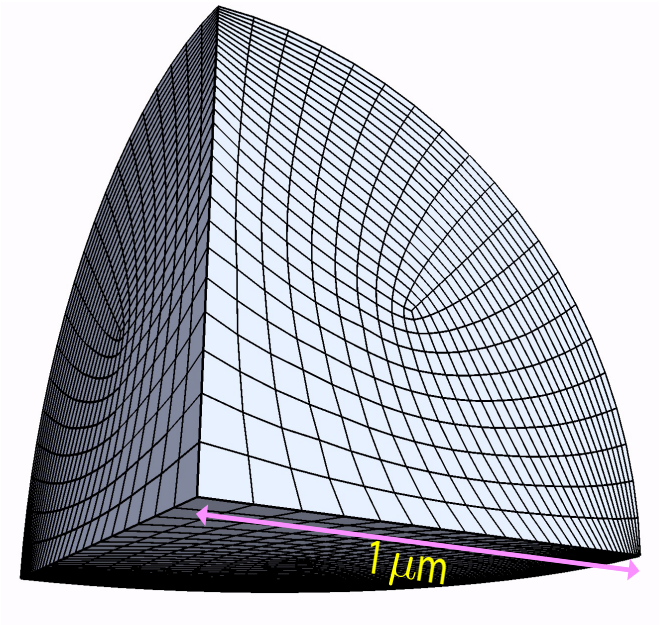

Figure 36. Finite element mesh of 1/8th of the spherical graphite particle with 1 μm radius.

Table 4. Material parameters for simulation of graphite particle

Young's modulus (E)	10 GPa
Poisson's ratio (ν)	0.28
Li diffusivity (D)	10^{-12} m^2s^{-1}
Maximum Li concentration inside graphite (c_{max})	3.2340×10^4 mol m^{-3}
Partial molar volume of Li in graphite (Ω)	2.88×10^{-6} m^3 mol^{-1}
Faraday's constant (F)	96485.34 C mol^{-1}
Universal gas constant (R)	8.314 J K^{-1} mol^{-1}

D.1 POTENTIOSTATIC OPERATION

For the potentiostatic lithiation of graphite particle of radius R, the boundary conditions are taken as $c(r,0)=0$ for $0 \le r \le R$ and, $c(R,t)=c_{max}$ for $t \ge 0$.

The analytical solution for Li concentration distribution inside the particle is given as

$$\frac{c(r,t)}{c_{max}} = 1 + \sum_{n=1}^{\infty} \frac{-1^n}{n\pi(r/R)} \sin(n\pi(r/R)) e^{-n^2\pi^2\tau} \tag{D1}$$

where, the normalized time $\bar{\tau}$ is obtained as $\bar{\tau} = tD/R^2$. The corresponding normalized radial and circumferential stress profiles are given as

$$\bar{\sigma}_r = -4\sum_{n=1}^{\infty} \exp(n^2\pi^2\tau)\left(\frac{1}{(n\pi)^2} + (-1)^n\left(\frac{\sin(n\pi x) - n\pi x\cos(n\pi x)}{(n\pi x)^3}\right)\right) \tag{D2}$$

$$\bar{\sigma}_\theta = -2\sum_{n=1}^{\infty} \exp(-n^2\pi^2\tau) \left(\frac{2}{(n\pi)^2} + \frac{(-1)^n}{n\pi x}\sin(n\pi x) - (-1)^n\left(\frac{\sin(n\pi x) - n\pi x\cos(n\pi x)}{(n\pi x)^3}\right)\right) \tag{D3}$$

where the stresses are normalized with a stress like quantity $E\Omega(c_{max})/3(1-\nu)$.

Figure 37 **(a-c)** show the comparison of the analytical (dotted line) and the FE simulation results of Li concentration and stress profile at different τ. Again, the simulation results match closely with the analytical solutions. The peak stress predicted by simulations are almost similar with about ~4% difference in magnitude.

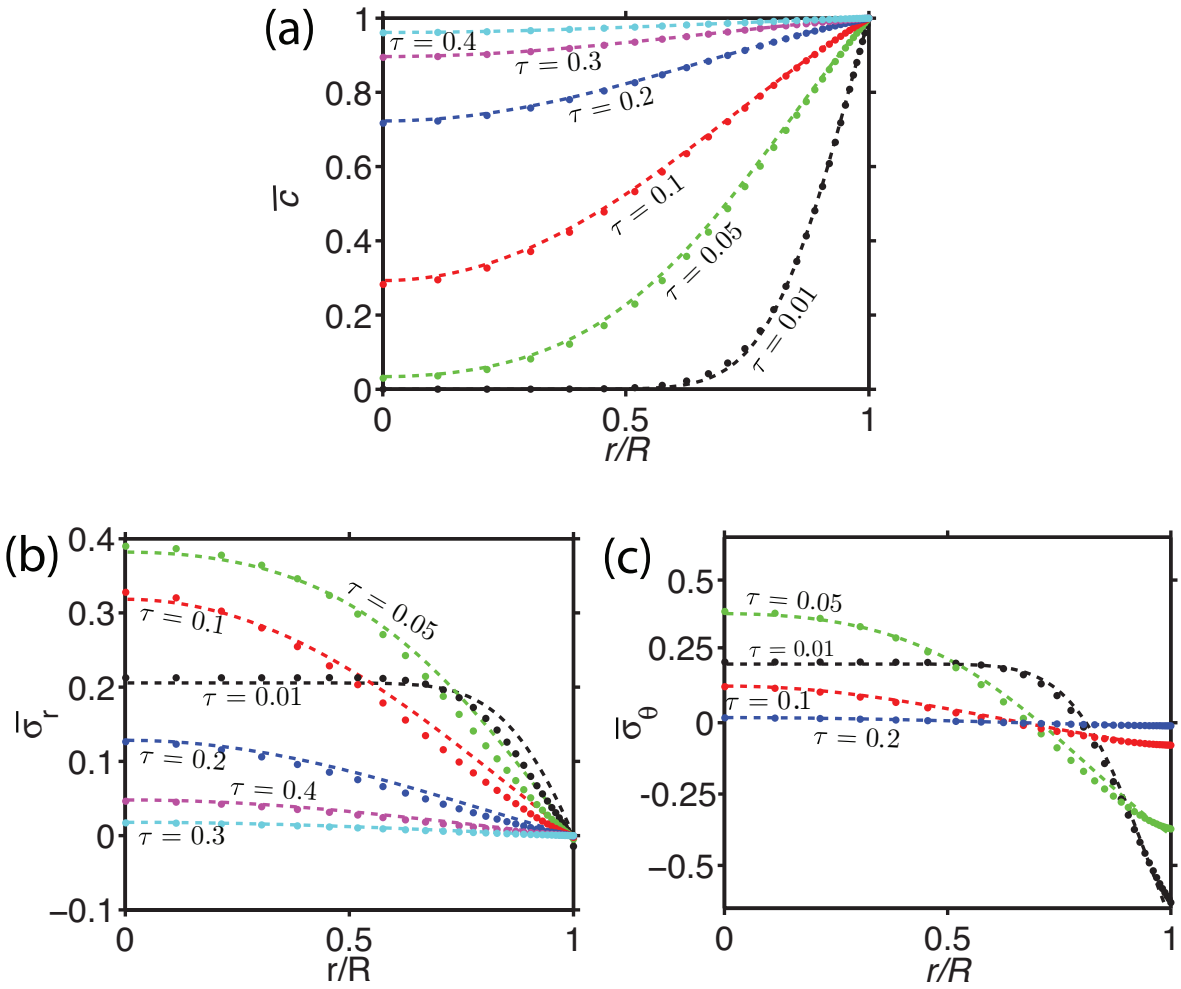

Figure 37. Comparison of normalized (a) concentration profiles, (b) radial stress profiles and (c) circumferential stress profiles for potentiostatic loading of graphite spherical particle (points- finite element simulation dotted line- analytical solution[43]).

D.2 GALVANOSTATIC OPERATION

For galvanostatic lithiation, a constant Li flux corresponding to 8C charge rate is applied to the particle surface. The boundary conditions are, $c(r,0)=0$ for $0 \le r \le R$ and $\mathbf{J}\cdot\mathbf{N} = J_{Li} = \dfrac{Cm}{At}$ on $r = R$ (see **Section 4.1** for details).

The analytical solution for Li concentration distribution inside the particle is given as

$$\frac{c(r,t)}{c_{max}} = \frac{IR}{FDc_{max}}\left[3\tau + \frac{1}{2}(r/R)^2 - \frac{3}{10} - \frac{2}{(r/R)}\sum_{n=1}^{\infty}\left(\frac{\sin(\lambda_n(r/R))}{\lambda_n^2\sin(\lambda_n)}\exp(-\lambda_n^2\tau)\right)\right] \tag{D4}$$

The corresponding normalized radial and circumferential stresses are given by

$$\bar{\sigma}_r(r,t) = \frac{1}{5}(1-(r/R)^2) + \frac{4}{(r/R)^4}\sum_{n=1}^{\infty}\left(\frac{\sin(\lambda_n(r/R)) - (\lambda_n(r/R)\cos(\lambda_n(r/R))}{\lambda_n^4\sin(\lambda_n)}\exp(-\lambda_n^2\tau)\right) \tag{D5}$$

$$\bar{\sigma}_\theta(r,t) = \frac{1}{5}(1-2(r/R)^2) + 2\sum_{n=1}^{\infty}\frac{\exp(-\lambda_n^2\tau)}{\lambda_n\sin(\lambda_n)} \times \left(\frac{\sin(\lambda_n(r/R))}{\lambda_n(r/R)} - \frac{\sin(\lambda_n(r/R)) - (\lambda_n(r/R)\cos(\lambda_n(r/R))}{\lambda_n^3(r/R)^3}\right) \tag{D6}$$

where the normalization factor is $2E\Omega/3(1-\nu)(J_{Li}R/D)$.

Figure 38 **(a-c)** shows the comparison of the analytical (dotted line) and the FE simulation results of Li concentration and stress profile at different τ. As it can be seen from these graphs, the analytical solution and the simulation results are in significant agreement with each other. Thus, the presented framework can be used to analyze Li diffusion induced stresses in electrode materials.

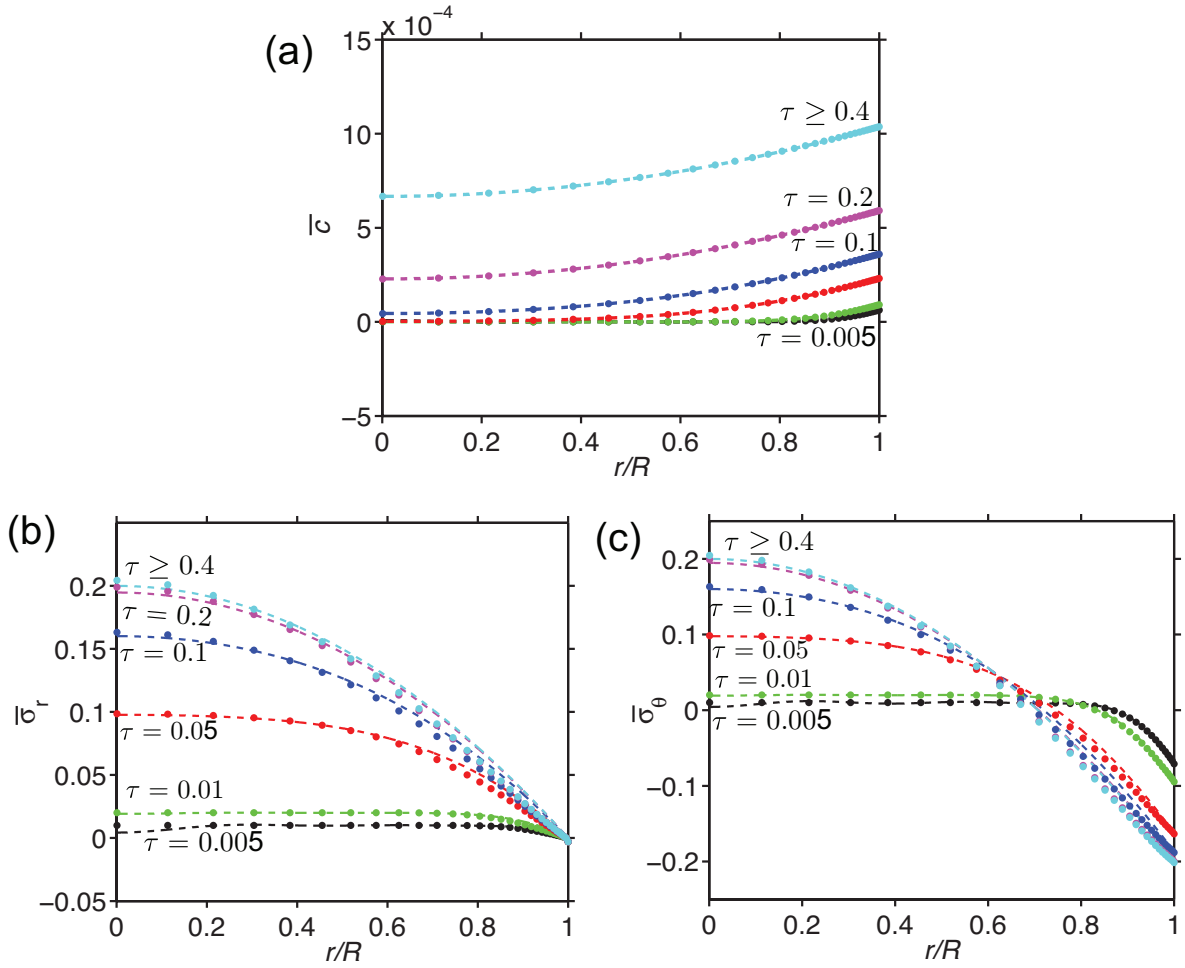

Figure 38. Comparison of normalized (a) concentration profiles, (b) radial stress profiles and (c) circumferential stress profiles for galvanostatic loading of graphite spherical particle (points- finite element simulation dotted line- analytical solution[43]).

APPENDIX E

OPEN CIRCUIT POTENTIAL OF 250 NM THICK *A*-SI THIN FILM ANODE

Prediction of the half-cell potential requires an accurate estimation of the open circuit voltage $U_{OCP}(\text{soc})$. However, these parameters depend on the mechanical configuration as well as the material properties of the anode. Thus GITT (Galvanostatic Intermittent Titration Technique) experiments are performed for estimating the $U_{OCP}(\text{soc})$ for a 250 nm thick *a*-Si thin films deposited on a Cu substrate[135]. The 250 nm thick film of *a*-Si was prepared by radio frequency (RF) magnetron sputtering. The details of the deposition conditions and the fabrication of the 2016 coin cells for electrochemical testing can be found in a previous publication[19]. Prior to GITT, the half-cell was cycled at $C/4$ current rate for 5 charge/discharge cycles to ensure the formation of the (solid-electrolyte interface) SEI layer. For the GITT, galvanostatic lithiation of the fully discharged *a*-Si anode was carried out in repeated segments of 1 hr at $C/25$ rate followed by a relaxation period of 10 hr to ensure equilibration. The cut-off voltage was set to 0.02 V vs. Li/Li^+ electrode. Similar process for delithiation of the fully lithiatiated anode was carried out and the cut off voltage was set to 1.2 V vs. the Li/Li^+ electrode. The $U_{OCP}(\text{soc})$ data obtained from the GITT experiment was fitted as a function of state of charge (soc) using cubic splines (Figure 39) and is used for all the Si thin film simulations performed for this study.

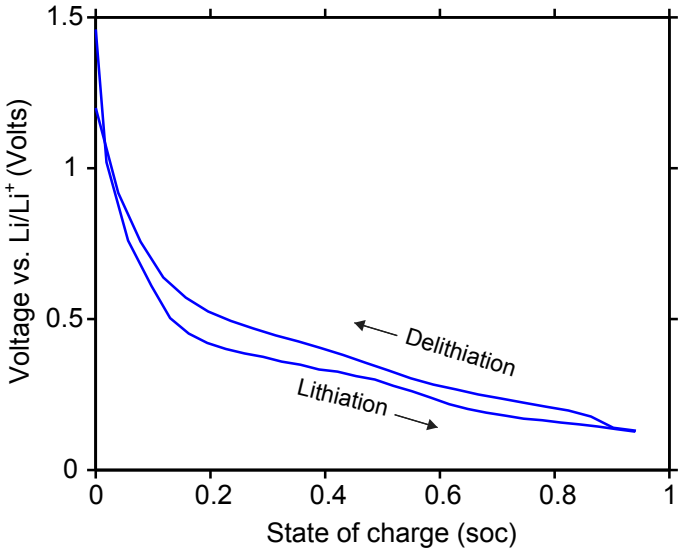

Figure 39. Open circuit potential for lithiation and delithiation of 250 nm *a*-Si thin film electrode obtained by Galvanostatic Intermittent Titration Technique (GITT).

APPENDIX F

EFFECT OF SI CONFIGURATION DIMENSION ON LI CONCENTRATION PROFILE AND ATTENDANT STRESSES IN DIFFERENT SI-CNT HETEROSTRUCTURED CONFIGURATIONS

Detailed simulations to study the effect of dimensions of active material (Si) on the evolution of Li concentration profile and attendant stresses in the three different Si-CNT heterostructure geometries considered in **Chapter 0**are reported here. The dimensions of the CNT (radius 40 nm) and the Li diffusivity in Si (D_o=10^{-18} m^2/s) are kept constant for all the simulations.

Figure 40 (a-c) shows the evolution of Li concentration ($c_{Li} / c_{Li\max}$) at different normalized times during the lithium alloying half-cycle ($\tau = 0$ to 0.5) for three coating thicknesses (25 nm, 50 nm and 100 nm) for Configuration I. The profiles are shown along the longitudinal (LONG) section (XZ plane) of the Si film coating. This figure reveals that increasing the Si coating thickness increases the concentration gradient in Si coating. As it can be seen from Figure 40 (a), for the 25 nm Si coating thickness, the difference in $c_{Li} / c_{Li\max}$ at the outside surface of Si exposed to the electrolyte and the inside surface adhered to the CNT does

not exceed 0.10 at any time instant. For the case of 100 nm Si coating thickness (Figure 40 (c)), the maximum difference in $c_{Li} / c_{Li\max}$ at outside and inside surface of Si is found to be ~0.74.

Similarly, the evolution of $c_{Li} / c_{Li\max}$ in Si nano-ring of Configuration II and the 1/8th of the Si nano-ring of Configuration III is shown in Figure 41 and Figure 42, respectively. The radial and axial thickness of the Si nano-ring is varied as 25, 50 and 100 nm. Again, it can be seen from Figure 41 and Figure 42 that increasing the size of the active material increase the concentration gradient in Si configuration. Additionally, as mentioned in **Section 8.4**, the ratio of surface area exposed to electrolyte to the active material volume is highest in Configuration III and least in Configuration I. As a result, the extent of concentration gradient developed inside the active material is different for different Si-CNT heterostructures. For example, for the Si nano-ring thickness of 100 nm, the maximum difference in $c_{Li} / c_{Li\max}$ at any time instant for Configuration II is ~0.61 (Figure 41 (c)), while for Configuration III it is ~0.41 (Figure 42 (c)).

In Figure 43, the attendant effective stresses (σ_e) in the active material of the three Si-CNT heterostructures are shown for different Si thickness at the end of lithium alloying half-cycle ($\tau = 0.5$). Figure 43 (a-c) shows that increasing Si thickness from 25 nm to 50 nm does not change the effective stresses significantly. However, upon increasing the Si coating thickness to 100 nm, significant amount of effective stresses are developed near the outer surface of Si coating exposed to the electrolyte. Similar observation was recorded for Configurations II and III. Figure 43 (d-f) and (g-i) show that increasing the Si nano-ring thickness from 25 nm to 50 nm does not change the incurred effective stresses significantly in the Si nano-ring, as well as in the particle in shape of 1/8th of Si nano-ring. However, increasing the nano-ring thickness to 100 nm increases the incurred stresses. Thus, the mechanical integrity of the 25 nm coating thickness

Si-CNT heterostructures can be expected to be similar to that of heterostructures with 50 nm coating thickness (discussed in detail in **Section 8.3** and **8.4**). However, increasing the Si coating thickness to 100 nm would definitely not improve the mechanical integrity of the Si-CNT configurations compared to the heterostructures with Si thickness of 50 nm.

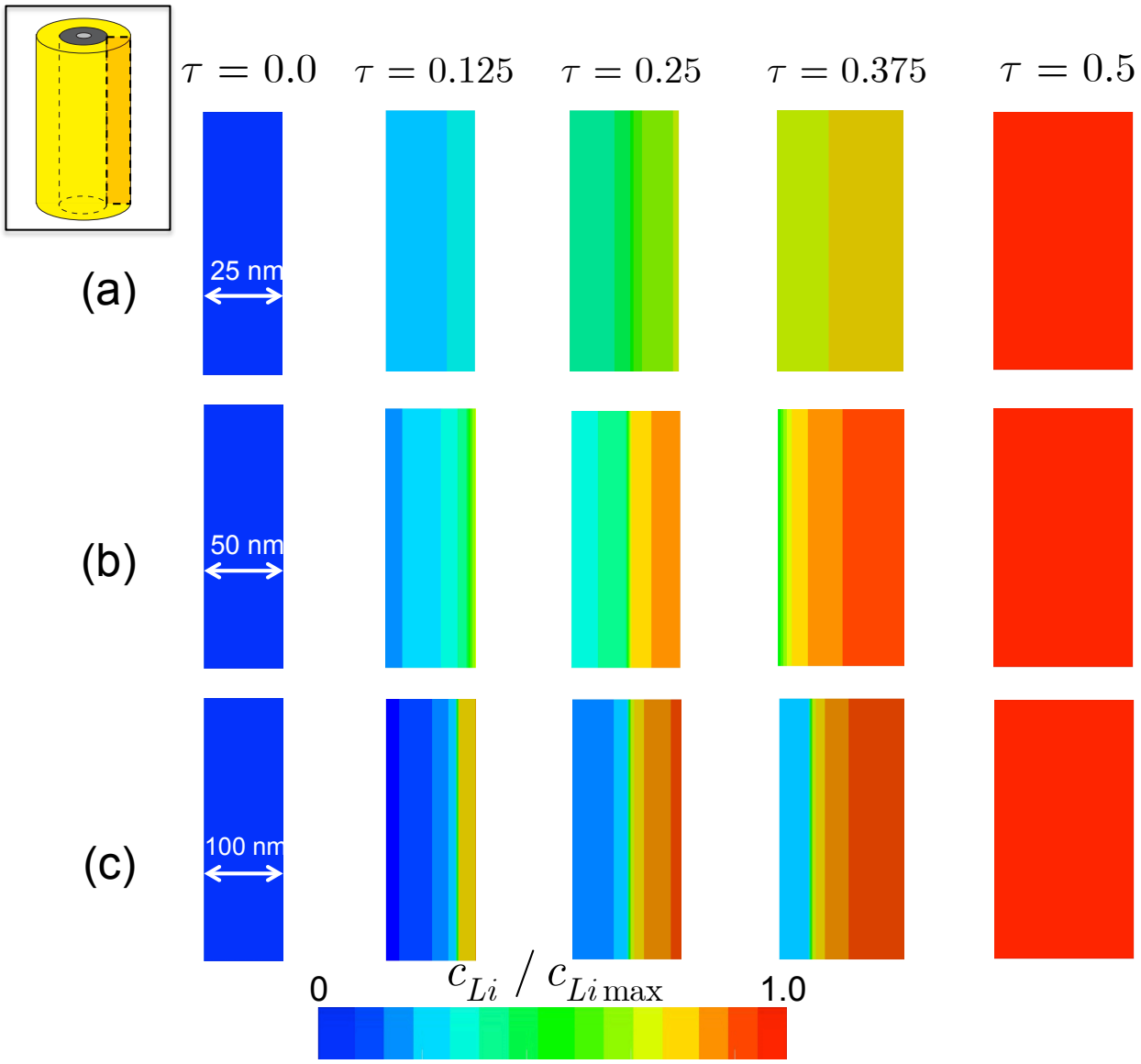

Figure 40. Evolution of normalized Li concentration ($c_{Li} \,/\, c_{Li\,\max}$) in Si during lithium alloying half-cycle along the longitudinal (LONG) section (XZ plane) of continuous Si coating of Configuration I with thickness (a) 25 nm, (b) 50 nm and (c) 100 nm. (Note that the longitudinal sections shown are not to scale).

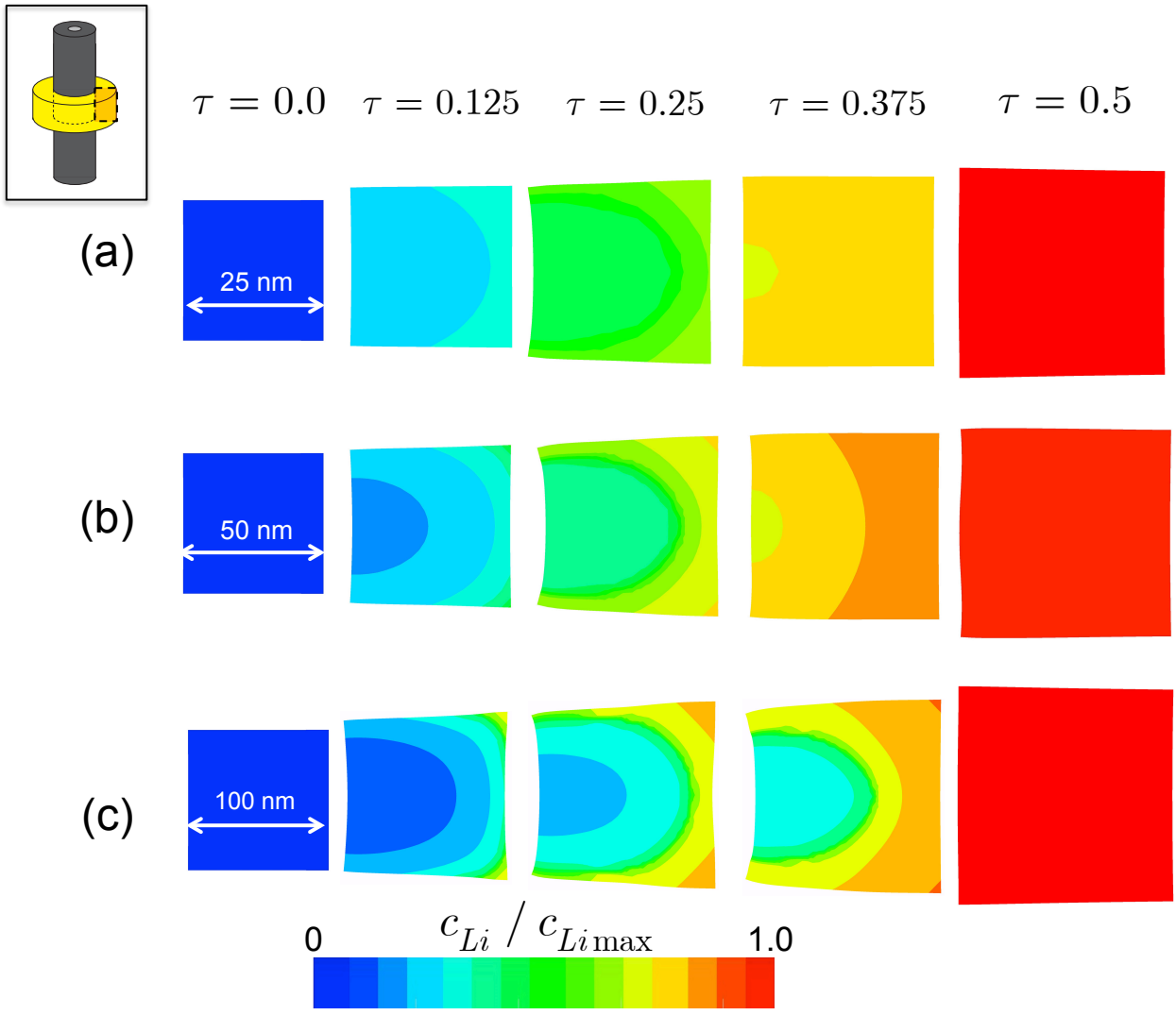

Figure 41. Evolution of normalized Li concentration ($c_{Li} \,/\, c_{Li\max}$) in Si during lithium alloying half-cycle along the longitudinal (LONG) section (XZ plane) of Si nano-ring of Configuration II with thickness (a) 25 nm, (b) 50 nm and (c) 100 nm. (Note that the longitudinal sections shown are not to scale).

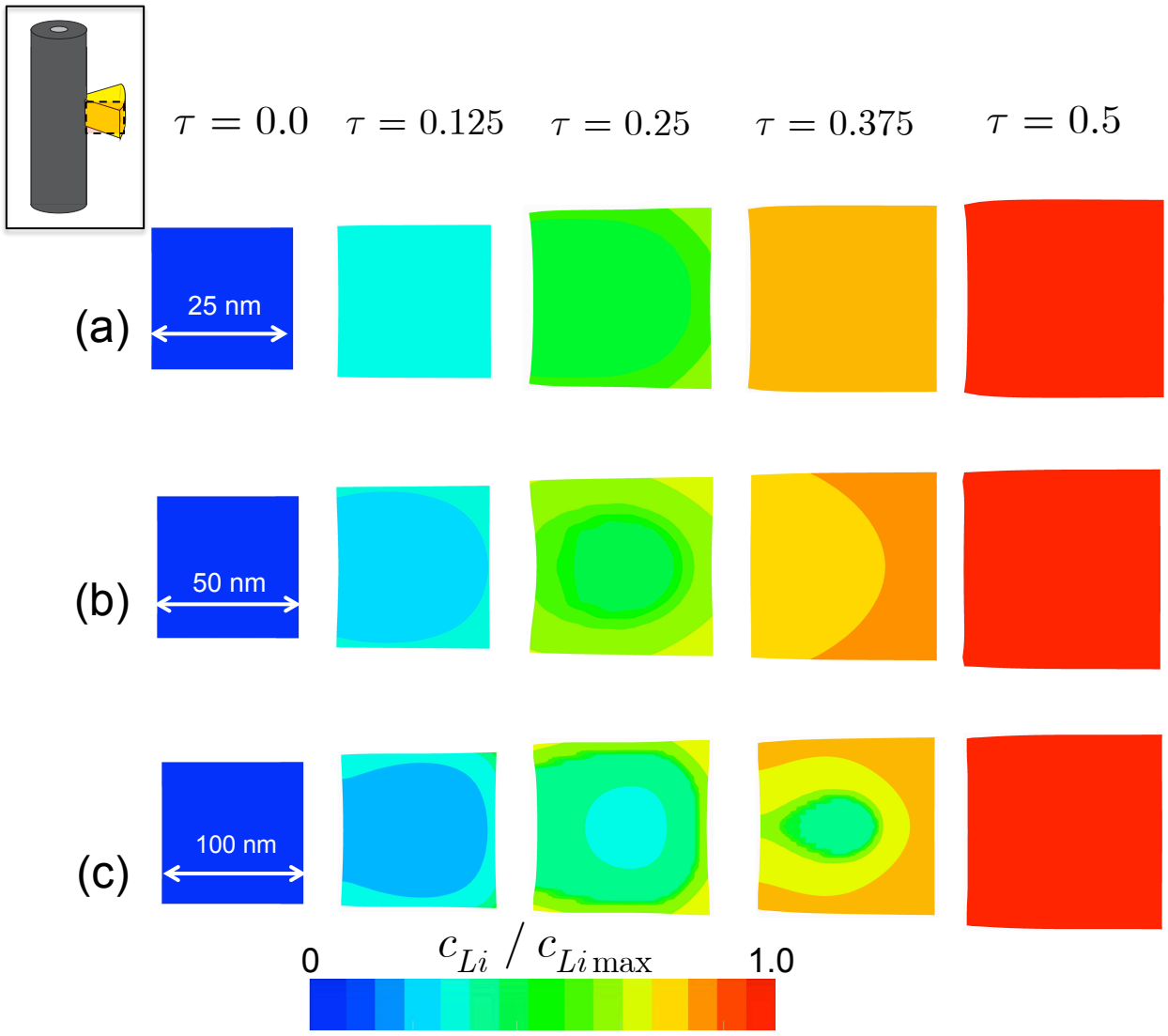

Figure 42. Evolution of normalized Li concentration ($c_{Li} / c_{Li\max}$) in Si during lithium alloying half-cycle along the longitudinal (LONG) section (XZ plane) of 1/8th of Si nano-ring of Configuration III with thickness (a) 25 nm, (b) 50 nm and (c) 100 nm. (Note that the longitudinal sections shown are not to scale).

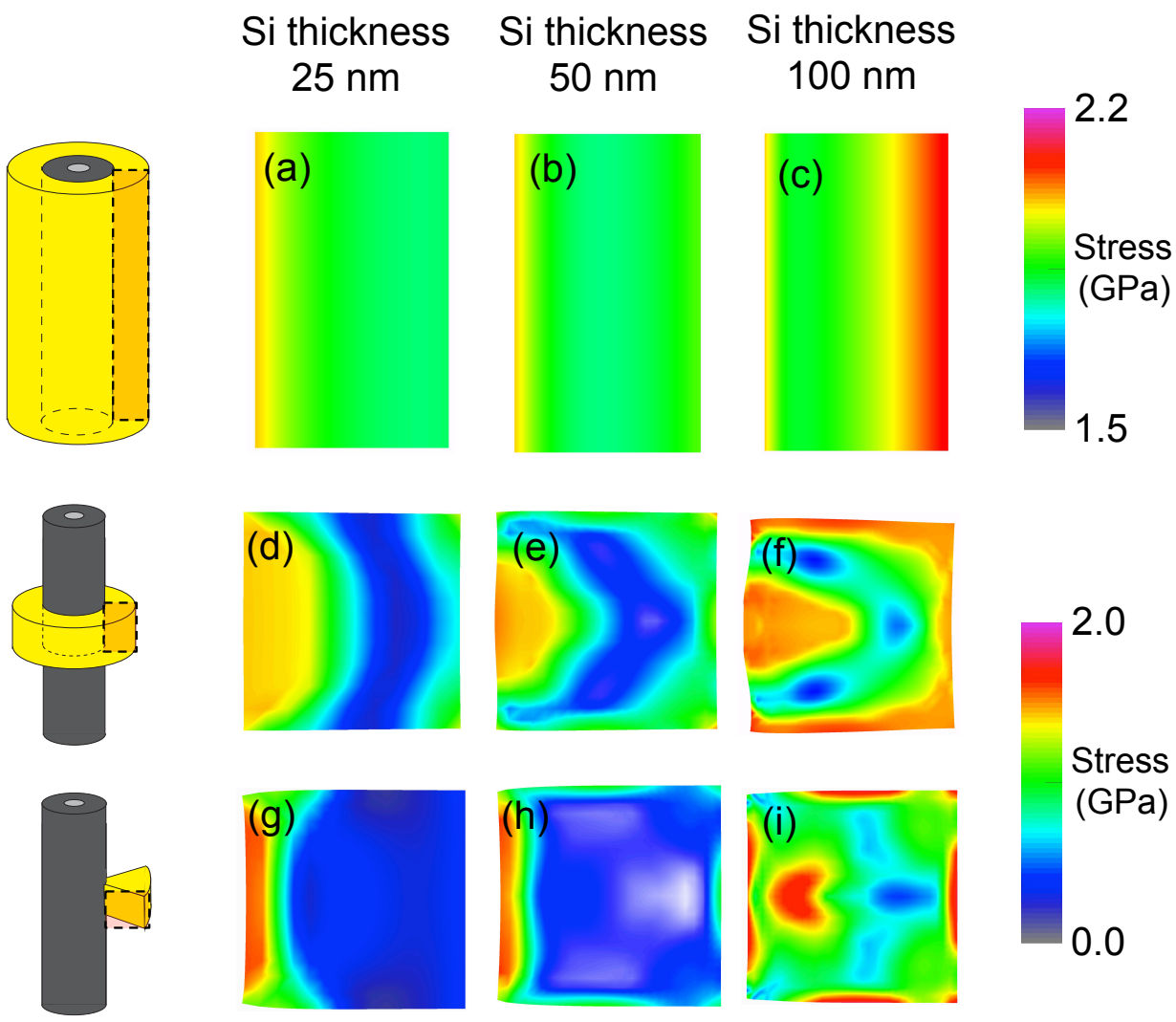

Figure 43. Effective stress in the active material along the longitudinal section (XZ plane) of three different Si-CNT heterostructure configurations for three different Si coating thicknesses. (Note that the stress scale bar for (a-c) and (d-i) is different).

BIBLIOGRAPHY

1. *Key world energy statistics*. 2014, International Energy Agency.

2. Thackeray, M.M., C. Wolverton, and E.D. Isaacs, *Electrical energy storage for transportation—approaching the limits of, and going beyond, lithium-ion batteries.* Energy & Environmental Science, 2012. **5**(7): p. 7854.

3. Tarascon, J.M. and M. Armand, *Issues and challenges facing rechargeable lithium batteries.* Nature, 2001. **414**(6861): p. 359-67.

4. Kasavajjula, U., C. Wang, and A.J. Appleby, *Nano- and bulk-silicon-based insertion anodes for lithium-ion secondary cells.* Journal of Power Sources, 2007. **163**(2): p. 1003-1039.

5. Tran, T.D., J.H. Feikert, X. Song, and K. Kinoshita, *Commercial Carbonaceous Materials as Lithium Intercalation Anodes.* Journal of the Electrochemical Society, 1995. **142**(10): p. 3297-3302.

6. Beaulieu, L.Y., K.W. Eberman, R.L. Turner, L.J. Krause, and J.R. Dahn, *Colossal Reversible Volume Changes in Lithium Alloys.* Electrochemical and Solid-State Letters, 2001. **4**(9): p. A137.

7. Colvin, E.W., J.E. Baldwin, A.D. Buckingham, and S. Danishefsky, *Silicon in Organic Synthesis*. Butterworths Monographs in Chemistry and Chemical Engineering. 1981: Butterworth-Heinemann.

8. Fu, K., O. Yildiz, H. Bhanushali, Y. Wang, K. Stano, L. Xue, X. Zhang, and P.D. Bradford, *Aligned carbon nanotube-silicon sheets: a novel nano-architecture for flexible lithium ion battery electrodes.* Adv Matererials, 2013. **25**(36): p. 5109-14.

9. Sun, C.F., K. Karki, Z. Jia, H. Liao, Y. Zhang, T. Li, Y. Qi, J. Cumings, G.W. Rubloff, and Y. Wang, *A beaded-string silicon anode.* ACS Nano, 2013. **7**(3): p. 2717-24.

10. Hu, L., H. Wu, Y. Gao, A. Cao, H. Li, J. McDough, X. Xie, M. Zhou, and Y. Cui, *Silicon-Carbon Nanotube Coaxial Sponge as Li-Ion Anodes with High Areal Capacity.* Advanced Energy Materials, 2011. **1**(4): p. 523-527.

11. Wang, C.M., X. Li, Z. Wang, W. Xu, J. Liu, F. Gao, L. Kovarik, J.G. Zhang, J. Howe, D.J. Burton, Z. Liu, X. Xiao, S. Thevuthasan, and D.R. Baer, *In situ TEM investigation of congruent phase transition and structural evolution of nanostructured silicon/carbon anode for lithium ion batteries.* Nano Lett, 2012. **12**(3): p. 1624-32.

12. Maranchi, J.P., A.F. Hepp, A.G. Evans, N.T. Nuhfer, and P.N. Kumta, *Interfacial properties of the a-Si/Cu : active-inactive thin-film anode system for lithium-ion batteries.* Journal of the Electrochemical Society, 2006. **153**(6): p. A1246-A1253.

13. Ryu, I., J.W. Choi, Y. Cui, and W.D. Nix, *Size-dependent fracture of Si nanowire battery anodes.* Journal of the Mechanics and Physics of Solids, 2011. **59**(9): p. 1717-1730.

14. Li, J., A.K. Dozier, Y. Li, F. Yang, and Y.-T. Cheng, *Crack Pattern Formation in Thin Film Lithium-Ion Battery Electrodes.* Journal of The Electrochemical Society, 2011. **158**(6): p. A689.

15. Kim, H., M. Seo, M.H. Park, and J. Cho, *A critical size of silicon nano-anodes for lithium rechargeable batteries.* Angew Chem Int Ed Engl, 2010. **49**(12): p. 2146-9.

16. Wu, H., G. Chan, J.W. Choi, I. Ryu, Y. Yao, M.T. McDowell, S.W. Lee, A. Jackson, Y. Yang, L. Hu, and Y. Cui, *Stable cycling of double-walled silicon nanotube battery anodes through solid–electrolyte interphase control.* Nature Nanotechnology, 2012. **7**: p. 310–315.

17. Chan, C.K., H. Peng, G. Liu, K. McIlwrath, X.F. Zhang, R.A. Huggins, and Y. Cui, *High-performance lithium battery anodes using silicon nanowires.* Nat Nanotechnol, 2008. **3**(1): p. 31-5.

18. Xiao, X., P. Liu, M.W. Verbrugge, H. Haftbaradaran, and H. Gao, *Improved cycling stability of silicon thin film electrodes through patterning for high energy density lithium batteries.* Journal of Power Sources, 2011. **196**(3): p. 1409-1416.

19. Maranchi, J.P., A.F. Hepp, and P.N. Kumta, *High Capacity, Reversible Silicon Thin-Film Anodes for Lithium-Ion Batteries.* Electrochemical and Solid-State Letters, 2003. **6**(9): p. A198.

20. Lee, K.-L., J.-Y. Jung, S.-W. Lee, H.-S. Moon, and J.-W. Park, *Electrochemical characteristics of a-Si thin film anode for Li-ion rechargeable batteries.* Journal of Power Sources, 2004. **129**(2): p. 270-274.

21. Datta, M.K., J. Maranchi, S.J. Chung, R. Epur, K. Kadakia, P. Jampani, and P.N. Kumta, *Amorphous silicon–carbon based nano-scale thin film anode materials for lithium ion batteries.* Electrochimica Acta, 2011. **56**(13): p. 4717-4723.

22. Yu, C., X. Li, T. Ma, J. Rong, R. Zhang, J. Shaffer, Y. An, Q. Liu, B. Wei, and H. Jiang, *Silicon Thin Films as Anodes for High-Performance Lithium-Ion Batteries with Effective Stress Relaxation.* Advanced Energy Materials, 2012. **2**(1): p. 68-73.

23. Chen, L.B., J.Y. Xie, H.C. Yu, and T.H. Wang, *An amorphous Si thin film anode with high capacity and long cycling life for lithium ion batteries.* Journal of Applied Electrochemistry, 2009. **39**(8): p. 1157-1162.

24. Nguyen, C.C. and S.-W. Song, *Interfacial structural stabilization on amorphous silicon anode for improved cycling performance in lithium-ion batteries.* Electrochimica Acta, 2010. **55**(8): p. 3026-3033.

25. Min-Feng, Y., O. Lourie, M.J. Dyer, K. Moloni, T.F. Kelly, and R.S. Ruoff, *Strength and Breaking Mechanism of Multiwalled Carbon Nanotubes Under Tensile Load.* Science, 2000. **287**(5453): p. 637-640.

26. Berber, S., Y.K. Kwon, and D. Tomanek, *Unusually high thermal conductivity of carbon nanotubes.* Physical Review Letters, 2000. **84**(20): p. 4613-4616.

27. Ebbesen, T.W., H.J. Lezec, H. Hiura, J.W. Bennett, H.F. Ghaemi, and T. Thio, *Electrical conductivity of individual carbon nanotubes.* Nature, 1996. **382**(6586): p. 54-56.

28. Gohier, A., B. Laik, K.H. Kim, J.L. Maurice, J.P. Pereira-Ramos, C.S. Cojocaru, and P. Van Tran, *High-rate capability silicon decorated vertically aligned carbon nanotubes for Li-ion batteries.* Adv Matererials, 2012. **24**(19): p. 2592-7.

29. Epur, R., M.K. Datta, and P.N. Kumta, *Nanoscale engineered electrochemically active silicon–CNT heterostructures-novel anodes for Li-ion application.* Electrochimica Acta, 2012. **85**: p. 680-684.

30. Dees, D., E. Gunen, D. Abraham, A. Jansen, and J. Prakash, *Electrochemical Modeling of Lithium-Ion Positive Electrodes during Hybrid Pulse Power Characterization Tests.* Journal of The Electrochemical Society, 2008. **155**(8): p. A603.

31. Doyle, M., *Modeling of Galvanostatic Charge and Discharge of the Lithium/Polymer/Insertion Cell.* Journal of The Electrochemical Society, 1993. **140**(6): p. 1526.

32. Doyle, M., *Comparison of Modeling Predictions with Experimental Data from Plastic Lithium Ion Cells.* Journal of The Electrochemical Society, 1996. **143**(6): p. 1890.

33. Doyle, M., T.F. Fuller, and J. Newman, *The importance of the lithium ion transference number in lithium/polymer cells.* Electrochimica Acta, 1994. **39**(13): p. 2073-2081.

34. Fuller, T.F., *Simulation and Optimization of the Dual Lithium Ion Insertion Cell.* Journal of The Electrochemical Society, 1994. **141**(1): p. 1.

35. Gomadam, P.M., J.W. Weidner, R.A. Dougal, and R.E. White, *Mathematical modeling of lithium-ion and nickel battery systems.* Journal of Power Sources, 2002. **110**(2): p. 267-284.

36. Ning, G., R.E. White, and B.N. Popov, *A generalized cycle life model of rechargeable Li-ion batteries.* Electrochimica Acta, 2006. **51**(10): p. 2012-2022.

37. Santhanagopalan, S., Q. Guo, P. Ramadass, and R.E. White, *Review of models for predicting the cycling performance of lithium ion batteries.* Journal of Power Sources, 2006. **156**(2): p. 620-628.

38. Ramadesigan, V., P.W.C. Northrop, S. De, S. Santhanagopalan, R.D. Braatz, and V.R. Subramanian, *Modeling and Simulation of Lithium-Ion Batteries from a Systems Engineering Perspective.* Journal of the Electrochemical Society, 2012. **159**(3): p. R31-R45.

39. Ramadesigan, V., K. Chen, N.A. Burns, V. Boovaragavan, R.D. Braatz, and V.R. Subramanian, *Parameter Estimation and Capacity Fade Analysis of Lithium-Ion Batteries Using Reformulated Models.* Journal of The Electrochemical Society, 2011. **158**(9): p. A1048.

40. McDowell, M.T., S.W. Lee, W.D. Nix, and Y. Cui, *25th anniversary article: Understanding the lithiation of silicon and other alloying anodes for lithium-ion batteries.* Adv Mater, 2013. **25**(36): p. 4966-85.

41. Chen-Min Li, J., *Physical chemistry of some microstructural phenomena.* Metallurgical Transactions A, 1978. **9**(10): p. 1353-1380.

42. Lee, S. and H. Ouyang, *General Solution of Diffusion-Induced Stresses.* Journal of Thermal Stresses, 1987. **10**(4): p. 269-282.

43. Cheng, Y.-T. and M.W. Verbrugge, *Evolution of stress within a spherical insertion electrode particle under potentiostatic and galvanostatic operation.* Journal of Power Sources, 2009. **190**(2): p. 453-460.

44. Cheng, Y.-T. and M.W. Verbrugge, *Diffusion-Induced Stress, Interfacial Charge Transfer, and Criteria for Avoiding Crack Initiation of Electrode Particles.* Journal of The Electrochemical Society, 2010. **157**(4): p. A508.

45. Deshpande, R., Y.-T. Cheng, M.W. Verbrugge, and A. Timmons, *Diffusion Induced Stresses and Strain Energy in a Phase-Transforming Spherical Electrode Particle.* Journal of The Electrochemical Society, 2011. **158**(6): p. A718.

46. Park, J., W. Lu, and A.M. Sastry, *Numerical Simulation of Stress Evolution in Lithium Manganese Dioxide Particles due to Coupled Phase Transition and Intercalation.* Journal of The Electrochemical Society, 2011. **158**(2): p. A201.

47. Verbrugge, M.W. and Y.-T. Cheng, *Stress and Strain-Energy Distributions within Diffusion-Controlled Insertion-Electrode Particles Subjected to Periodic Potential Excitations.* Journal of The Electrochemical Society, 2009. **156**(11): p. A927.

48. Zhang, X., A.M. Sastry, and W. Shyy, *Intercalation-Induced Stress and Heat Generation within Single Lithium-Ion Battery Cathode Particles.* Journal of The Electrochemical Society, 2008. **155**(7): p. A542.

49. Zhang, X., W. Shyy, and A. Marie Sastry, *Numerical Simulation of Intercalation-Induced Stress in Li-Ion Battery Electrode Particles.* Journal of The Electrochemical Society, 2007. **154**(10): p. A910.

50. Jagannathan, K. and K. Raghunathan, *Charge-Discharge Asymmetry of Phase Change Electrodes from Isotropic Solid State Diffusion Models.* Journal of the Electrochemical Society, 2013. **159**(1): p. A26-A37.

51. Bhandakkar, T.K. and H. Gao, *Cohesive modeling of crack nucleation in a cylindrical electrode under axisymmetric diffusion induced stresses.* International Journal of Solids and Structures, 2011. **48**(16-17): p. 2304-2309.

52. Deshpande, R., Y.-T. Cheng, and M.W. Verbrugge, *Modeling diffusion-induced stress in nanowire electrode structures.* Journal of Power Sources, 2010. **195**(15): p. 5081-5088.

53. Deshpande, R., Y. Qi, and Y.-T. Cheng, *Effects of Concentration-Dependent Elastic Modulus on Diffusion-Induced Stresses for Battery Applications.* Journal of The Electrochemical Society, 2010. **157**(8): p. A967.

54. Harris, S.J., R.D. Deshpande, Y. Qi, I. Dutta, and Y.-T. Cheng, *Mesopores inside electrode particles can change the Li-ion transport mechanism and diffusion-induced stress.* Journal of Materials Research, 2011. **25**(08): p. 1433-1440.

55. Sethuraman, V.A., M.J. Chon, M. Shimshak, V. Srinivasan, and P.R. Guduru, *In Situ Measurements of Stress Evolution in Silicon Thin Films During Electrochemical Lithiation and Delithiation* Journal of Power Sources, 2010. **195**(15): p. 5062-5066.

56. Sethuraman, V.A., V. Srinivasan, A.F. Bower, and P.R. Guduru, *In Situ Measurements of Stress-Potential Coupling in Lithiated Silicon.* Journal of The Electrochemical Society, 2010. **157**(11): p. A1253.

57. Shenoy, V.B., P. Johari, and Y. Qi, *Elastic softening of amorphous and crystalline Li–Si Phases with increasing Li concentration: A first-principles study.* Journal of Power Sources, 2010. **195**(19): p. 6825-6830.

58. Chen, B., J. Zhou, X. Pang, P. Wei, Y. Wu, and K. Deng, *Fracture damage of nanowire lithium-ion battery electrode affected by diffusion-induced stress and bending during lithiation.* RSC Advances, 2014. **4**(40): p. 21072.

59. Grantab, R. and V.B. Shenoy, *Pressure-Gradient Dependent Diffusion and Crack Propagation in Lithiated Silicon Nanowires.* Journal of The Electrochemical Society, 2012. **159**(5): p. A584.

60. Kalnaus, S., K. Rhodes, and C. Daniel, *A study of lithium ion intercalation induced fracture of silicon particles used as anode material in Li-ion battery.* Journal of Power Sources, 2011. **196**(19): p. 8116-8124.

61. Grantab, R. and V.B. Shenoy, *Location- and Orientation-Dependent Progressive Crack Propagation in Cylindrical Graphite Electrode Particles.* Journal of The Electrochemical Society, 2011. **158**(8): p. A948.

62. Zhao, K., M. Pharr, L. Hartle, J.J. Vlassak, and Z. Suo, *Fracture and debonding in lithium-ion batteries with electrodes of hollow core–shell nanostructures.* Journal of Power Sources, 2012. **218**: p. 6-14.

63. Zhao, K., W.L. Wang, J. Gregoire, M. Pharr, Z. Suo, J.J. Vlassak, and E. Kaxiras, *Lithium-assisted plastic deformation of silicon electrodes in lithium-ion batteries: a first-principles theoretical study.* Nano Lett, 2011. **11**(7): p. 2962-7.

64. Zhao, K., M. Pharr, Q. Wan, W.L. Wang, E. Kaxiras, J.J. Vlassak, and Z. Suo, *Concurrent Reaction and Plasticity during Initial Lithiation of Crystalline Silicon in Lithium-Ion Batteries.* Journal of the Electrochemical Society, 2012. **159**(3): p. A238-A243.

65. Zhao, K., W.L. Wang, J. Gregoire, M. Pharr, Z. Suo, J.J. Vlassak, and E. Kaxiras, *Lithium-Assisted Plastic Deformation of Silicon Electrodes in Lithium-Ion Batteries: A First-Principles Theoretical Study.* Nano Letters, 2011. **11**: p. 2962-2967.

66. Zhao, K., M. Pharr, J.J. Vlassak, and Z. Suo, *Inelastic hosts as electrodes for high-capacity lithium-ion batteries.* Journal of Applied Physics, 2011. **109**(1): p. 016110.

67. Brassart, L., K. Zhao, and Z. Suo, *Cyclic plasticity and shakedown in high-capacity electrodes of lithium-ion batteries.* International Journal of Solids and Structures, 2013. **50**(7-8): p. 1120-1129.

68. Deshpande, V.S., A. Needlemana, and E. Van der Giessen, *Discrete dislocation modeling of fatigue crack propagation.* Acta Materialia, 2002. **50**(4): p. 831-846.

69. Maiti, S. and P. Geubelle, *Cohesive modeling of fatigue crack retardation in polymers: Crack closure effect.* Engineering Fracture Mechanics, 2006. **73**(1): p. 22-41.

70. Ortiz, M. and A. Pandolfi, *Finite deformation irreversible cohesive elements for three-dimensional crack-propagation analysis.* International Journal for Numerical Methods in Engineering, 1999. **44**: p. 1267-1282.

71. Bockris, J.O., A.K.N. Reddy, and M. Gamboa-Aldeco, *Modern Electrochemistry 2A: Fundamentals of Electrodics*. Vol. 2. 2001: Springer.

72. Huggins, R.A., *Lithium Alloy Anodes.* 2011: p. 405-431.

73. Deshpande, V.S., A. Needleman, and E. Van der Giessen, *A discrete dislocation analysis of near-threshold fatigue crack growth.* Acta Materialia, 2001. **49**(16): p. 3189-3203.

74. Maiti, S. and P. Geubelle, *A cohesive model for fatigue failure of polymers.* Engineering Fracture Mechanics, 2005. **72**(5): p. 691-708.

75. Maiti, S., C. Shankar, P.H. Geubelle, and J. Kieffer, *Continuum and Molecular-Level Modeling of Fatigue Crack Retardation in Self-Healing Polymers.* Journal of Engineering Materials and Technology, 2006. **128**(4): p. 595-602.

76. Pal, S., S.S. Damle, S.H. Patel, M.K. Datta, P.N. Kumta, and S. Maiti, *Modeling the delamination of amorphous-silicon thin film anode for lithium-ion battery.* Journal of Power Sources, 2014. **246**: p. 149-159.

77. Park, K., G.H. Paulino, and J.R. Roesler, *A unified potential-based cohesive model of mixed-mode fracture.* Journal of the Mechanics and Physics of Solids, 2009. **57**: p. 891-908.

78. Mishin, Y., P. Sofronis, and J.L. Bassani, *Thermodynamic and kinetic aspects of interfacial decohesion.* Acta materialia, 2002. **50**: p. 3609-3622.

79. Wang, J.S., *The thermodynamics aspects of hydrogen induced embrittlement.* Engineering Fracture Mechanics, 2001. **68**(6): p. 647-669.

80. Rice, J.R. and J.-S. Wang, *Embrittlement of interfaces by solute segregation.* Materials Science and Engineering: A, 1989. **107**: p. 23-40.

81. Evans, A.G., J.W. Hutchinson, and Y. Wei, *Interface adhesion: Effect of plasticity and segregation.* Acta materialia, 1999. **47**(15): p. 4093-4113.

82. Dowben, P.A. and A. Miller, *Surface segregation phenomena*. 1990, Boca Raton, Florida: CRC Press, Inc.

83. McLean, D., *Grain boundaries in metals*. 1957, Oxford: Oxford University Press.

84. Shaw, D., *Atomic Diffusion in Semiconductors*. 1973: Springer.

85. Cho, G.-b., J.-p. Noh, H.-j. Sung, S.-y. Choi, S.-h. Lee, H.-j. Ahn, T.-h. Nam, and K.-w. Kim, *Improved electrochemical properties of patterned Si film electrodes.* Microelectronic Engineering, 2012. **89**: p. 104-108.

86. Soni, S., B.W. Sheldon, X. Xiao, M.W. Verbrugge, A. Dongjoon, H. Haftbaradaran, and H. Gao, *Stress Mitigation during the Lithiation of Patterned Amorphous Si Islands.* Journal of The Electrochemical Society, 2011. **159**(1): p. A38-A43.

87. Haftbaradaran, H., X. Xio, M.W. Verbrugge, and H. Gao, *Method to deduce the critical size for interfacial delamination of patterned electrode structures and application to lithiation of thin-film silicon islands.* Journal of Power Sources, 2012. **206**: p. 357-366.

88. Haftbaradaran, H., S.K. Soni, B.W. Sheldon, X. Xiao, and H. Gao, *Modified Stoney Equation for Patterned Thin Film Electrodes on Substrates in the Presence of Interfacial Sliding.* Journal of Applied Mechanics, 2012. **79**: p. 031018-1 031018-6.

89. Chandrasekaran, R. and T.F. Fuller, *Analysis of the Lithium-Ion Insertion Silicon Composite Electrode/Separator/Lithium Foil Cell.* Journal of The Electrochemical Society, 2011. **158**(8): p. A859.

90. Stournara, M.E., X. Xiao, Y. Qi, P. Johari, P. Lu, B.W. Sheldon, H. Gao, and V.B. Shenoy, *Li segregation induces structure and strength changes at the amorphous Si/Cu interface.* Nano Lett, 2013. **13**(10): p. 4759-68.

91. Haftbaradaran, H., S.K. Soni, B.W. Sheldon, X. Xiao, and H. Gao, *Modified Stoney Equation for Patterned Thin Film Electrodes on Substrates in the Presence of Interfacial Sliding.* Journal of Applied Mechanics, 2012. **79**(3): p. 031018.

92. Soni, S.K., B.W. Sheldon, X. Xiao, M.W. Verbrugge, D. Ahn, H. Haftbaradaran, and H. Gao, *Stress Mitigation during the Lithiation of Patterned Amorphous Si Islands.* Journal of The Electrochemical Society, 2012. **159**(1): p. A38.

93. Cho, G., J. Noh, H. Sung, S. Choi, S. Lee, H. Ahn, T. Nam, and K. Kim, *Improved electrochemical properties of patterned Si film electrodes.* Microelectronic Engineering, 2012. **89**: p. 104-108.

94. Song, Y., B. Lu, X. Ji, and J. Zhang, *Diffusion Induced Stresses in Cylindrical Lithium-Ion Batteries: Analytical Solutions and Design Insights.* Journal of The Electrochemical Society, 2012. **159**(12): p. A2060-A2068.

95. Zhang, J., B. Lu, Y. Song, and X. Ji, *Diffusion induced stress in layered Li-ion battery electrode plates.* Journal of Power Sources, 2012. **209**: p. 220-227.

96. Y.Q. Zhang, X.H.X., X.L. Wang, Y.J. Mai, S.J. Shi, Y.Y. Tang, L. Li, J.P. Tu, *Silicon/graphene-sheet hybrid film as anode for lithium ion batteries.* Electrochemistry Communications, 2012. **23**: p. 17-20.

97. Yongfeng Tong, Z.X., Chang Liu, Guang'an Zhang, Jun Wang, Z.G. Wu, *Magnetic sputtered amorphous Si/C multilayer thin films as anode materials for lithium ion batteries.* Journal of Power Sources, 2013. **247**: p. 78-83.

98. Choi, J.-Y., D.J. Lee, Y.M. Lee, Y.-G. Lee, K.M. Kim, J.-K. Park, and K.Y. Cho, *Silicon Nanofibrils on a Flexible Current Collector for Bendable Lithium-Ion Battery Anodes.* Advanced Functional Materials, 2013. **23**(17): p. 2108-2114.

99. Siladitya Pal, S.S.D., Siddharth H. Patel, Moni K. Datta, Prashant N. Kumta, Spandan Maiti, *Modeling the delamination of amorphous-silicon thin film anode for lithium-ion battery.* Journal of Power Sources, 2014: p. 149-159.

100. Pal, S., S. Damle, S. Patel, M.K. Dutta, P.N. Kumta, and S. Maiti, *Micromechanisms of capacity fade in silicon anode for lithium-Ion batteries.* ECS Transactions, 2012. **41**(11): p. 87-89.

101. Pal, S., S.S. Damle, P.N. Kumta, and S. Maiti, *Modeling of Lithium segregation induced delamination of a-Si thin film anode in Li-ion batteries* Computational Material Science, 2013. **79**: p. 877–887.

102. Sethuraman, V.A., M.J. Chon, M. Shimshak, V. Srinivasan, and P.R. Guduru, *In situ measurements of stress evolution in silicon thin films during electrochemical lithiation and delithiation.* Journal of Power Sources, 2010. **195**(15): p. 5062-5066.

103. Zhao, K.J., M. Pharr, J.J. Vlassak, and Z.G. Suo, *Inelastic hosts as electrodes for high-capacity lithium-ion batteries.* Journal of Applied Physics, 2011. **109**(1).

104. Mukhopadhyay, A. and B.W. Sheldon, *Deformation and stress in electrode materials for Li-ion batteries.* Progress in Materials Science, 2014. **63**: p. 58-116.

105. Zhu, H., Z. Jia, Y. Chen, N. Weadock, J. Wan, O. Vaaland, X. Han, T. Li, and L. Hu, *Tin anode for sodium-ion batteries using natural wood fiber as a mechanical buffer and electrolyte reservoir.* Nano Lett, 2013. **13**(7): p. 3093-100.

106. Yao, Y., M.T. McDowell, I. Ryu, H. Wu, N. Liu, L. Hu, W.D. Nix, and Y. Cui, *Interconnected silicon hollow nanospheres for lithium-ion battery anodes with long cycle life.* Nano Lett, 2011. **11**(7): p. 2949-54.

107. Liu, X.H., L. Zhong, S. Huang, S.X. Mao, T. Zhu, and J.Y. Huang, *Size-dependent fracture of silicon nanoparticles during lithiation.* ACS Nano, 2012. **6**(2): p. 1522-31.

108. Ma, Z.S., T.T. Li, Y.L. Huang, J. Liu, Y.C. Zhou, and D.F. Xue, *Critical silicon-anode size for averting lithiation-induced mechanical failure of lithium-ion batteries.* Rsc Advances, 2013. **3**(20): p. 7398-7402.

109. Chen, J., Y. Liu, A.I. Minett, C. Lynam, J. Wang, and G.G. Wallace, *Flexible, Aligned Carbon Nanotube/Conducting Polymer Electrodes for a Lithium-Ion Battery.* Chemistry of Materials, 2007. **19**(15): p. 3595-3597.

110. Fan, Y., Q. Zhang, C. Lu, Q. Xiao, X. Wang, and B.K. Tay, *High performance carbon nanotube-Si core-shell wires with a rationally structured core for lithium ion battery anodes.* Nanoscale, 2013. **5**(4): p. 1503-6.

111. Fan, Y., Q. Zhang, Q. Xiao, X. Wang, and K. Huang, *High performance lithium ion battery anodes based on carbon nanotube–silicon core–shell nanowires with controlled morphology.* Carbon, 2013. **59**: p. 264-269.

112. Evanoff, K., J. Khan, A.A. Balandin, A. Magasinski, W.J. Ready, T.F. Fuller, and G. Yushin, *Towards ultrathick battery electrodes: aligned carbon nanotube-enabled architecture.* Adv Matererials, 2012. **24**(4): p. 533-7.

113. Epur, R., M. Ramanathan, M.K. Datta, D.H. Hong, P.H. Jampani, B. Gattu, and P.N. Kumta, *Scribable multi-walled carbon nanotube-silicon nanocomposites: a viable lithium-ion battery system.* Nanoscale, 2015. **7**(8): p. 3504-10.

114. Wang, W., R. Epur, and P.N. Kumta, *Vertically aligned silicon/carbon nanotube (VASCNT) arrays: Hierarchical anodes for lithium-ion battery.* Electrochemistry Communications, 2011. **13**(5): p. 429-432.

115. Wang, W. and P.N. Kumta, *Nanostructured hybrid silicon/carbon nanotube heterostructures: reversible high-capacity lithium-ion anodes.* ACS Nano, 2010. **4**(4): p. 2233-41.

116. CUBIT Geometry and Meshing Toolkit Version 14.1 (https://cubit.sandia.gov/public/14.1/Cubit-14.1-announcement.html), 2014.

117. Pal, S., S.S. Damle, P.N. Kumta, and S. Maiti, *Modeling of lithium segregation induced delamination of a-Si thin film anode in Li-ion batteries.* Computational Materials Science, 2013. **79**: p. 877-887.

118. Pal, S., S. Damle, S. Patel, M.K. Dutta, P.N. Kumta, and S. Maiti, *Micromechanisms of Capacity Fade in Silicon Anode for Lithium-Ion Batteries.* 2012: p. 87-99.

119. McDowell, M.T., S.W. Lee, J.T. Harris, B.A. Korgel, C. Wang, W.D. Nix, and Y. Cui, *In situ TEM of two-phase lithiation of amorphous silicon nanospheres.* Nano Lett, 2013. **13**(2): p. 758-64.

120. Wang, J.W., X.H. Liu, K. Zhao, A. Palmer, E. Patten, D. Burton, S.X. Mao, Z. Suo, and J.Y. Huang, *Sandwich-Lithiation and Longitudinal Crack in Amorphous Silicon Coated on Carbon Nanofibers.* ACS Nano, 2012. **6**(10): p. 9158-9167.

121. Wang, J.W., Y. He, F. Fan, X.H. Liu, S. Xia, Y. Liu, C.T. Harris, H. Li, J.Y. Huang, S.X. Mao, and T. Zhu, *Two-phase electrochemical lithiation in amorphous silicon.* Nano Lett, 2013. **13**(2): p. 709-15.

122. Ding, N., J. Xu, Y.X. Yao, G. Wegner, X. Fang, C.H. Chen, and I. Lieberwirth, *Determination of the diffusion coefficient of lithium ions in nano-Si.* Solid State Ionics, 2009. **180**(2-3): p. 222-225.

123. Boles, S.T., A. Sedlmayr, O. Kraft, and R. Mönig, *In situ cycling and mechanical testing of silicon nanowire anodes for lithium-ion battery applications.* Applied Physics Letters, 2012. **100**(24): p. 243901.

124. Kushima, A., J.Y. Huang, and J. Li, *Quantitative Fracture Strength and Plasticity Measurements of Lithiated Silicon Nanowires by In Situ TEM Tensile Experiments.* ACS Nano, 2012. **6**(11): p. 9425-9432.

125. Qian, D., G.J. Wagner, W.K. Liu, M.-F. Yu, and R.S. Ruoff, *Mechanics of carbon nanotubes.* Applied Mechanics Reviews, 2002. **55**(6): p. 495.

126. Ayachit, U., The ParaView Guide: A Parallel Visualization Application (Kitware), 2015.

127. Argon, A.S. and J. Im, *Separation of Second-Phase Particles in Spheroidized 1045 Steel, Cu-0.6pct Cr Alloy, and Maraging-Steel in Plastic Straining.* Metallurgical Transactions, 1975. **A 6**(4): p. 839-851.

128. Shabrov, M.N., E. Sylven, S. Kim, D.H. Sherman, L. Chuzhoy, C.L. Briant, and A. Needleman, *Void nucleation by inclusion cracking.* Metallurgical and Materials Transactions a-Physical Metallurgy and Materials Science, 2004. **35A**(6): p. 1745-1755.

129. Rice, J.R. and D.M. Tracey, *On the ductile enlargement of voids in triaxial stress fields*. Journal of the Mechanics and Physics of Solids, 1969. **17**(3): p. 201-217.

130. Horstemeyer, M.F. and A.M. Gokhale, *A void–crack nucleation model for ductile metals.* International Journal of Solids and Structures, 1999. **36**(33): p. 5029-5055.

131. Choi, J.W., J. McDonough, S. Jeong, J.S. Yoo, C.K. Chan, and Y. Cui, *Stepwise nanopore evolution in one-dimensional nanostructures.* Nano Lett, 2010. **10**(4): p. 1409-13.

132. Wan, J., A.F. Kaplan, J. Zheng, X. Han, Y. Chen, N.J. Weadock, N. Faenza, S. Lacey, T. Li, J. Guo, and L. Hu, *Two dimensional silicon nanowalls for lithium ion batteries.* J. Mater. Chem. A, 2014. **2**(17): p. 6051-6057.

133. Datta, M.K., R. Epur, P. Saha, K. Kadakia, S.K. Park, and P.N. Kumta, *Tin and graphite based nanocomposites: Potential anode for sodium ion batteries.* Journal of Power Sources, 2013. **225**: p. 316-322.

134. Yabuuchi, N., Y. Matsuura, T. Ishikawa, S. Kuze, J.-Y. Son, Y.-T. Cui, H. Oji, and S. Komaba, *Phosphorus Electrodes in Sodium Cells: Small Volume Expansion by Sodiation and the Surface-Stabilization Mechanism in Aprotic Solvent.* ChemElectroChem, 2014. **1**(3): p. 580-589.

135. Baggetto, L., J.F.M. Oudenhoven, T. van Dongen, J.H. Klootwijk, M. Mulder, R.A.H. Niessen, M.H.J.M. de Croon, and P.H.L. Notten, *On the electrochemistry of an anode stack for all-solid-state 3D-integrated batteries.* Journal of Power Sources, 2009. **189**(1): p. 402-410.